Exploiting Spin Manipulation and Stereo-Isomerization in Molecular Switches
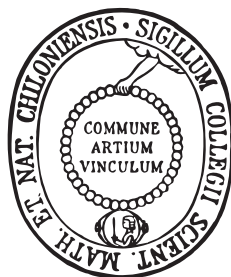
A thesis presented for the degree of

Doctor of Natural Sciences

to

the Faculty of Mathematics and Natural Sciences
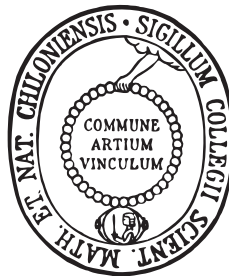of Christian-Albrechts-University of Kiel

by

Sujoy Karan

Kiel, 2015

Exploiting Spin Manipulation and Stereo-Isomerization in Molecular Switches

Dissertation
zur Erlangung des Doktorgrades
der Mathematisch-Naturwissenschaftliche Fakultät
der Christian-Albrechts-Universität zu Kiel

vorgelegt von

Sujoy Karan

Kiel, 2015

to my parents

This work has been carried out under the
supervision of Prof. Dr. Richard Berndt
at
the Institute of Experimental and Applied
Physics,
Christian-Albrechts-University of Kiel,
Germany

Typeset in LaTeX

First Examiner: Prof. Dr. Richard Berndt

Second Examiner: Prof. Dr. Olaf Magnussen

Date of Examination: 04.06.2015

Approved for Printing: 04.06.2015

<div style="text-align:center">

_____

Prof. Dr. Wolfgang J. Duschl

Dean, Faculty of Mathematics and Natural Sciences

</div>

Contents

Abstract

Using molecules for electronics is a novel endeavor, and the subject of compelling research focusing mainly on the characterization of single molecules.

This thesis presents different aspects of molecular functionalities at surfaces, investigated using a low-temperature Scanning Tunneling Microscope (STM). A variety of substances, from organometallic complexes to organic biomolecules, are addressed, which demonstrate several issues relating to the response of individual molecules (or parts of them) to external stimuli.

The focus of this thesis is threefold.

First, it involves the characterization of surface-induced molecular configurations and their agglomeration into supramolecular structures. For example, bis-terpyridine ligands, dissociated from metallosupramolecular grids, are trapped in their out-of-equilibrium high-energy conformations on a Au(111) substrate. The most abundant conformer is found to be an asymmetric form of the ligand, which has not been observed before.

The fabrication of supramolecules with C_5 symmetry, which are mainly found in living organisms, is presented from *all-trans*-retinoic acid. These pentamers are found to agglomerate in large arrays with patterns resembling a so called pentagonal *Cairo* tiling, although a planar surface can not be filled completely with regular pentagons.

Second, switching of individual molecules and concomitant changes in their electronic structures are presented along with the underlying switching mechanisms. For instance, controlled and reversible remote switching within a single binuclear organometallic complex is demonstrated (the first of its kind). By injecting current to one subunit, a geometrical isomerization of the other has been achieved via a so called *Bailar* twist. The process is attributed to the intramolecular electron transfer.

Manipulation of molecular spin states is presented from two different organic bio-molecules on a Au(111) substrate. In both cases, the molecules can be switched to a number of states, few of which carry localized spin as revealed from the Kondo fingerprints in conductance spectra. The creation and annihilation of single-molecule radical cations are proposed to be the cause of the reversible spin-state switching.

Third, the thesis addresses electron transport through junctions comprising

single molecules. Mn-porphyrin, a planar molecule, was studied on Au(111). Using a sharp feature at the Fermi energy, which results from a Kondo effect, it is shown that a significant amount of voltage ($\geq 80\%$) applied to the junction drops at the molecule-substrate spacing, when the central Mn atom is contacted with the STM tip. This result implies that the simple assumption made about a symmetrically coupled molecular junction—that the applied voltage drops equally on both molecule-electrode interfaces—may be invalid in many cases.

On the whole, the results of this thesis add to the understanding of the response of individual molecules to charge injection, highlighting several important details of single-molecule junctions.

Zusammenfassung

Um Moleküle für elektronische Anwendungen nutzbar zu machen, ist eine gezielte Erforschung der Eigenschaften einzelner Moleküle notwendig. In dieser Arbeit werden Moleküle auf Oberflächen mit Hilfe der Tieftemperatur-Rastertunnel-mikroskopie unter verschiedenen Gesichtspunkten untersucht. An mehreren Substanzen, von organometallischen Verbindungen bis zu organischen Biomole-külen, wird deren Reaktion auf externe Stimuli gezeigt. Diese Arbeit beleuchtet dabei drei Gesichtspunkte:

Zum einen werden oberflächeninduzierte Molekülkonfigurationen und die Anordnung in supramolekularen Strukturen charakterisiert. So wird zum Bei-spiel gezeigt, dass Bis-Terpyridin-Liganden, welche durch Dissoziation metall-supramolekularer Verbindungen entstehen, durch Adsorption auf der Au(111)-Oberfläche in eine hochenergetische Nichtgleichgewichtskonformation gezwun-gen werden. Das am häufigsten beobachtete Konformer liegt dabei in einer asymmetrischen Form vor, die bisher noch nicht beobachtet wurde.

Die Herstellung von Supramolekülen mit C_5-Symmetrie, welche auch in lebenden Organismen vorkommt, wird an *all-trans*-Retinsäure demonstriert. Es wird gezeigt, dass diese Pentamere sich in großen regelmäßigen Strukturen – ähnlich der sogenannten Kairo-Parkettierung – anordnen, die für regelmäßige Fünfecke nicht möglich wären.

Als zweites werden Schaltprozesse einzelner Moleküle und die damit ein-hergehenden Änderungen der elektronischer Struktur und der zugrunde liegende Schaltmechanismus untersucht. So wird z. B. zum ersten Mal ein kontrol-liertes, nicht-lokales und reversibles Schalten einer dinuklearen organometal-lischen Verbindung gezeigt. Die Ladungsinjektion in eine Untereinheit erzeugt dabei eine geometrische Isomerisierung der anderen Untereinheit durch einen so-genannten *Bailar twist*, welcher auf intramolekularen Elektronentransfer zurück-zuführen ist. Die Manipulation molekularer Spinzustände wird an zwei ver-schiedenen organischen Biomolekülen auf Au(111) gezeigt. In beiden Fällen können die Moleküle in verschiedene Zustände geschaltet werden, von denen einige einen lokalisierten Spin besitzen. Dieser kann durch eine Kondosignatur in Leitwertspektren nachgewiesen werden. Als Ursache dieser reversiblen Schalt-prozesse des Molekülspins wird die Erzeugung und Vernichtung von Radikal-

kationen vorgeschlagen.

Als dritter Aspekt wird der Elektronentransport durch Einzelmolekülkontakte untersucht. Dies geschieht an dem planaren Molekül Mn-Porphyrin auf Au(111). Mit Hilfe einer durch den Kondoeffekt hervorgerufenen scharfen Signatur an der Fermienergie wird gezeigt, dass ein signifikanter Teil ($\geq 80\%$) der angelegten Spannung zwischen Molekül und Substrat abfällt, wenn das zentrale Mn-Atom mit der Spitze eines Rastertunnelmikroskops kontaktiert wird. Die vereinfachende Annahme eines symmetrisch gekoppelten Molekülkontakts, bei dem die angelegte Spannung an den Übergangen zu beiden Elektroden symmetrisch abfällt, ist in vielen Fällen somit nicht gerechtfertigt.

Insgesamt zeigt diese Arbeit, wie sich durch Ladungsinjektion die strukturellen und elektronischen Eigenschaften einzelner Moleküle verändern lassen.

Thesis Outline

The outline of the thesis is as follows:

Chapter 1 starts with the foundations of molecular electronics and subsequently develops into a brief survey including the latest advances and the prospects for this field.

Chapter 2 briefly describes the experimental techniques together with significant details of the topics that are pertinent to the subject matter.

Chapter 3 provides a brief overview of the experimental setup with relevant details.

Chapter 4 presents results from a Mn-porphyrin that was contacted in a scanning tunneling microscope. Using the Kondo resonance in the differential conductance spectra, it is shown that the electrostatic potential of a molecule can be very relevant for interpreting electron transport through molecules.

Chapter 5 demonstrates controlled and reversible remote switching within a single binuclear organometallic molecule. By injecting current to one subunit, a reversible isomerization of the other has been achieved. The process is attributed to intramolecular electron transfer.

Chapter 6 reports the formation of surface-trapped conformations of a bis(terpyridine) ligand on Au(111). The most abundant conformer is found to be an asymmetric form of the ligand, which has not been observed before.

Chapter 7 presents the preparation of supramolecular pentamers from *all-trans*-retinoic acid molecules on Au(111) surfaces as well as on a molecular monolayer. The stability of pentamers is analyzed from experiments using an isomer of retinoic acid and density functional theory calculations.

Chapter 8 and 9 presents the generation and annihilation of spin in single organic bio-molecules on Au(111). Two different molecules were investigated. In both the cases, the molecules are switched to a number of states, few of which carry localized spin as evidenced from the Kondo fingerprints in conductance spectra. A thorough analysis is done performing experiments on different substrates and comparing results from a different isomer. The experimental results are supported by the density functional theory calculations.

Editorial changes have been made in adapting the published manuscripts into the format of this thesis without changing their scientific contents.

1   Introduction

The concept of using molecules as active electronic components has attracted huge research efforts in recent years for the development of *nano-molecular* devices. However, integrating molecules into electrical circuits will require fabrication strategies, that are still long-sought goals. A rather pragmatic approach was thus taken in initiating this thesis which aimed at understanding *molecular functionalities* in tunneling as well as transport junctions.

Background

The field of *"molecular electronics"*,[1] as we understand it today [1], was commenced with the studies conducted by *Mann* and *Kuhn* in 1971, reporting conductivity measurements through monolayers of cadmium salts of fatty acids [2]. Their measurements showed that the conductivity decreased exponentially with layer thickness, therefore revealing electron tunneling through the organic layer [1, 2]. Later in 1974, *Aviram* and *Ratner* came with the seminal idea of unimolecular *quantum transport* and its application as a rectifier in an electrical circuit [3]. It did not have much impact at that time due to limitations on the experimental front to deal with single molecules. But it was in 1981, that the field of *nanoscience* leapt forward with the advent of scanning tunneling microscope (STM) [4–6]. Within few years, molecules were successfully introduced—the molecule that has been introduced first was copper phthalocyanine imaged by *Gimzewski et al.* [7]—onto the surfaces with the opening of a realistic way to characterize single molecules.

Prospects

An important challenge lies in interpreting electron transport through junctions comprising individual molecules or an array of molecules that are coupled to macroscopic electrodes [8, 9]. The transport properties of these junctions involve numerous microscopic details, sensitive to both physical and chemical parameters. For example, the influence of the contact geometry on the conductance of a single C_{60} molecule has recently been studied in detail by *Schull et al.*

---

[1]The term *"molecular engineering"* was coined in the 1950s by *Hippel* suggesting the feasibility of molecular *nano*-devices [10].

[11]. Not many experiments have gained such a control at the level of atomic length-scale in a molecular transport junction. Examining charge-transport in reduced dimensions may, thus, lead us exploring many unexpected physical phenomena.

Manipulating charge-transport by spin–and vice versa–is a central paradigm in spintronics applications [12–14]. Materials studied for spintronics have so far been exclusively dominated by conventional metallic compounds and semiconductors [15, 16]. However, little is known about the spintronic properties of molecular structures. Spin-induced effects in molecules or within molecular bridges may have potential application in data storage and sensing.

Understanding charge-transfer to and through a molecule is one of the important issues, that involves transfer of energy within the molecules. This process needs to be interpreted at a single molecule level, *e.g.*, to implement molecule-based logic functions where a lateral energy transfer is necessary. An experimental realization of intramolecular electron transfer has recently been shown by me and co-workers [17], where individual binuclear organometallic complexes were addressed. The chemical nature of the transfer-pathway has been found to be crucial. Inquisitive approach towards this hardly explored field may lead us gaining some insight. Beside that, numerous chemical reactions in nature (*e.g.* cellular respiration, photosynthesis) also incorporate electron-transfer by creating charge imbalance in living organisms, making the experiments on electron transfer process substantially significant for complementing biochemical research.

Single-molecule junctions also include other fundamental issues that describe intrinsic molecular characteristics [18]. For example, thermal conduction at the smallest imaginable length-scale can be realized. Also, the influence of physical quantities like electric field, current, mechanical force on switchable molecules with different chemical and optical properties can be investigated.

Experiments Reported on Molecular Functionalities

I. Conformational Switching

Experiments on individual molecules using scanning tunneling microscope have provided wealth of information on molecular conformations[2] and their mechanical properties [19]. Different mechanisms have been shown to drive individual molecules into distinct conformations. For example, lateral manipulation of molecules on a surface has been shown as a route to conformational molecular switches [20]. Structural bistability of a metalloporphyrin macrocycle was reported to have influenced by electrostatic forces [21]. Investigations have also been performed on a variety of conformational switches based on isomerization. Changes in the conformations of azobenzenes (and derivatives) have been

---

[2]In this section, the term *conformation* refers to the geometrical configuration. In chemistry, *conformation* belongs to a particular class of isomer (see Chapter 2).

achieved on surfaces via *cis–trans* isomerization under the influence of electric field [22], tunneling electrons [23–25], and illumination [26, 27]. However, stronger interaction with the substrates restrains them from switching [28]. Manipulation of a chlorophyll-a molecule among different conformations was also achieved via isomerization [29]. Few examples of electron-induced hydrogen tautomerization have been reported, which reflect conductance switching through alteration of chemical bonds within the molecules [30, 31]. Also, there are examples of thermally induced chiral switching that undergoes conformational changes [32].

II. Manipulation of Molecular Spin

Several examples of the manipulation of molecular spin[3] have been reported from individual molecules, describing the control over spin-electron interactions. Cobalt phthalocyanine, for example, does not show any magnetic property on Au(111). But, its intrinsic magnetic moment can be recovered through dehydrogenation at the phenyl rings [33]. Switching of metalloporphyrin derivative between two different conformations has been reported to have different Kondo temperatures [34]. The control of the spin of individual magnetic adatoms was achieved by changing their local environment through ligand attachment [35]. Similar consequences have been reported from molecules with varying number of nearest neighbors [36]. Oscillation in Kondo temperature has been shown from individual molecules through quantum size effects [37]. Adsorption of molecules with respect to atomic lattice of the substrate has been shown to strongly affect their magnetic properties [38]. Coordination of CO molecules to individual manganese phthalocyanine showed a different magnetic state than an uncoordinated one on the surface [39].

A few examples showing disappearance and reappearance of molecular spin has been reported. Addition of NO molecules to the coordination sphere of cobalt centers in tetraphenylporphyrins was shown to leave the molecule in a diamagnetic state [40]. Reversible spin-control of manganese phthalocyanine molecules was achieved through attachment and detachment of single hydrogen atom to the molecule [41]. Spin of a double-decker molecule has been switched *on* and *off* through the rotations of the upper ligand by controlled current pulses [42]. Metal atoms has been used as spin-dopants in individual molecules to manipulate their magnetic states [43, 44]. Moreover, two examples of spin-crossover molecules—switching between high- and low-spin states when decoupled from the metallic substrates—have been reported [45, 46].

III. Related Work

Bistability in molecular junctions has also been achieved through the mechanically controlled break-junction approach [47–49]. *Chen et al.* demonstrated a molecular switch based on potential-induced changes of oxidation state, showing the role of electrochemical properties of a molecule in electron transport

---

[3]Molecular spin refers to the total spin angular momentum S of the whole molecular system.

[50]. The alteration of a single-molecule junction between two stable states in response to external voltage stimuli has been reported [51]. *Quek et al.* showed reversible binary switching in a single-molecule junction by mechanical control of the metal-molecule contact geometry [52]. Current rectification through chemical substitution of a molecule has also been realized using break-junction technique [53]. Moreover, wealth of examples provided informations on charge transport in molecular junctions through conductance histograms, obtained by forming thousands of metal-molecule-metal junctions using this technique [54–57]. For a detailed review on the evolution of break-junction technique the reader is referred to Ref. [58].

What's New

In this thesis, I, together with coworkers, have been able to show several new aspects of molecular junctions, revealing fundamental details.

For example, the detailed variation of the electrostatic potential in a molecular junction was studied contacting a Mn-porphyrin on Au(111) (see Chapter 4). Hardly any experimental work addressing the voltage drop across a molecular junction has been reported so far, although a few theoretical articles addressed the voltage drop to interpret phenomena such as negative differential resistance or conductance fluctuations [59, 60]. Our result implies that simplistic assumptions—that in a supposedly symmetric single-molecule junction, the applied voltage drops equally on both molecule-electrode interfaces—may not always be valid.

Remote switching over a nanometer distance within a single molecule has been demonstrated for the first time (see Chapter 5). The process, effected by a so called Bailar twist [61], is attributed to intramolecular electron transfer which can be prohibited by changing the chemical composition of the transfer-pathway.

The fabrication of supramolecules with C_5 symmetry, which are mainly found in living organisms, is presented from *all-trans*-retinoic acid (see Chapter 7). These pentamers are found to agglomerate in large arrays with patterns resembling a pentagonal *Cairo* tiling, although regular pentagons are incompatible with filling a planar surface completely. This is the first of its kind that shows two-dimensional arrays comprising supramolecular pentamers only.

Furthermore, the spin states of single bio-molecules are manipulated on a Au(111) substrate (see Chapter 8 and 9). The molecules can be switched selectively between paramagnetic and diamagnetic states by generating and quenching singly charged radical cations.

All these results are discussed in detail in the respective chapters.

2   Experimental Techniques and Fundamentals

A rudimentary description of experimental techniques used throughout the work is given. This includes the functioning of *Scanning Tunneling Microscope* (STM) in view of different measurement modes and the operation of electrospray ionization.

The latter part touches upon the topics that are relevant to the subject matter of this thesis. It contains discussions on *Kondo effect* and the associated characteristic resonances (the *Kondo resonance*). The versatility of chemical structure in terms of isomerism is outlined. The chapter ends with a brief description of the Au(111) surface that is mostly used for hosting molecules.

Scanning Tunneling Microscopy

The ability to image atomic structures and other aspects of the *scanning tunneling microscope*[1] (STM) has been widely applied in *nanoscience*. In this thesis, the technique is used to characterize single molecules which were deposited onto metal substrates.

The STM makes use of *quantum-mechanical tunneling effect*[2] to probe surfaces of conducting samples [4–6]. A sharp metal tip is brought into close proximity of the sample surface, making electrons to tunnel across the gap owing to an overlap of the electronic wave functions of the tip and the sample. This causes finite transmission probabilities of electrons so that a voltage applied between the tip and sample results in a net "*tunneling*" current which decreases exponentially with the tip-sample distance.

Different modes of measurements used for data acquisition are briefly described below. A comprehensive description can be found in Refs. [62, 63].

I. Imaging of Surface-Structures

The topographs presented in this thesis are obtained with the STM operated in *constant-current mode*. In this mode, the tunneling resistance is held constant by a feedback-circuit that adjusts the $z(x, y)$ position of the tip relative to

---

[1]It was developed in 1981 by *Binnig* and *Rohrer* who received the Nobel prize in physics.
[2]the finite probability of finding an electron in regions of space that are classically forbidden

the surface[3]. A contour of constant current is, therefore, followed by the tip revealing surface morphology. The other mode, so-called *constant-height mode*, registers variations in the tunneling current at every (x, y) position of the surface with the tip being at a constant z.

Tersoff and *Hamann* presented a model providing adequate description of STM topographs [64, 65]. The model is based on *Bardeen's* approach to tunneling [66] whereby the system was thought to consist of two independent subsystems with many-particle states: one for the tip and one for the sample. Few assumptions—in particular, the atom at the apex of the tip was considered as the lone contributor to the tunneling processes and assumed to exhibit a spherical s-like orbital wave function, and only elastic tunneling was considered—were made therein. Applications of this formalism have been shown to produce reliable results [67, 68]. However, the *Tersoff-Hamann* model fails to explain the experimentally observed corrugation amplitude[4] of metal surfaces quantitatively [69]. *Chen* explained this discrepancy by extending the model through generalization of s-like tip orbital to arbitrary orbital symmetries [62, 70].

Nevertheless, the absolute value of the corrugation amplitude is a quantity that depends on other quantities like the actual geometry of the tip, the tip-sample distance which are hardly controllable in the experiment. Thus, the results obtained by the *Tersoff-Hamann* approximation can certainly be considered correct qualitatively.

II. Spectroscopic Measurements

Spectroscopic data are used to investigate the electronic properties of samples. The energy-dependent differential conductance dI/dV is acquired over a position of the surface with the tip held at constant height (determined by the chosen value of current I and voltage V prior to opening the feedback loop). The dI/dV spectrum is proportional to the energy-dependent local density of states of the sample at absolute zero temperature [71, 72], assuming a constant density of states of the tip and a monotonically varying barrier transmission probability with voltage. *Stroscio et al.* showed that the ratio of differential to total conductance $(d\ln I/d\ln V)$ obtained with the STM yields a close correspondence to spectral density of the surface electronic structure [73], which was later verified theoretically by *Lang* [74].

Usually, a lock-in amplifier is used in the experiment to record the spectra (likewise the data presented in this thesis) rather than differentiating $I(V)$ curves numerically. The reason is that a higher signal-to-noise ratio is achieved with the former technique, whereas to avoid $1/f$ noise (f denotes frequency) from numerically differentiated curves is difficult. The lock-in technique modulates the actual voltage signal with a certain frequency[5] that shifts the measure-

---

[3]The surface is assumed to be parallel to the xy plane.

[4]defined as the difference between the largest and smallest tip-sample distance in *constant-current mode*

[5]In certain cases we are limited by the low bandwidth of current amplifier.

ment to a noise-free domain, thereby enhancing the measurement[6] sensitivity.

Care should be taken not to misinterpret the features of the spectrum arising due to the structure of the tip. For example, *Vázquez de Parga et al.* have showed (both by experiment and calculations) that a (111) *bcc* structure of a tungsten tip (blunt tip) shows the characteristic feature of the Cu(111) surface state in differential conductance spectrum, while the spectrum obtained with (111) *fcc* tips (sharp tip) displays two sharp resonances corresponding to the tip states close to Fermi energy [75]. To avoid such inconsistencies, the tips were always tested by taking spectra on bare substrates before and after the data acquisition. Only those tips that showed appropriate spectra—for example, the appearance of the surface state of Au(111) around ~ 480 meV below the Fermi energy [76, 77]—were used.

The influence of the finite temperature to the lock-in output and the additional broadening induced by the lock-in itself have to be considered for analyzing the detected dI/dV signal [78]. However, as long as the broadening due to lock-in is smaller than the unavoidable thermal broadening, the former one can be neglected [79].

III. Contact Experiments

The electron transport through single atoms or molecules is studied by performing controlled experiments with the tip at contact to the adsorbate. In practice, the conductance spectrum ($I(\Delta z)$, Δz represents tip displacement) is recorded when the tip is approached towards the surface at a constant voltage with an inoperative feedback loop. A sharp jump or a rapid increase of conductance indicates (cf. [11, 80]) transition to contact from the tunneling regime[7]. The point of intersection between the transition and contact regimes defines the point-contact and hence, the contact conductance.

These quantum *point-contacts*[8] are described by the Landauer formula [83, 84] that relates electrical conductance (G) to the transmission probability τ_i of individual eigen modes (so called conductance channel) as $G = (2e^2/h) \sum \tau_i$. $2e^2/h$ refers to the conductance quantum with h being the Planck's constant and e, the electronic charge. The Landauer formula for multiple quantum channels [85] has been applied to different geometries as well [87, 88].

---

[6] In practice, some details have to be considered. For example, the modulation frequency should be chosen such that the data-acquisition time at each step of the entire voltage range is large compared to the time period of the modulation voltage. The phase between the input and the reference signal should be adjusted correctly—in particular, if the tunneling resistance is high compared to the reactance of the junction capacitance where the signal arising due to capacitive reactance may prevail over the actual signal—in order to obtain accurate output.

[7] From $I(\Delta z)$ curves recorded in the tunneling regime, the apparent barrier height may be extracted [81].

[8] Dimensions are comparable to the Fermi wavelength [82]. Ohm's law fails to describe electron transport through these quantum conductors.

Electrospray Ionization

Electrospray Ionization is one of the established techniques used in mass spectrometry, especially useful in producing ions from macromolecules. In the present work the technique was used for the deposition of fragile and non-volatile molecules on surfaces in ultra-high vacuum, since the thermal evaporation technique could not be applied to substances that are thermally unstable.
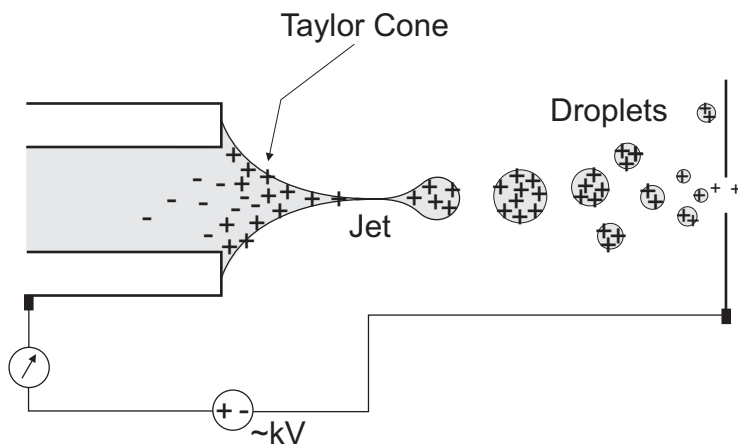

Figure 2.1: Schematic shows the electrospray ionization process. The solution containing analytes is sprayed from a needle to which a high voltage (positive in this case) is applied. The electric field gradient between the needle and the counter electrode results in an excess of positive charge on the liquid surface at the tip of the needle and a *Taylor cone* is formed. The released droplets shrink due to repeated coulomb fission and the gas phase ions are generated.

The electrospray is generated by exposing colloids or solutions containing the analytes to a high electric field at the apex of a metallic emitter [89, 90]. Colloid/solution reaching the tip of the emitter gets polarized and opposite charges are directed in accordance with the direction of the electric field (Fig. 2.1). This induces accumulation of similar charges at the tip of the emitter, leading to mutual coulombic repulsion that deforms the liquid meniscus into the shape of a cone, known as *Taylor cone* [91]. At a sufficiently high field, electrostatic forces overcome the surface tension and liquid is released in form of a jet, which then breaks into droplets. The *Rayleigh instability* [92, 93] leads to the shrinkage of droplets through repeated coulomb fission [94]. The solvent evaporates, leaving an aerosol of analytes in air.

The capability of transforming ions from solution to the gas phase makes this technique useful in analyzing thermolabile substances. Recently, it has become as one of the deposition techniques to deal with fragile macromolecules [95–98].
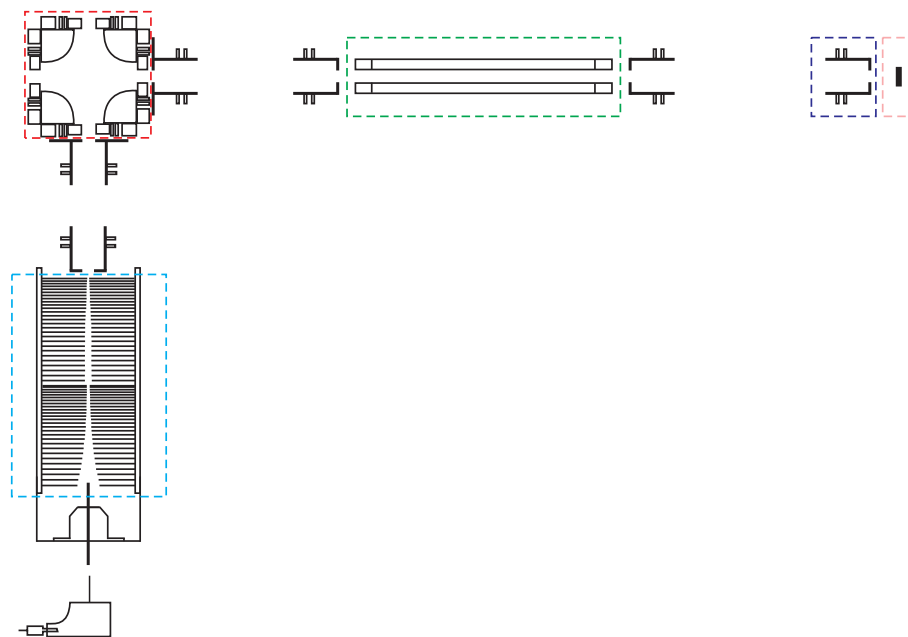
Figure 2.2: Schematic of Electrospray Ionization deposition instrument. The ion funnel, composed of a series of ring electrodes of successively decreasing inner diameters, is confined in cyan dotted rectangle. The red square accommodates electrostatic quadrupole deflector that acts as an energy filter. The quadrupole mass spectrometer and the position of the sample are surrounded with green and pink rectangle, respectively. The part confined in blue rectangle depicts one of the ion optical lenses that are used to focus the ion beam.

In a set-up developed in our laboratory [99], ions, produced[9] at atmospheric pressure, are guided into the vacuum through an ion funnel (Fig. 2.2, the part contained within the dotted cyan rectangle). An alternating radio-frequency voltage accelerates the ions towards the funnel axis, while an applied electrostatic potential drags the ions to the exit of the funnel. At the next stage, neutral contaminants are restricted from reaching the high vacuum chambers by an electrostatic quadrupole deflector (Fig. 2.2, surrounded by the red dotted square), that purifies the ion beam. The quadrupole deflector also acts as an energy filter. The difference in potentials (ΔV_q) applied to the pairs of rods of the quadrupole is taken, in close approximation, as the mean kinetic energy per charge of the ions passing the deflector [100, 101]. A quadrupole mass filter (Fig. 2.2, the part within the dotted green rectangle) is then operated to select analytes of desired mass to be moved forward into ultra-high vacuum where the deposition takes place. The flux of molecular ions is perceived as ion current[10] (I_{ion}) allowing estimation of molecular density on the substrate. The prepared samples are then directly transferred to a cryogenic STM, attached to the electrospray set-up, for further characterization. A detailed description of this instrument can be found in Ref. [102].

The mean impact energy per charge (E_{im}) of the ions reaching the substrate is estimated as $E_{im}/e = \Delta V_q + V_{q(av)} - V_{sub}$ with $V_{q(av)}$ being the average potential applied to the rods of the quadrupole deflector and V_{sub}, the potential applied to the substrate and e, the charge of the ions.

---

[9]In most of the cases, molecular ions are produced by the dissolution (addition) of ions (such as hydrogen) from (to) the molecules rather than creating radical ions. But the type of ion produced from a particular analyte depends on the used solvent, concentration of solution etc.

[10]The time t required to cover a surface of area A_s with molecules carrying charge Q_{ion} individually is estimated as $t = A_s/A_m \cdot Q_{ion}/I_{ion}$, with A_m being the surface area covered by a molecule. Usually, it takes few hours to cover $1/10$ th of the surface with the molecules.

Kondo Resonance: The Fingerprint of Atomic/Molecular Spin

Scanning Tunneling Spectroscopy (STS) studies on magnetic atoms and molecules on metal surfaces often show Kondo fingerprints [33, 38, 42, 103–107], the characteristic resonances arising due to the *Kondo effect* [108, 111].

The presence of a magnetic impurity in non-magnetic metal leads to interactions between the localized spin moment ($S = 1/2$) of the impurity and the spin of the electrons in the conduction band, giving rise to the *Kondo effect* at low temperatures. Higher temperatures lead to the dominance of electron-phonon interactions in the metal over the interactions of the magnetic impurity with the conduction electrons. Below a characteristic temperature, the *Kondo temperature T_K*, the scenario changes and the local magnetic moment of the impurity is screened by the conduction electrons of the metallic host, leading to the formation of a many-body ground state possessing a resonance around Fermi energy, named the *Kondo resonance*.

To a crude approximation, these resonances are modeled with a Lorentzian function $\delta(\epsilon) \propto \frac{\Gamma_L^2}{\Gamma_L^2 + \epsilon^2}$ with Γ_L being the half width of the resonance at the half maximum. At temperature $T = 0$, Γ_L is proportional to the Kondo temperature (T_K) and is expressed as $\Gamma_L = k_B T_K$ with k_B being the Boltzmann constant. For $T \ll T_K$ (strong coupling regime), the width Γ_L becomes equal to $\frac{1}{2}\sqrt{(\alpha k_B T)^2 + (2k_B T_K)^2}$ with $\alpha = 2\pi$ [110].

The shape of the resonance—not always appears as a peak, rather a dip or an asymmetric feature is obtained—gives an insight into the tunneling channels involved in the process. The interference between two tunneling paths [111]—a direct tunneling into the conduction band as well as tunneling into the Kondo-impurity—eventually determines the shape of the resonance that can be modeled by the function described by *Fano* [112]. The functional form of a Fano line-shape is given as: $\delta(\epsilon) \propto \frac{(q + \tilde{\epsilon})^2}{1 + \tilde{\epsilon}^2}$, where q is the asymmetry parameter and $\tilde{\epsilon} = \frac{\epsilon - \epsilon_0}{k_B T_K}$, with ϵ_0 being the position of the resonance. $q = 0$ corresponds to a dip in the conductance at zero bias, whereas in the limit of $q \to \infty$ the Lorentzian peak is recovered. Other values of q give asymmetric shapes.

A more accurate *Frota* function [113, 114] has been used recently for describing zero-bias anomalies [37, 115–117]. The supremacy of *Frota* function is also justified by *numerical renormalization group* (NRG) calculations [118]. The *Frota* function has the following form: $\delta(\epsilon) \propto -Im\left[(ie^{i\phi}\left(\frac{i\Gamma_F}{\epsilon - \epsilon_0 + i\Gamma_F}\right)^{\alpha}\right]$, where $\alpha = 1/2$ and ϵ_0 is the position of the resonance. At $\phi = \pi$, the resonance appears as a symmetric peak with a half width of $2.542 \cdot \Gamma_F$ at the half maximum [115]. The width parameter Γ_F is proportional to the Kondo temperature and can be given as $\Gamma_F = \gamma \cdot k_B T_K$. The exact value of the prefactor γ is an issue. $\gamma = 1.454$ has been predicted from NRG calculations [119], whereas $\gamma = 1.545$ has been reported elsewhere [114, 120].

Basic Terminology of Stereochemistry

As this thesis deals with single molecule analysis, different chemical terms are often used in order to refer to specific structures or to describe certain processes. Although it is difficult to address the needs of all scientific communities with a single document, this section will provide a basic understanding in ways useful to the intended readership. A comprehensive description can be found in any of the standard textbooks dealing with organic chemistry [121].

I. Isomerization

Isomerization leads to transformations of chemical compounds into other forms that have exactly the same chemical formula. These conversions result in *isomers* which are categorized on the basis of structural or spatial arrangement of the constituent atoms (Fig. 2.3).

In *structural isomers*, the atoms are arranged in completely different order. The isomers may contain different bond types as well. The form of isomerization that creates *structural isomers* excludes arrangements which are simply due to the molecular rotation as a whole, or the rotation of a functional group about particular bond. Structural isomers are divided into different groups based on the type of isomerization. For example, chain isomerism occurs due to the possibility of branching in hydrocarbon chains (Fig. 2.3a). In position isomerism, particular groups or atoms are moved around on a carbon skeleton (Fig. 2.3b). Isomers that belong to different families of compounds containing different functional groups (*e.g.* –OH, –CHO) are called functional group isomers (Fig. 2.3c). The interconversion between two structural forms through changes in positions of hydrogen atoms within the molecule results in *tautomers* (Fig. 2.3d).

In contrast, *stereoisomers* must contain the same sequence of bonded atoms. This class includes *enantiomers*, which are non-superimposable mirror-images of each other (Fig. 2.3e), and *diastereomers*, which are not. The diastereomers encompass conformational isomers (*conformers*) and *cis/trans* isomers (Fig. 2.3f). Conformational isomers interconvert themselves through rotations about single bonds and are thus different from other classes of *stereoisomers*. *cis/trans* isomers describe the relative orientations of functional groups within a molecule.

II. Torsion Angles and Klyne-Prelog Nomenclature

In a chain of atoms A–B–C–D (Fig. 2.4a), the angle (having an absolute value between 0 and 180 degree) between the projections of A–B and C–D onto a plane normal to the bond B–C is referred to as the torsion angle θ (named interchangeably with dihedral angle) around the bond B–C. This angle may also be described as the angle between the plane containing atoms A, B and C, and the plane containing atoms B, C and D [122, 123].

If the precise torsion angle for a conformation is not known, the Klyne-Prelog notations [124] are used to roughly specify a range in which the torsion angle lies. Two particular conformers in the Klyne-Prelog nomenclature are
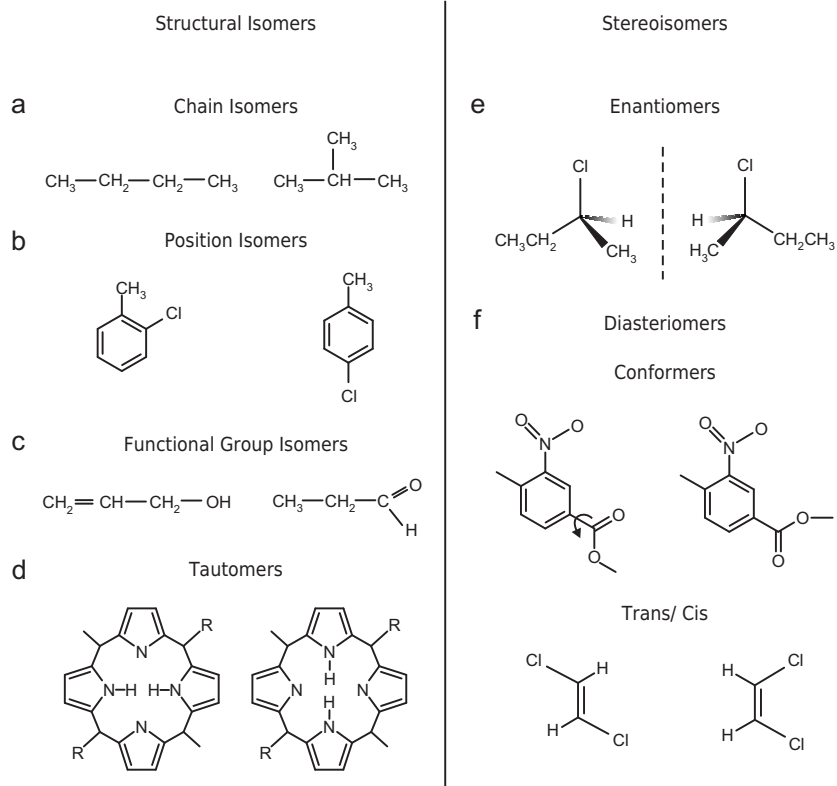
Figure 2.3: (a–d) A variety of structural isomers: (a) *Chain isomers* of butane (C_4H_{10}). (b) Examples of *position isomers* with chlorine (Cl) at two of the possible positions with respect to methyl (CH_3) group attached to a benzene ring. (c) *Functional group isomers*: a molecular formula C_3H_6O can either possess an –OH (an alcohol) or a –CHO group (an aldehyde) through the rearrangement of bond order. (d) *Tautomers* of a porphyrin resulted from the movement of H atoms through the shifting of bonding electrons. (e) Structures are mirror images of each other and are, thus, called *enantiomers*. (f) *Conformers*: Isomers produced by rotation about a single bond (marked with curved arrow). *cis/trans* isomers: Chlorine atoms of 1,2-Dichloroethene are on opposite sides of the double bond in *trans* form, whereas both the chlorine atoms are on the same side in *cis* form. No rotation of the double bond is occurred.
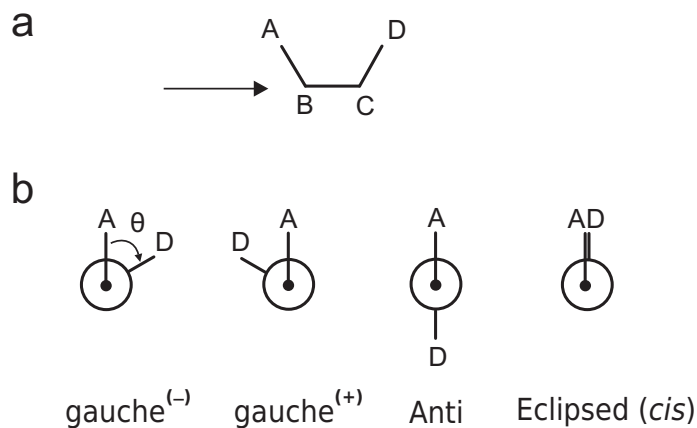
Figure 2.4: (a) A system involving four backbone atoms connected by three covalent bonds. (b) Newman projection of different conformations, when looking lengthwise down the bond B–C (arrow in (a)). $\theta = 60°$ corresponds to *gauche*(-), whereas a torsion angle of $-60°$ refers to *gauche*(+) conformation.

noteworthy and have special names [123]. A torsion angle of $\pm 60°$ is called *gauche*, whereas $\theta = 180°$ refers to the *anti* conformation. $\theta = 0°$ corresponds to the eclipsed conformation (which is simply the *cis* conformation).

These conformations are better viewed using a Newman projection [125] that represents the head-on look (arrow in Fig. 2.4a) down the bond of interest—in this case, the bond B–C. The atoms connecting the bond are represented with a dot (the atom in front, B) and a circle (the atom at the back, C). Few of the conformers in the Klyne-Prelog nomenclature are depicted in Fig. 2.4b as examples. When the bond to the front needs to be rotated clockwise (counterclockwise) in order to eclipse the bond at the rear, the angle θ is considered positive (negative).

Au(111)

For the experiments presented in this thesis, Au(111) substrates were mostly preferred due to their low catalytic activity. Gold exhibits a *face-centered cubic* (*fcc*) structure with a lattice constant of 4.08 $\mathring{A}$. An uniaxial compression of the topmost atomic layer along one of the three $\langle 1\bar{1}0 \rangle$ directions leaves the surface of Au(111) in a reconstructed $(22 \times \sqrt{3})$ superstructure, known as *herringbone reconstruction* [126, 127]. The formation of mesoscopic domains (called as '*stress domain*') under long-range elastic interactions has been shown to be the reason for this characteristic pattern [128]. Domain walls (ridges) separate the areas with surface atoms in *fcc* and *hcp* regions that appear in a parallel zig-zag pattern with a periodicity of 63 $\mathring{A}$ [76].
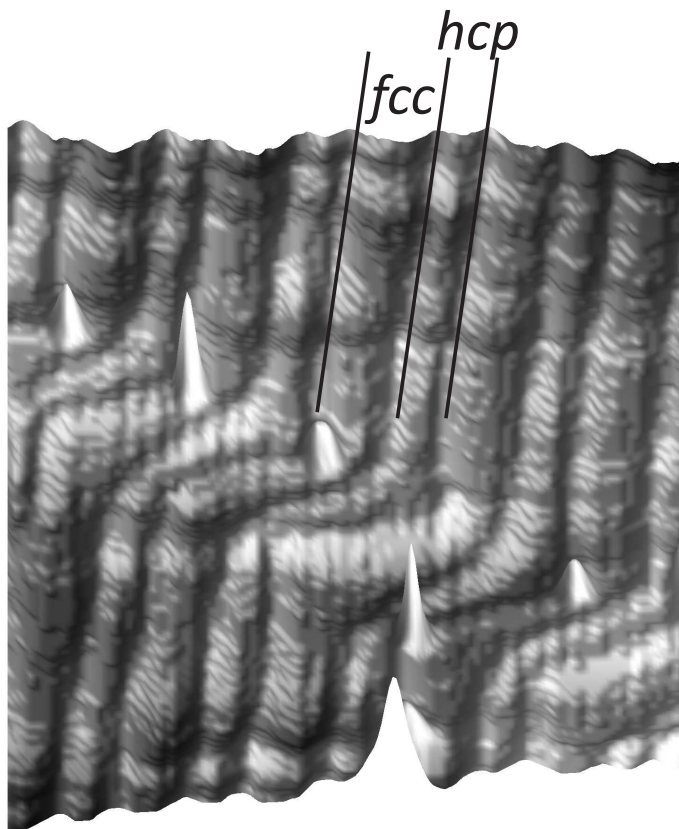

Figure 2.5: Constant current 29.7×41 nm^2 image of the Au(111) surface ($I = 30$ pA, $V = 1.5$ V). The image is displayed in pseudo three-dimensional fashion. The herringbone reconstruction is clearly visible. Molecular fragments are trapped at the reactive elbow sites.

3   An Overview of the Apparatus

This part of the thesis briefly describes the instruments used for the experiments. Relevant details of the setup are provided.

The STM and Control Systems

The majority of data presented in this thesis has been acquired with a commercial Besocke-beetle type [129, 130] scanning tunneling microscope (STM) from CreaTec[1]. The scanning head is attached to the base of the cryostat[2] via three stainless-steel springs that take part in vibration isolation. Both the STM head and the inner cryostat have got eddy current damping. Two radiation shields—the inner one is kept at liquid He temperature—isolate the STM head from thermal radiation. A sample temperature of $\sim$ 5 K is achieved (without pumping the cryostat).

The piezoelectric tube-scanners are driven by high-voltage amplifiers (output range of ±200 V). A gain of 6 $\mathring{A}$/V (12 $\mathring{A}$/V) is used for the vertical[3] (lateral) motion of the piezos, yielding a full-scale dynamic range of 0.24 μm in the direction perpendicular to the sample surface (0.48 μm laterally).

A transimpedance amplifier[4] is used in the feedback-circuit. It has a bandwidth of 1.1 kHz (7 kHz) at the gain of 10^9 V/A (10^8 V/A). The STM is controlled through CreaTec STM-program (which has been replaced by Nanonis-program later on) running on Windows XP.

Overview of the Whole Setup

The ultra-high vacuum chamber containing the STM (base pressure $\sim$ 4 $\cdot$ 10^{-11} mbar) is attached to a preparation chamber (PC) and can be isolated via a pneumatic gate valve. A base pressure of $\sim 2.5 \cdot 10^{-10}$ mbar is maintained in PC with the help of a turbo-molecular pump, a ion getter pump and a titanium sublimator (used when necessary). The samples and tips are inserted

---

[1] http://www.sps-createc.com
[2] The cryostat consists of two concentric cylinders—the inner cylinder is filled with liquid He, whereas the outer one contains liquid N_2.
[3] perpendicular to the sample surface
[4] Femto DLPCA-200, http://www.femto.de

into the PC from a load-lock—separated from the PC via a second pneumatic gate valve—using a transfer rod. The PC is equipped with the following: *(i)* a manipulator – for introducing samples and tips into the STM, *(ii)* a storage station – as many as four samples and six tips can be stored, *(iii)* an ion gun – for sputtering the samples, *(iv)* an evaporator – for sublimating molecules, *(v)* a mass spectrometer – for analyzing residual gas molecules, and *(vi)* a quartz balance – for monitoring the thickness of molecular film .

The PC is combined with a home-built Electrospray Ionization (ESI) setup [99] via an another gate valve. ESI consists of five stages which are pumped differentially when in operation. This apparatus is used for depositing fragile macromolecules onto surfaces[5]. During deposition using ESI, the pressure in the PC goes up to $\sim 1 \cdot 10^{-9}$ mbar. An Extrel Merlin Automation 5221 Series Scan and Resolution Controller is used to operate the ESI setup. A detailed description of this instrument can be found in Refs. [102].

The complete setup is placed on pneumatic vibration-isolators to reduce the influence of building vibrations.

The Tips and Samples

Tips were electrochemically etched from tungsten (W) wire of a diameter of 0.25 mm. They were then heated (to approximately $\sim 1000°C$) for a short period of time (< 15 s) by electron bombardment. This is sufficient to remove any contamination as well as oxide film covering the W tip. They were further treated *in situ* by indentation into the substrate during the experiments.

Nobel metal surfaces have been used as substrates. They were mounted on small resistive heaters, fixed to the sample holders, with a NiCr/Ni thermocouple attached to them for monitoring the temperature. Prior to the deposition of molecules, the substrates were cleaned by repeated cycles of Ne^+ or Ar^+ ion sputtering and subsequent annealing (to about ~ 775 K). An ion-beam energy of 0.8–1.2 keV was used for sputtering to achieve an ion current of ~ 10 μA.

---

[5]The substrates can be cooled through the manipulator with liquid nitrogen or helium, therefore providing a wide range of sample temperatures during the deposition of molecules.

4 Shifting the Voltage Drop in Electron Transport Through a Single Molecule

This chapter is based on a manuscript accepted in Physical Review Letters [131].

Abstract

A Mn-porphyrin was contacted on Au(111) in a low-temperature scanning tunneling microscope (STM). Differential conductance spectra show a zero-bias resonance that is due to an underscreened Kondo effect according to many-body calculations. When the Mn center is contacted by the STM tip, the spectrum appears to invert along the voltage axis. A drastic change in the electrostatic potential of the molecule involving a small geometric relaxation is found to cause this observation.

Introduction

The spin states of molecules at surfaces are intriguing because of the interaction of localized molecular orbitals with delocalized substrate states. When a molecular spin is screened by delocalized electrons, the Kondo effect may be observed, which gives rise to a characteristic anomaly in the excitation spectrum close to the Fermi energy [33, 38, 42, 105–107]. Several approaches are being explored to control molecular Kondo systems at surfaces. These include the application of electric fields [132], mechanical deformation [133], chemical modification of the ligand shell [39–41, 134], and electronic excitation followed by spin state trapping [45, 46].

In purely metallic systems, the proximity of a metal tip in a scanning tunneling microscope (STM) has been shown to modify the Kondo effect through changes of the Co d band and exchange interaction [135–137]. It seems natural to extend this method to the spin states of metal complexes using the tip as an additional ligand. By moving the tip, the ligand strength may be continuously modified with the subsequent changes in the local environment of the molecule, making this approach particularly appealing. The concomitant forces were observed to lead, in extreme cases, to the transfer of an atom or molecule from the sample to the tip [138, 139].

Moreover, the electrostatic potential at the molecule may be modified. Although the electrical field in a nanoscopic junction is fundamentally interesting and drives current through the molecule little is known about it from experiments. Usually, it is assumed that the states of an adsorbed molecule are pinned with respect to the Fermi level of the substrate. A voltage drop between molecules and their substrate has been reported in cases where the molecules or parts of them were decoupled from a metal substrate by insulating layers [140–142] or by a particular geometric arrangement such as rod-shaped molecules adsorbed vertically [143] or molecular double-deckers [144]. The question of the voltage drop within a molecular junction has been addressed by non-equilibrium *ab initio* quantum transport calculations. These calculations show that most of the voltage drops at the weakest bond of the junction [145, 146]. Calculations also indicate that a voltage drop between molecule and substrate may lead to negative differential resistance [59] and two-level fluctuations [60] of C_{60} junctions as well as rectification in a molecular wire [147].

Here we present STM data and results of *ab initio* calculations for a metal complex on Au(111). In the limit of weak interaction with the STM tip the complex exhibits an underscreened high-spin Kondo effect. When the tip is moved closer to the metal ion, the differential conductance spectrum changes drastically. It turns out, however, that this change is due to sub-Angstrom structural relaxations. Similar to a mechanically operated switch, the voltage drop over the junction moves from the tip–molecule gap to the molecule–substrate bond.

Results and Discussion

Purified 5, 10, 15, 20-tetrakis(4-sulfonatophenyl)-21H, 23H-porphine manganese (III) chloride (MnTPS-Cl) was dissolved in aqueous methanol in the presence of 1 vol% acetic acid. Mass-selected singly charged MnTPS cations originating from the dissolution of Cl ions were electrosprayed onto clean Au(111) surfaces in ultrahigh vacuum (UHV) [99]. Thus prepared samples were cooled to 77 K and subsequently transferred into a STM, which was operated at $\sim$ 5 K in UHV. Tips were electrochemically etched from tungsten wire and further prepared *in situ* by indentation into the substrate. A sinusoidal modulation (2 mV$_{\mathrm{rms}}$, 1.2 kHz) was added to the bias to record spectra of the differential conductance.

Figure 4.1a schematically shows MnTPS, which hosts a Mn ion at the center of a tetraphenylporphyrin with four sulfonyl hydroxide (–SO$_3$H) groups occupying *para* positions of the phenyl rings. When adsorbed on Au(111), the molecules appear quatrefoil shaped in STM topographs at positive sample voltage V (Fig. 4.1b), as typically observed for porphyrins and phthalocyanines [38, 106, 134]. One of the molecular C_2 axes preferably aligns along a $\langle 0\bar{1}1 \rangle$ direction of Au(111) within the agglomerates. However, deviations of $\approx \pm 5°$ from this orientation were observed. Slight variations in apparent heights among the lobes of a particular as well as of different molecules are likely due to incommensurability with the substrate lattice. This structural variability may indicate a
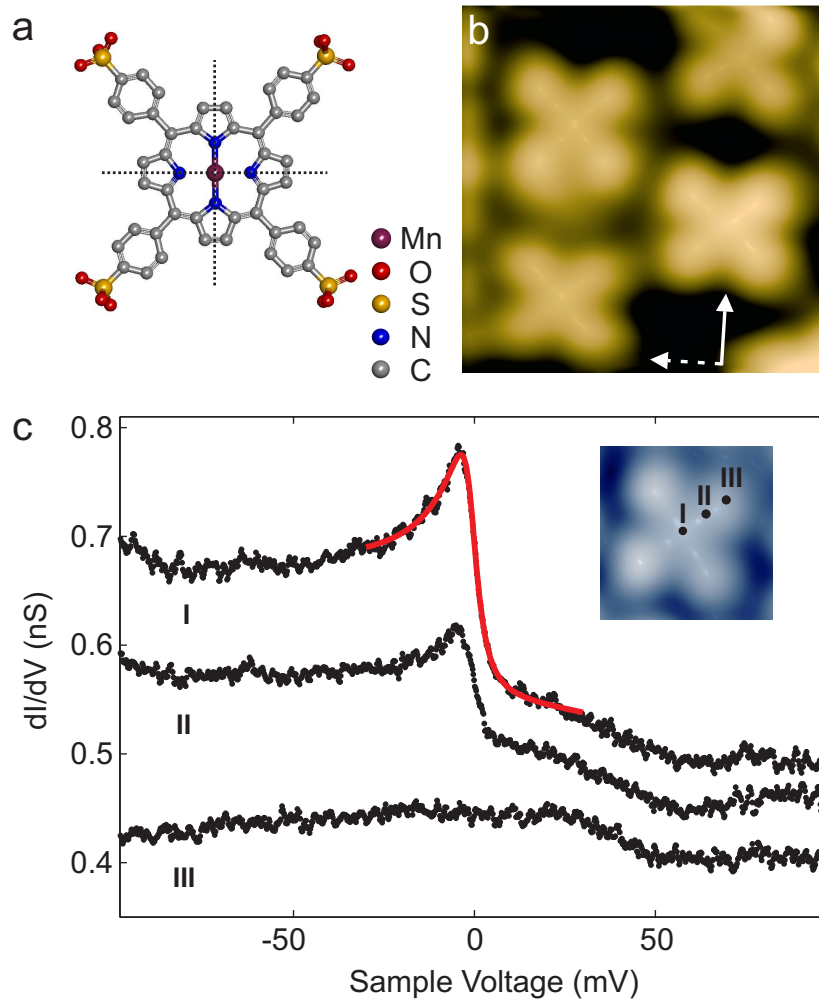
Figure 4.1: (a) Structure of MnTPS (H atoms not shown). Dotted lines through pairs of opposite pyrrole units indicate C_2 axes. (b) STM topograph (4×4 nm^2, sample voltage $V = 2.65$ V, current $I = 50$ pA) of MnTPS agglomerated into an island on Au(111). The data are displayed in a pseudo three-dimensional fashion. The apparent height of the molecular lobes is ≈ 0.28 nm. Solid and dashed vectors indicate a $[0\bar{1}1]$ and $[\bar{2}11]$ directions of Au(111), respectively. (c) Spatial evolution of dI/dV spectra of MnTPS. Dots in the inset indicate the positions of the measurements (spectrum **I** above the molecular center, spectrum **III** at the center of a lobe). For clarity, spectra **II** and **III** are shifted by -0.05 and -0.1 nS, respectively. The solid red line depicts a Frota fit to spectrum **I**.

fairly weak molecule–substrate interaction as expected for Au.

dI/dV spectra measured over various positions of the molecules are shown in Fig. 4.1c. Above the Mn center (spectrum **I**) a resonance is observed close to zero bias, which continuously vanishes as the tip is moved sideways onto a lobe (spectra **II** and **III**). Following previous reports from metals [111] and metal porphyrins [105, 148], we attribute the resonance as a signature of the Kondo effect. The spectrum of the Mn center may be described well by a Frota line [114, 116] (solid red line) leading to an estimated Kondo temperature $T_K \sim 100$ K [1]. T_K measured from different molecules scattered in the range $100(7)$ K. No systematic effect of the position of a molecule in the agglomerates on the line shape was observed.

Next, the tip was brought closer to the center of a molecule until contact was reached. Data recorded for a molecule in a *fcc* region of the Au(111) reconstruction are shown in Fig. 4.2a. Δz is the displacement of the tip from its initial height defined by $V = 100$ mV and $I = 0.05$ nA. The abrupt rise of the conductance at $\Delta z = 0.33$ nm signals the transition to contact.

dI/dV spectra were acquired by holding the tip at predetermined heights over the molecular center (Fig. 4.2b). Spectra recorded in the tunneling range exhibit similar line shapes (only spectra corresponding to $\Delta z = 0$ are shown). At contact, a resonance near zero bias is still observed but surprisingly the line shape appears to be inverted on the voltage axis. Further approach of the tip from the point of contact does not change the shape of the spectrum. Approach of the tip beyond ~ 0.03 nm from the point of contact usually led to the destruction of the junction. Very similar Kondo temperatures (~ 100 K) are obtained from the fits of Frota line shapes to both the tunneling and contact spectra. Tunneling spectra ($\Delta z = 0$) recorded after the contact experiment were unaltered (bottom curve in Fig. 4.2b), excluding the possibility that an irreversible change of the tip or the molecule occurred at contact. Isolated molecules, which were prepared by manipulation with the tip, exhibited tunneling characteristics virtually identical to that of the molecules in the agglomerates (Fig. 4.2b). However, at contact isolated molecules were usually unstable.

At first glance, it may seem natural to attribute a changed Kondo line to a modified molecular spin state. On the other hand, it appears difficult to interpret the observed inversion of the line in such a scenario. We therefore performed DFT based *ab initio* electronic structure and transport calculations to investigate to what extent the Kondo physics is modified by the proximity of the tip. The calculation explicitly takes into account the strong dynamic correlations originating from the Mn $3d$-shell that give rise to the Kondo effect [149–151]. First, the MnTPS molecule was relaxed in the junction between the Au(111) substrate and the STM tip, modeled by a small Au pyramid built in the [111] direction, using VASP [152, 153] with the PBE functional [154] and

---

[1]Different definitions of the Kondo temperature exist in the literature. For the sake of comparability to the Kondo temperatures extracted from previous STM experiments we use the definition that relates T_K to the half width at half maximum of the symmetric resonance. This gives $k_B T_K = 2.54\Gamma$, where k_B is the Boltzmann constant and the width Γ of the Frota line is defined in [116].
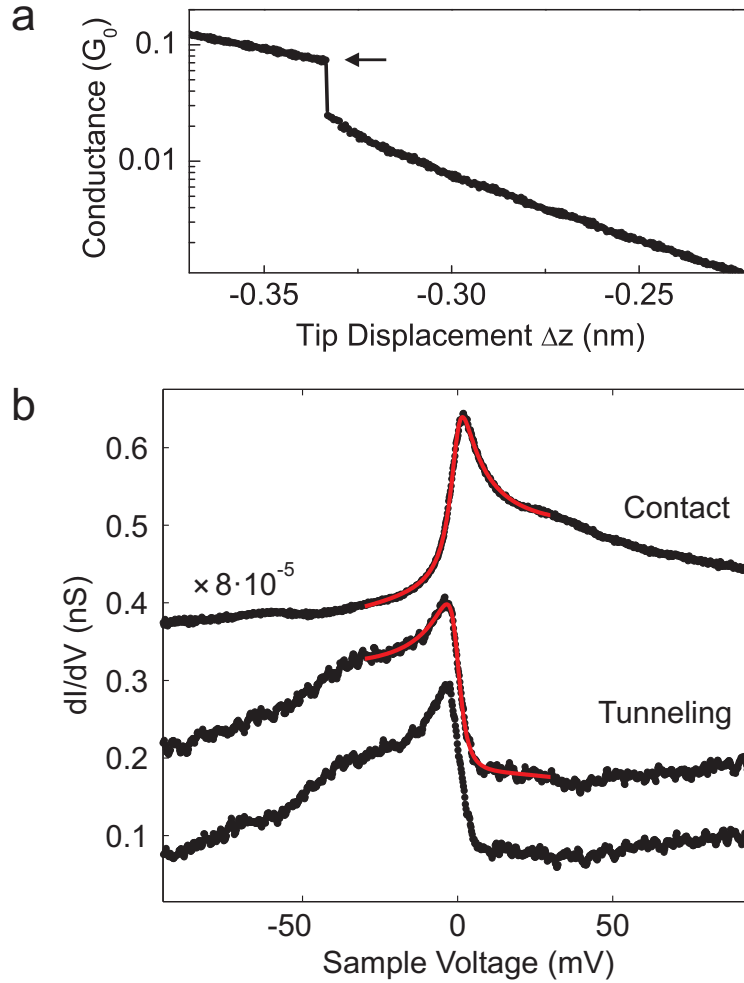
Figure 4.2: (a) Conductance vs. displacement Δz of the tip from the tunneling condition ($\Delta z = 0$ at $V = 100$ mV and $I = 0.05$ nA) towards contact at the center of a MnTPS molecule. At contact formation (arrow) the conductance is $0.074\ G_0$ with $G_0 = 2e^2/h$ being the conductance quantum. The conductance measured from different molecules scattered in the range of $0.07 \pm 0.03 G_0$. (b) dI/dV spectra acquired at $\Delta z = 0$ (tunneling) and 0.33 nm (contact) at the center of a molecule. The bottom two curves are shifted by -0.45 and -0.35 nS, respectively, for clarity. Solid red lines show fits of Frota functions in the range of ± 30 mV.

31

the dispersion correction due to Grimme [155] (see section I of the Supporting Information for details). Figures 4.3a and 4.3b show the resulting structures in the tunneling regime and at contact, respectively. Without the tip, the Mn center is found to be at a height of 2.77Å above the surface. When the tip is brought closer to the Mn center, the molecule is lifted from the surface. At contact (tip at a height of 6Å above the surface [2]), the displacement of Mn center is ≈ 0.7Å.

In order to determine the dynamic single-particle broadening $\Gamma_d(\omega)$ of the Mn $3d$-levels due to the coupling to the organic framework of the molecule, the substrate and the tip, DFT-based transport calculations were performed using the ANT.G code [156]. To make the calculations computationally feasible we replaced the sulfonatophenyl groups of the molecule by hydrogen atoms, which leaves the local environment of the Mn center unchanged. Figure 4.3c shows $\Gamma_d(\omega)$ of the $3d_{z^2}$ orbital, which is the only orbital that couples directly to the s-type conduction electrons of the substrate (similar to MnPc [151, 157]) and effectively binds to the s-level of the Au tip atom (details in the Supporting Information, Fig. 4.5). Hence, the $3d_{z^2}$ orbital is essentially the only d-orbital that responds to the lifting of the molecule from the substrate. In the tunneling regime the broadening is featureless around the Fermi energy E_F (Fig. 4.3c, solid red line), while the coupling to the s-level of the tip at contact leads to a broad feature at ≈ 1.2 eV above E_F (Fig. 4.3c, dashed blue line). The concomitant increased broadening at E_F is partially compensated by reduced coupling to the substrate.

To capture correlation effects beyond the mean-field approximation, the Mn $3d$-shell was augmented by a Hubbard interaction term that takes into account density–density interactions and Hund's rule coupling. We assume an intra-orbital repulsion $U = 4.5$ eV, an inter-orbital repulsion $U' = 3.1$ eV and a Hund's coupling $J_H = 0.7$ eV [3]. The one-crossing approximation (OCA) [158] was used to solve the multi-orbital Anderson impurity model of the Mn $3d$-shell coupled to the rest of the system. The solution yields the spectral function of the Mn $3d$-shell $A_d(\omega)$ (see Supporting Information, Fig. 4.6). Only the $3d_{z^2}$ orbital couples to the conduction electrons near E_F and thus shows a Kondo resonance. While the width of the resonance is comparable to that of the dI/dV spectra recorded in the tunneling regime, a slightly broader resonance appears at contact due to a small increase of $\Gamma_d(E_F)$ and charge fluctuations of the $3d_{z^2}$ orbital (see Supporting Information). The total spin of the Mn $3d$-shell is found to be approximately 1.7, $i.$ $e.$ half-way between spin-3/2 and spin-2 systems. Hence MnTPS displays an underscreened high-spin Kondo effect.

To obtain the low-bias transport properties of the system we calculated the transmission function $T(\omega) = \mathrm{Tr}[\hat{\Gamma}_\mathrm{T}(\omega)\hat{G}_\mathrm{M}^\dagger(\omega)\hat{\Gamma}_\mathrm{S}(\omega)\hat{G}_\mathrm{M}(\omega)]$, where $\hat{G}_\mathrm{M}(\omega)$ is the correlated Green's function of the extended molecule that contains the Kondo resonance. $\hat{\Gamma}_\mathrm{T}$ and $\hat{\Gamma}_\mathrm{S}$ are operators describing the coupling to the tip and

---

[2]At tip heights exceeding 6Å above the substrate the molecule was not lifted further. We thus define 6Å as the point of contact

[3]These values are slightly smaller than the ones used for MnPc [151, 157]. However, the results are hardly affected by changes of these parameters by up to 30%.
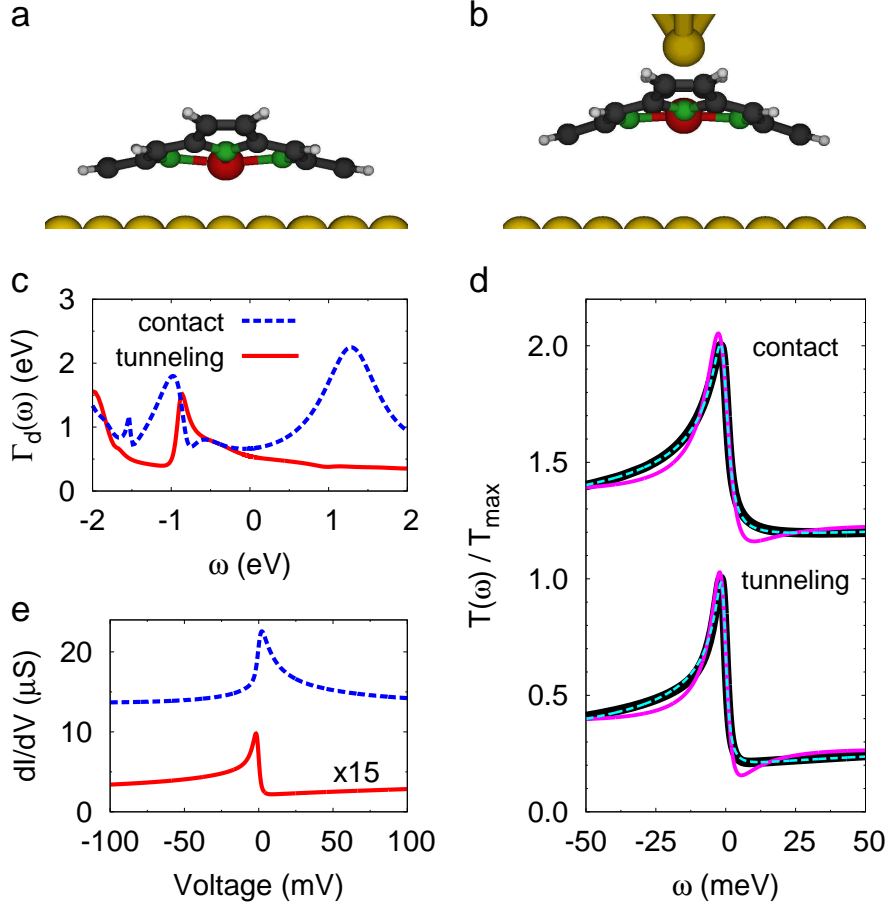
Figure 4.3: (a,b) Schematics of relaxed structures in tunneling and contact regimes. At contact, which corresponds to a tip height of 6 Å above the substrate, the Mn center is lifted from the surface by 0.7 Å w. r. t. the tunneling regime. This vertical displacement is exaggerated in the figure for better perceptibility. (c) Broadening of $3d_{z^2}$ orbital in the tunneling (solid red line) and contact (dashed blue line) regimes. (d) Calculated transmission functions $T(\omega)$ normalized to the maximum transmission $T_{\max}$ in the tunneling and contact (solid black lines) regimes along with fits using Frota (dashed cyan lines) and Fano (solid magenta lines) line shapes. Fits minimize the mean-square deviation over the interval of 100 to 100 meV. For clarity, a narrower range is shown. The transmission curve at contact is shifted by 1. (e) Calculated dI/dV curves in the tunneling (solid red line) and in the contact regime (dashed blue line). α is 0.02 and 0.8 in the tunneling and contact regimes, respectively. The contact spectrum is shifted by 10 μS.

the substrate, respectively. Figure 4.3d shows the calculated transmission curves (for both the tunneling and contact regimes) that exhibit asymmetric resonances similar in shape to those of the dI/dV spectra measured in the tunneling regime (Fig. 4.2b). However, in contrast to the experiment no line shape inversion occurs at contact. Figure 4.3d also shows fits of Fano (solid magenta lines) and Frota (dotted cyan) functions to the calculated transmissions for both tunneling and contact. Interestingly, the fit of the Frota line to our results, which are based on the OCA, is superior. Similar observations were previously made for spectral functions calculated using numerical renormalization group [113, 115] and quantum Monte Carlo [159] approaches. Second order perturbation theory, on the other hand, results in a Fano line shape [160].

The difference in line shape between the calculated transmission functions and the measured dI/dV is understood by considering the voltage drop across the junction. The current through the molecule can be written in terms of the transmission function as $I(V) = \frac{2e}{h} \int_{\mu}^{\mu+eV} d\omega \, T(\omega - \alpha eV)$, where μ is the chemical potential of the substrate and α is a dimensionless parameter determining the local chemical potential at the position of the molecule [143, 161]. Similar to a voltage divider, α can be obtained from the broadening Γ_t (Γ_s) due to tip (substrate) as $\alpha = \frac{\Gamma_t}{\Gamma_t + \Gamma_s}$. Since the transport through MnTPS is dominated by transmission through the $3d_{z^2}$ orbital, for Γ_t and Γ_s we use the couplings of the Mn $3d_{z^2}$ orbital to the tip and substrate, respectively. We estimate $\alpha = 0.02$ with $\Gamma_t \sim 0.01$ eV and $\Gamma_s \sim 0.54$ eV in the tunneling regime, and $\alpha = 0.7$ at contact (tip 6Å above the surface) with $\Gamma_t \sim 0.47$ eV and $\Gamma_s \sim 0.2$ eV. As expected, e. g., from non-equilibrium quantum transport calculations [146], $\Gamma_t \ll \Gamma_s$ in the tunneling range, α is small, the potential at the molecule is pinned to μ, and the applied bias drops over the vacuum gap between the tip and the molecule.

Figure 4.3(e) shows the calculated dI/dV spectra for $\alpha = 0.02$ (tunneling) and $\alpha = 0.8$ (contact). The latter value is chosen because the estimated $\alpha = 0.7$ gives a rather symmetric resonance (also see Supporting Information, Fig. 4.8). Like in the experiments, the line shape of the spectrum at contact (dashed blue line) is inverted with respect to the tunneling regime (solid red line). Since no such inversion occurs in the underlying transmission curves (Fig. 4.3d), the observed inversion is solely due to the modified local potential of the molecule. In other words, the voltage drop has shifted to the molecule–substrate spacing [4]. This shift is not only due to an increased molecule–tip coupling but also to a sub-Angstrom displacement of the molecule, which reduces Γ_s. Moreover, since $\alpha \geq 0.8$ is required to produce an asymmetry comparable to that of the experimental data, we conclude that at least 80% of the voltage drops between molecule and substrate in the contact regime.

A second, less obvious difference between tunneling and contact is that the Kondo screening of the molecular spin is mainly mediated by the electron systems of the substrate and the tip, respectively. In the present experiments, the

---

[4] Ref. [161] pointed out this possibility. However, no corresponding experimental observation was made due to junction instability at high conductances.

tip was covered with Au, the material of the substrate and the Kondo temperature happens to be hardly changed. Occasionally, with some tips, the Kondo resonance disappeared in the contact range, possibly because the material at the apex of those tips did not provide the required screening.

Conclusion

The model of the voltage drop used above has been very useful in interpreting data from double-barrier situations like tunneling to a molecule on a thin insulator. The data presented here for a flat molecule between two metal electrodes, shows that the voltage drop can be very relevant (≥ 80 % between substrate and molecule) in a case that is less expected. While for MnTPS (α close to one) an inversion of the line shape is observed, a more symmetric coupling ($\alpha \approx 0.5$) would cause an artificial broadening of the measured resonance. In summary, the electrical potential in molecular and atomic junctions apparently deserves more attention.
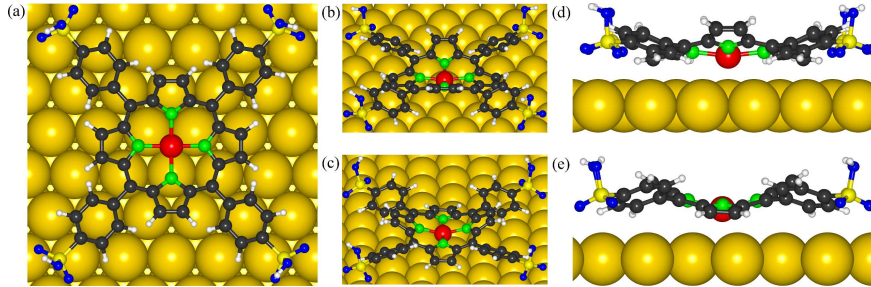
Figure 4.4: Relaxed structures of MnTPS molecule on Au(111) in the tunneling regime. (a) Top view of the molecule adsorbed on the *fcc* hollow site. (b,c) Side view along the two N-Mn-N axes with a 30° inclination w.r.t. the Au surface. (d,e) Side view along the two N-Mn-N axes. For subsequent DFT+many-body calculations the MnP "core" of the molecule has been used.

Supporting Information

I. Structure relaxations

The structures of an MnTPS molecule have been relaxed on a Au(111) substrate using VASP[152, 153], both in the absence and in the presence of a Au tip (in form of a pyramid grown in the [111] direction) in the proximity of the central Mn atom. We have used the Perdew-Burke-Ernzerhof (PBE) functional[154] and included dispersion correction due to Grimme (DFT-D3) [155]. The experimental situation has been modeled using a 3 layer slab of Au(111) extending over 10×10 lateral primitive unit cells. For the relaxations we used the Γ point in the Brillouin zone only. All crystal structures have been relaxed until the forces acting on each atom were smaller than 0.05 eV/Å. The planar geometry of the molecule is strongly deformed on the surface, with the porphine ring forming a saddle structure. The phenyl groups rotate themselves out of the molecular plane by about 30° as shown in Fig. 4.4. Energetically the *fcc* hollow sites are found as the most favorable positions for the molecular center. In the absence of a tip, the distance of the Mn center from the Au surface is 2.77 Å. When the tip is brought into the proximity of the Mn center, the molecule is lifted from the surface. For the apex atom at the heights of 6.0, 5.8, and 5.6 Å above the surface, the Mn center is lifted by about 0.7, 0.5, and 0.3 Å, respectively, from its initial position.

II. DFT+OCA electronic structure and transport calculations

We have performed *ab initio* electronic structure and transport calculations explicitly taking into account the strong dynamic correlations originating from the Mn $3d$-shell that give rise to the Kondo effect, as described in previous

36

work [149–151]. Using the ANT.G *ab initio* transport code[156] we have first performed DFT calculations of an embedded cluster containing the molecule, a finite part of the Au surface and the pyramidal Au-tip. Both the tip and the finite Au surface have been embedded into electrodes modeled by tight-binding Bethe lattices with realistic tight-binding parameters for bulk Au obtained from DFT calculations. In order to make the calculations computationally feasible for the ANT.G code, we replaced the sulfonatophenyl groups of the molecule by hydrogen atoms, leaving the Mn center in a local environment similar to that of the original structure.

From the converged DFT calculation we obtain the Kohn-Sham Green's function of the embedded cluster,

$$\hat{G}_{\mathrm{C}}^0(\omega) = [\omega + \mu - \hat{H}_{\mathrm{C}}^0 - \hat{\Sigma}_{\mathrm{T}}(\omega) - \hat{\Sigma}_{\mathrm{S}}(\omega)]^{-1}, \qquad (4.1)$$

where μ is the chemical potential, $\hat{H}_{\mathrm{C}}^0$ is the Kohn-Sham (KS) Hamiltonian of the cluster which yields a mean-field description of the electronic structure of the cluster and $\hat{\Sigma}_{\mathrm{T}}(\omega)$ and $\hat{\Sigma}_{\mathrm{S}}(\omega)$ are the embedding self-energies which describe the coupling of the cluster to the bulk electrodes of the STM and substrate, respectively. From $\hat{G}_{\mathrm{C}}^0(\omega)$ we calculate the so-called hybridization function of the Mn $3d$-shell,

$$\hat{\Delta}_d(\omega) = \omega + \mu - \hat{h}_{\mathrm{d}}^0 - [\hat{G}_d^0(\omega)]^{-1}, \qquad (4.2)$$

where $\hat{h}_d^0$ and $\hat{G}_d^0(\omega)$ are the projected KS Hamiltonian and KS Green's function, respectively, for the Mn $3d$ states. The negative imaginary part of $\hat{\Delta}_d(\omega)$ yields the (dynamic) single-particle broadening $\hat{\Gamma}_d(\omega)$ of the $3d$-levels due to the coupling to the rest of the system comprising the organic rest of the molecule, substrate and the tip. Figure 4.5 shows the orbitally resolved single-particle broadening $\hat{\Gamma}_d(\omega)$ for the Mn $3d$-shell in the tunneling regime. The hybridization functions resemble the ones calculated for manganese phthalocyanine (MnPc) on Pb(111) and Ag(001) [151, 157], but differ in some important details. The broadening of the $3d_{z^2}$ orbital is relatively featureless around the Fermi level indicating a coupling of that orbital predominantly to the s-type conduction electrons in the Au substrate. Near the Fermi level the d_{xz} and d_{yz} orbitals do not couple directly to the substrate, but the appearance of Lorentzian peaks in the hybridization functions indicate indirect coupling of those orbitals to the substrate via organic ligands. In contrast to MnPc, these peaks are not directly at the Fermi level but about 1 eV above. The $d_{x^2-y^2}$ orbital has an extremely strong coupling to the organic rest of the molecule at -2 eV which leads to quenching of that orbital, while the d_{xy} orbital does not couple at all to the substrate or the organic rest for low energies.

In order to capture dynamic correlation effects originating from the strongly interacting $3d$-electrons of the Mn center, the Mn $3d$-shell is augmented by a Hubbard type interaction term,

$$\mathcal{H}_U = \frac{1}{2} \sum_{ijkl\sigma\sigma'} U_{ijkl} d_{i\sigma}^\dagger d_{j\sigma'}^\dagger d_{l\sigma'} d_{k\sigma}, \qquad (4.3)$$
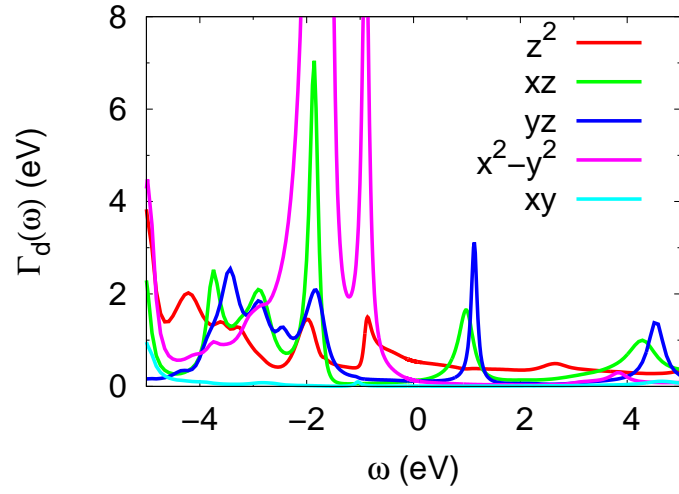
Figure 4.5: Orbital resolved dynamic broadening $\Gamma_d(\omega) = -\mathrm{Im}\Delta_d(\omega)$ for Mn $3d$-shell in the tunneling regime.
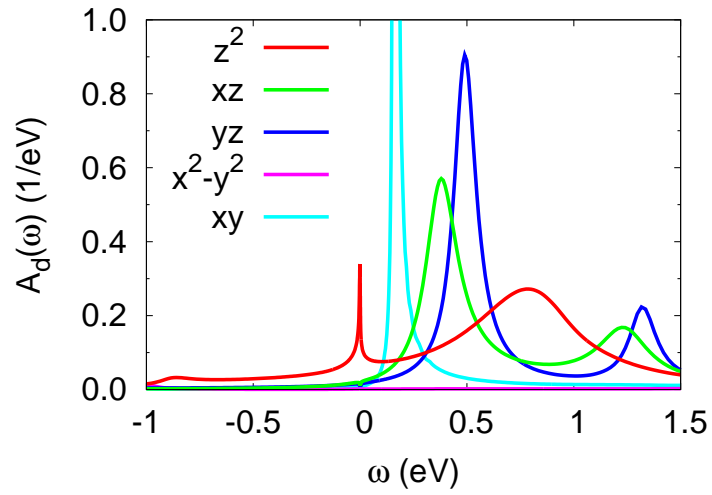

Figure 4.6: Orbital resolved spectral function in the tunneling regime.

where U_{ijkl} are the matrix elements of the effective Coulomb interaction for the Mn $3d$-shell. The effective Coulomb interaction is much smaller than the bare one due to random phase approximation (RPA) screening by the conduction electrons in the substrate, tip and organic rest of the molecule. Here we take a simplified model interaction taking into account only density-density interactions U_{ijij} and Hund's rule coupling U_{ijji}. We assume an intra-orbital repulsion $U = 4.5$ eV, an inter-orbital repulsion $U' = 3.1$ eV and a Hund's coupling $J_H = 0.7 \ eV$. Since the Coulomb interaction within the $3d$-shell has already been taken into account on a mean-field level by the Kohn-Sham DFT Hamiltonian $\hat{H}_d^0$, we subtract a double-counting correction (DCC) in order to obtain the bare energy levels of the Mn $3d$-shell: $\hat{\epsilon}_d = \hat{H}_d^0 - \hat{V}_{dc}$. Here we choose the so-called fully-localized limit (FLL) DCC scheme [162].

The Mn $3d$-levels ϵ_d, the effective Coulomb interaction $\mathcal{H}_U$ and the hybridization function $\hat{\Delta}_d(\omega)$ completely define a multi-orbital Anderson impurity model (AIM). We have used One-Crossing Approximation (OCA) to solve the AIM [158]. The solution of the AIM yields the spectral function of the Mn $3d$-shell $A_d(\omega)$ which is shown in Fig. 4.6 for the tunneling regime. Only the $3d_{z^2}$ orbital shows a Kondo peak at the Fermi level. The other orbitals do not show Kondo peaks but have strong resonances not too far from the Fermi level. Overall the Mn $3d$-shell is in a mixed valence situation with a total occupation of ~ 5.5, although individual orbital-occupancies are rather close to 1. The total spin of the Mn $3d$-shell is found to be approximately 1.7, $i.e.$ half-way between a Spin-3/2 and a Spin-2 systems. The spin in the $d_{x^2-y^2}$ orbital is completely quenched by the strong coupling to the organic ligands. At contact the d_{z^2} orbital is slightly lowered in energy due to the bonding to the tip atom, increasing the occupancy of that orbital to ~ 1.2.

Using the Kramers-Kronig relation the real part of the correlated $3d$ Green's function $\hat{G}_d(\omega)$ has been calculated. From that we obtain the electronic self-energy via $\hat{\Sigma}_d = [\hat{G}_d^0]^{-1} - [\hat{G}_d]^{-1}$, which captures the dynamic correlation effects induced by the effective Coulomb interaction $\mathcal{H}_U$. The $correlated$ electronic structure and transport properties of the whole system is then calculated from the correlated cluster Green's function,

$$\hat{G}_{\mathrm{C}}(\omega) = [(\hat{G}_{\mathrm{C}}^0(\omega))^{-1} - \hat{\Sigma}_d(\omega) + \hat{V}_{dc}]^{-1}, \qquad (4.4)$$

where the $\hat{\Sigma}_d$ and $\hat{V}_{dc}$ only act on the subspace of the Mn $3d$-shell. From $\hat{G}_{\mathrm{C}}(\omega)$ we calculate the correlated transmission function,

$$T(\omega) = \mathrm{Tr}[\hat{\Gamma}_{\mathrm{T}}(\omega)\hat{G}_{\mathrm{C}}^\dagger(\omega)\hat{\Gamma}_{\mathrm{S}}(\omega)\hat{G}_{\mathrm{C}}(\omega)], \qquad (4.5)$$

which according to Landauer yields the low-bias transport properties, $i.e.$ the low-bias differential conductance and current [84]. $\hat{\Gamma}_{\mathrm{T}}$ and $\hat{\Gamma}_{\mathrm{S}}$ are the imaginary parts of the electrode self-energies $\hat{\Sigma}_{\mathrm{T}}$ and $\hat{\Sigma}_{\mathrm{S}}$, respectively. Figure 4.7 shows the calculated transmission functions both in the tunneling and in the contact regime for different heights of the tip above the surface. For distances below 5.8 Å the transmission function is strongly broadened, $i.e.$ the Kondo
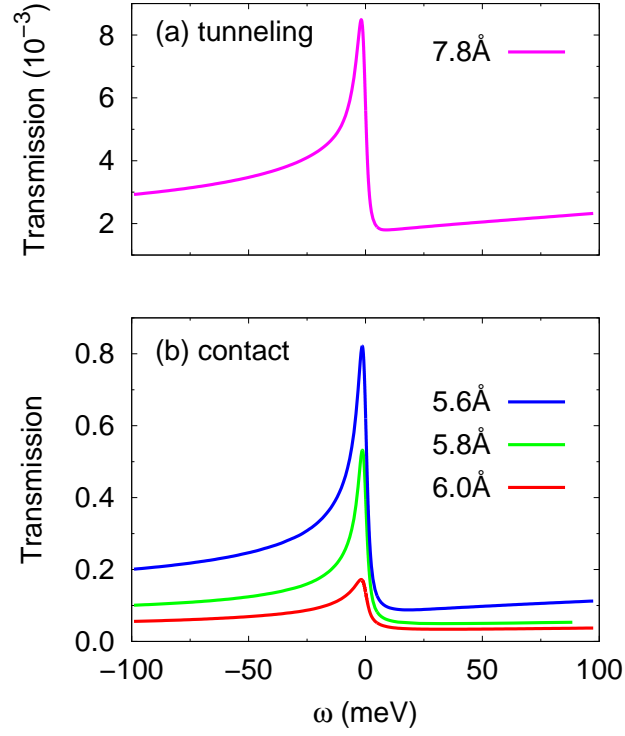
Figure 4.7: Correlated transmission functions (a) in the tunneling regime with the tip at 7.8Å above the surface, and (b) in the contact regime with tips at different heights above the surface as indicated.
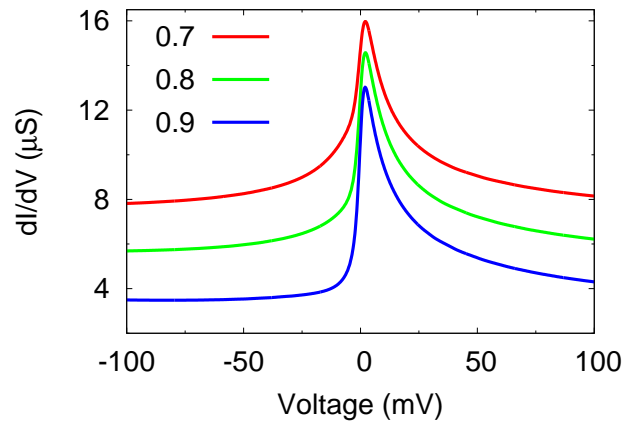
Figure 4.8: Calculated dI/dV spectra in the contact regime with the tip at 6Å above the substrate for different values of the parameter α.

temperature increases strongly. Also the conductance increases strongly. However, junction instability at higher current prohibited to make this observation experimentally.

Figure 4.8 shows the calculated dI/dV spectra in the contact regime for different values of α, the dimensionless parameter determining the local chemical potential at the position of the molecule. For $\Gamma_t \ll \Gamma_s$ ($\Gamma_t \gg \Gamma_s$), $\alpha \to 0$ ($\alpha \to 1$) implying that the local potential at the molecule is pinned to the chemical potential of the substrate (the tip).

Acknowledgement

5 Remotely Triggered Geometrical Isomerization of a Binuclear Complex

The results presented in this chapter were published in the Journal of American Chemical Society [17].

Abstract

Binuclear organometallic molecules are model systems for investigating intramolecular spin-coupling and charge-transfer processes. Using electrospray ionization, Fe(salten) dimers linked by dipyridyl disulfide are deposited on gold for probing with a low-temperature scanning tunneling microscope. Each monomer constitutes a multistable switch owing to its geometric isomerism. Controlled and reversible remote switching within a single dimer is demonstrated. The process is attributed to intramolecular electron transfer.

Introduction

One approach to molecule-based functional devices relies on switches on surfaces. Switching in molecular layers has been achieved using stimuli like light, temperature, and electric fields [22, 27, 163–168]. Upon injecting current with a scanning tunneling microscope (STM), changes of molecular conformation, spin, and adsorption state have been observed [23, 45, 46, 169–172].

Usually the current-induced changes occur directly under the STM tip [173]. For molecule-based logic, however, a lateral energy transfer appears to be necessary. Few examples—controlled molecular hopping [174] and tautomerization propagating over an intervening molecule [30]—have been reported from custom-made molecular arrays. Implementing a pathway for energy transfer within a single molecule by chemical synthesis is a desirable alternative to on-surface preparation with a STM.

Here we demonstrate controlled and reversible remote switching within a single binuclear organometallic molecule. By injecting current to one subunit, a reversible isomerization of the other via a Bailar twist [61] is induced. The choice of the linker between the subunits is seen to be crucial for electron transfer comparing results from electron-rich disulfides and less conducting ethyl chains.

43
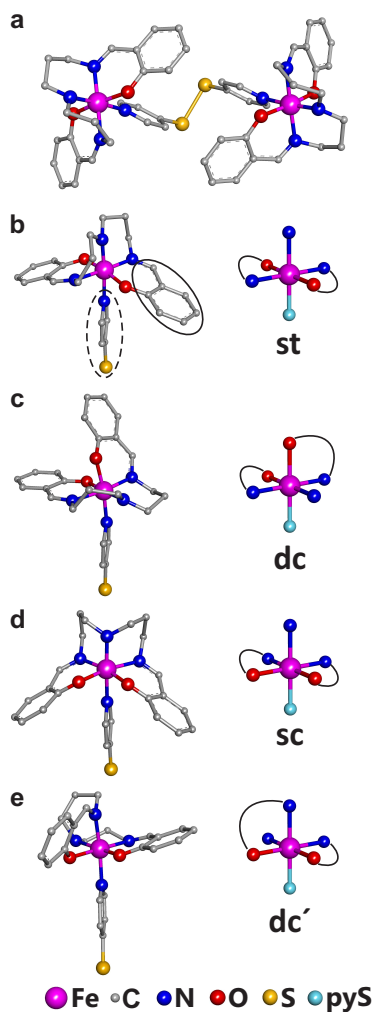
Figure 5.1: Structures of [Fe(salten)pyS]$_2$ dimer and monomers. H atoms are not shown. (a) Calculated structure of [Fe(salten)pyS]$_2$. (b–e) Geometrical isomers of the (thiopyridine)-Fe(salten) subunit: (b) symmetric *trans* (st), (c) dissymmetric *cis* (dc), (d) symmetric *cis* (sc), and (e) second dissymmetric *cis* (dc'). Solid and dotted ellipses indicate phenolate and the coligand L = pyridine thiolate, respectively. The molecular structures in the left panel are represented by simplified symbols of the quasi-octahedral cores on the right. Arches indicate the positions of phenolate rings.

Results and Discussion

As a switch we synthesized the binuclear compound [Fe(salten)pyS]$_2$ (Fig. 5.1a) [175]. It is composed of two iron(III) bis(3-salicylideneaminopropyl)amine (Fe-salten) subunits that are coupled via a dipyridyl disulfide (pySSpy) linker. To enable single-molecule experiments in ultrahigh vacuum and at low-temperature (~ 5 K) we used electrospray ionization for deposition of molecules onto Au(111) [99].

The geometry of pseudo-octahedral [Fe(salten)L] complexes depends on the coligand L. Strong or bulky ligands, *e.g.*, pyridine or pyridine derivatives, lead to a *trans* geometry (Fig. 5.1b) [176]. Weaker ligands favor a *cis* configuration (Fig. 5.1c) [177]. While the *cis* configuration is dissymmetric, the *trans* configuration exhibits a C_2 axis. Besides these geometries, which have been observed in crystals before [176, 177], two additional configurations are conceivable, namely a symmetric *cis* configuration with a mirror plane (Fig. 5.1d), and a second dissymmetric configuration with both phenolate groups *cis* to the axial ligand (Fig. 5.1e). Below we use the naming scheme st, dc, sc and dc' introduced in Fig. 5.1. The dimer of Fig. 5.1a with two st subunits is accordingly denoted st–st. Our calculations (see Computational Methods in the Supporting Information for details) show that with L = pyridine thiolate the st and dc isomers are most stable (Supporting Table 5.1). The energies of dc', and sc are higher by ~ 0.5 and 0.9 eV, respectively, in agreement with the fact that dc and st are experimentally observed [176] whereas dc' and sc are hypothetical.

After deposition of sub-monolayer amounts of [Fe(salten)pyS]$_2$ onto Au(111), STM images reveal three closely related dimeric patterns (Fig. 5.2). They may be divided in halves (dotted line in Fig. 5.2a) that exhibit either three (Fig. 5.2a) or three major and one minor (Fig. 5.2b) lobes. Two patterns are composed of identical halves (Fig. 5.2a,b), and the third one (Fig. 5.2c) is a combination thereof. The submolecular contrasts may be understood on the basis of the structures of dimers (Fig. 5.2d–f) comprising combinations of the isomers shown in Fig. 5.1. The molecules are assumed to adsorb with the disulfide linker attached to the substrate. The molecule of Fig. 5.2a is a symmetric dc–dc dimer. Its highest lobes appear to originate from the phenolate ligand. The pattern of Fig. 5.2b is consistent with a st–st dimer (Fig. 5.2e) where the phenolate ligands are located at heights similar to that Fe, with a propyl chain (C3 linkage) above one of them. The propyl chain is likely causing the extra lobe in the image. Finally, the asymmetric species of Fig. 5.2c combines the dc and st subunits and is denoted dc–st. The abundances of st–st, dc–st, and dc–dc dimers determined from large scale images ($\sim 40\%$, 35%, and 25%, respectively) are consistent with the calculated sequence of energies (Table 5.1). A dc configuration of a subunit of the adsorbed [Fe(salten)pyS]$_2$ seems to be at conflict with the st configuration reported for bulk materials. However, infrared reflection absorption spectra indicate that on Au(111) a dc configuration is also possible [175], which is consistent with our STM observations.

Spectra of the differential conductance dI/dV of the three species (Fig. 5.2g–i) were acquired at the positions marked in the STM images. With the tip above
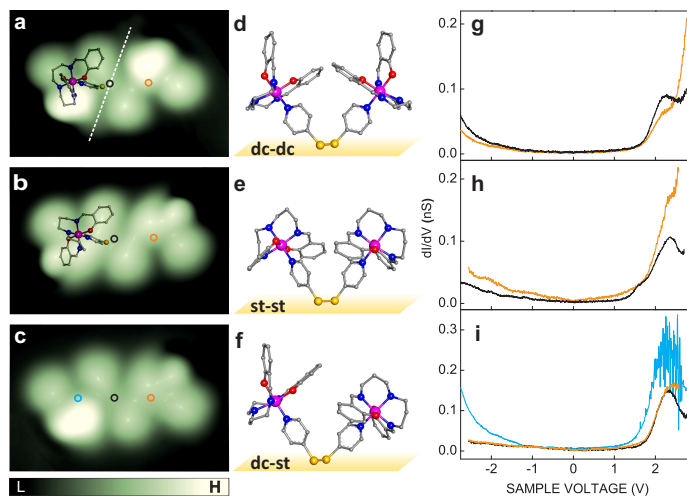
Figure 5.2: (a–c) STM images $(3.5 \times 2.4 \text{ nm}^2)$ of three distinct structures of [Fe(salten)pyS]$_2$ on Au(111). The data is displayed in a pseudo-three-dimensional fashion with the color scale covering a range of 0.21 nm. Images (in all the figures) were acquired with sample voltages $V = 0.20 - 0.25$ V at constant currents $I = 10 - 50$ pA. A dotted line in (a) separates the two subunits of the binuclear molecule. Colored circles indicate the positions where dI/dV spectroscopy was performed. In (a) and (b), topviews of models of dc and st monomers are overlaid over one half. (d–f) Side views of [Fe(salten)pyS]$_2$ comprising different isomers. (g–i) dI/dV spectra recorded at the positions indicated in a–c. Before opening the current feedback, the STM was operated at $V = 2.7$ V and $I = 100$ pA.

the disulfide moiety, all species show a prominent unoccupied electronic state at ~ 2.35 V (black lines). Indication of this resonance is also discernible closer to the centers of the individual subunits (orange lines). The similarity of the spectra of all species lends support to the geometric interpretation of the STM images in Fig. 5.2a–c.

dc–st molecules display a striking anomaly when the tip is placed over the center of the dc subunit (blue circle and line in Figs. 5.2c,i). Fluctuations occur at sample voltages exceeding ~ 1.5 V, which signal rapid changes of the tunneling junction. Figure 5.3b presents the result of current injection to the dc subunit of the dc–st dimer shown in Fig. 5.3a. The st subunit has switched to a new state with a bright protrusion at its center. We attribute it to the dc' isomer of Fig. 5.1e, where the phenolate ligand with its conjugated π system is located above the Fe center Fig. 5.3f.

The manipulated monomer is located ~ 1 nm away from the point of current injection; *i.e.*, the switching occurs remotely. The process is fully reversible. By injecting another current pulse on the dc side, the original dc–st state is restored. Remarkably, the dc unit itself does not switch to any other configuration so long as nondestructive currents and voltages are used.

On st–st dimers (Fig. 5.3c) a transformation to st–dc' was occasionally found (Fig. 5.3d). However, the switching took place locally, *i.e.* at the st subunit to which the current was injected. st–dc dimers behaved similarly (reversible, local switching to dc'–dc).

We suggest that the isomerization between st and dc' is effected by a Bailar twist [61], whereby two opposite triangular faces of the octahedral coordination shell rotate by 120° with respect to each other. Fig. 5.4 shows the transformation of a dc' isomer to st via a twist of the upper triangle, while the lower one is fixed to the substrate. It involves only one flexible C3 linkage, while all other metal-ligand bonds remain fixed. It may be reversed, but the ligands do not allow for further rotation. Consequently, the st subunit represents a two-state configurational switch. The absence of any switching from dc subunits can also be understood on the basis of this mechanism (see Supporting Fig. 5.5). A twist from dc to dc' would involve a propylene and an iminophenol bridge. The conjugated π system of the latter is more rigid and thus suppresses this twist. Another conceivable twist involving only a flexible C3 linkage leads to the unfavorable (*vide supra*) sc configuration. This explains why remote switching is found only when injecting electrons into the dc part of dc–st dimers (or the resulting dc–dc' dimers) and not on st–st dimers. dc cannot be switched and thus serves as a relay to transfer the excitation energy to the other subunit, while st uses the energy itself to convert to dc'.

The mechanism of the remote switching is of particular interest. Remote switching on dc–st and only local switching on st–st are difficult to reconcile with a force-related mechanism. Moreover, the threshold voltage of ~ 1.5 V, which is close to the onset of the unoccupied molecular resonance, and the absence of switching at reversed polarity favor an electron-induced process.

The different total energies of the dimers (Supporting Table 5.1) are essentially due to the different energies of their subunits rather than their mutual
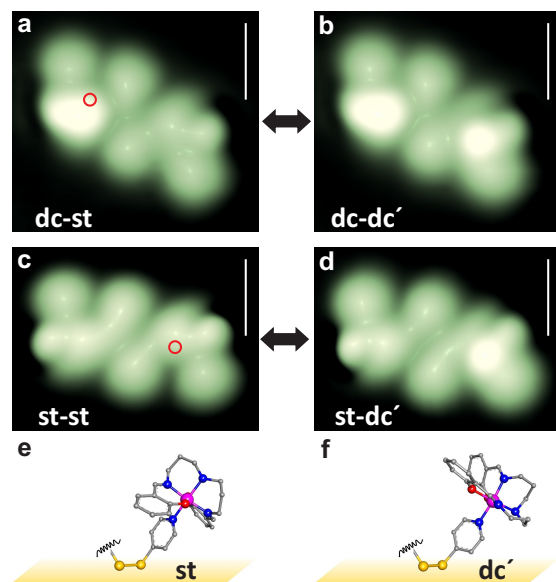
Figure 5.3: Reversible isomerization of dc–st and st–st molecules. STM images recorded (a,c) before and (b,d) after injecting current at 1.6 V at the positions marked by red circles in a and c. Scale bars correspond to 1 nm. (e,f) Side views of st and dc' subunits, respectively.
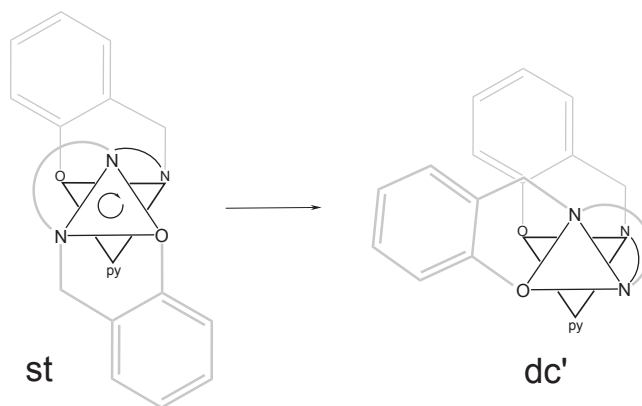
Figure 5.4: Isomerization of st to dc' via a Bailar twist. Two opposite triangular faces of the octahedral coordination shell of [Fe(salten)pyS] are displayed with black lines. C3 linkages are indicated by arches, and C–N double bonds are omitted. In the Bailar twist transforming the st isomer to dc', the upper triangle rotates clockwise by 120° with respect to the lower one, which is fixed to the substrate by the pyridine disulfide linker. Further rotation is sterically inhibited.

interaction. This means that a sufficient fraction of the excitation energy has to be transferred from the dc to the st subunit to achieve isomerization to dc'.

The injection of an electron to the dc subunit locally creates an electronically and possibly vibrationally excited state. To discriminate between vibrational and electronic energy-transfer mechanisms, a dimer linked by a less electron-rich dipyridylethane moiety was synthesized. Using deposition conditions similar to those used before, ∼ 60% st–st and ∼ 40% dc–st dimers were observed (see Supporting Fig. 5.6a) which appear very similar to the disulfide-linked molecules. Switching experiments on dipyridylethane-linked dimers, however, led to strikingly different results. On the dc–st species, remote switching was never observed. Occasionally, we found local interconversion between st and dc' when tunneling directly into these subunits (Supporting Fig. 5.6b,c).

The results from the dipyridylethane-linked dimers allow for the following conclusions. First, through-space tunneling from the excited dc subunit to the st part is not relevant for switching. The absence of remote switching of sulfide-linked st–st molecules is also in line with this interpretation. Next, vibrational energy transfer may tentatively be excluded. The energies of the S–S stretching and bending modes are lower than the energies of the modes of the Fe(salten) monomers. This, along with the bonding of the S atoms to Au, is expected to make vibrational energy transfer over the S–S linker rather inefficient. The fact that the dipyridylethane bridge does not enable remote switching despite its different vibrational modes does not favor vibrational energy transfer. This leaves electron transfer through the disulfide bridge, possibly involving the S–Au bonds, as the most likely scenario. Our calculations for sulfide-linked dimers indeed show that the lowest unoccupied molecular orbital exhibits a high electron density at the disulfide bridge and overlaps with the Fe(salten) subunits (see Supporting Fig. 5.7). With an dipyridylethane bridge, this orbital is localized to the separate subunits and hardly overlaps via the ethyl chain (see Supporting Fig. 5.7).

Conclusion

In conclusion, a custom-made binuclear Fe(salten) complex on Au exhibits geometrical isomerism of the individual subunits. Reversible switching between two isomers has been achieved within single molecules. A disulfide bridge connecting the molecular subunits enables remote switching, whereas an ethyl link is inactive. It is conceivable that our approach may be extended to implement basic logic functions within a single molecule.

Supporting Information

I. Experimental details

The experiments were carried out with a low-temperature scanning tunneling microscope (STM) in ultrahigh vacuum (UHV). Single crystalline Au(111) substrates were cleaned by Ar^+ sputtering and annealing at $\sim$ 750 K. Using an electrospray ionization apparatus, freshly synthesized binuclear [Fe(salten)pyS]$_2$ was sprayed in positive ion mode from a methanolic solution, mass selected, and deposited onto the substrates held at room temperature in UHV. Subsequently the samples were initially cooled to nitrogen temperature and then transferred into the microscope at $\approx$ 5 K. All STM images shown were acquired at constant currents $I = 10 - 50$ pA and sample voltages $V = 0.20 - 0.25$ V. The image contrasts were essentially unchanged within the range -1 V $< V < 1.1$ V. Currents exceeding $\sim$ 200 pA usually lead to irreversible damage of the molecules. STM images were processed with WSxM [178].

II. Computational methods

Density functional theory (DFT) calculations were carried out with the software package Gaussian-09 [179] using Beckes three-parameter hybrid functional with the LYP 196 correlation functional of Lee, Yang, and Parr [180]. A 6-311G basis set was used for all atoms.

III. Calculated total energy differences for [Fe(salten)pyS] and [Fe(salten)pyS]$_2$

Monomers	$\Delta E(eV)$	Dimers	$\Delta E(eV)$
dc	0	st–st	0
st	0.08	dc–st	0.15
dc'	0.58	dc–dc	0.37
sc	0.98	st–dc'	0.51
		dc–dc'	0.75
		dc–sc	1.06
		sc–sc	1.72

Table 5.1: Calculated total energy differences with respect to the lowest energy monomer and dimer. Note that the energy difference between st and dc monomers is insignificant compared to the estimated accuracy of the calculations.

IV. Bailar twists not observed in the experiments
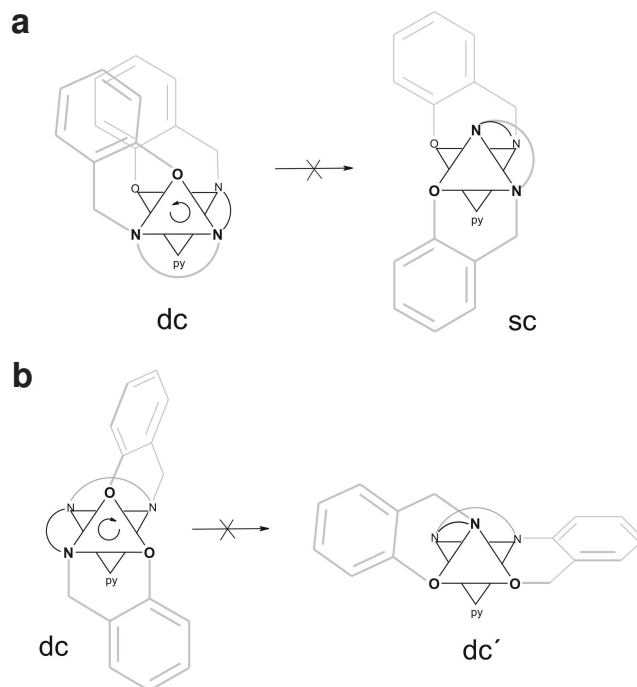
Figure 5.5: Bailar twists starting from the dc configuration. (a) Twist from dc to sc. Only one flexible C3 linkage is connecting the triangles. However, the final sc configuration is energetically unfavorable. (b) Twist from dc to dc'. The triangular ligand planes are connected by propylene and iminophenol, the latter being rigid owing to its conjugated π electron system.

V. STM data from dipyridylethane-linked dimers on Au(111)
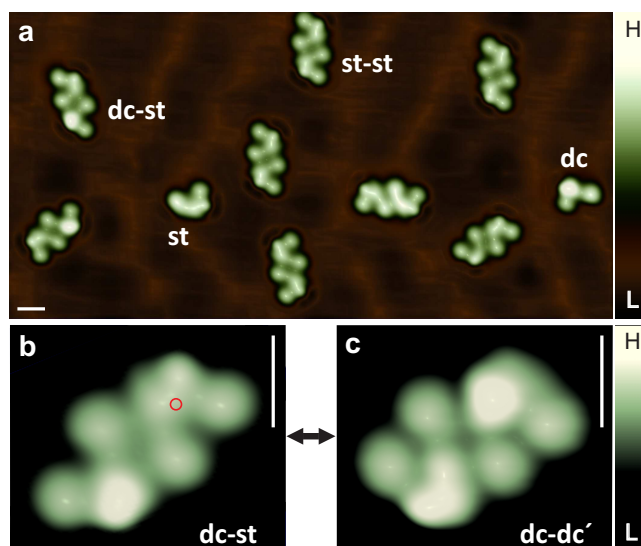
Figure 5.6: STM images of dipyridylethane-linked dimers on Au(111). Scale bars correspond to 1 nm in all panels, the height scale covers a range of 0.22 nm. (a) The 22×11 nm^2 image shows [(salten)pyCH$_2$]$_2$ deposited on Au(111). The majority of molecular features are st–st and dc–st dimers (two examples are labeled). Few dc and st monomers are observed. Small variations of the apparent molecular heights are presumably due to different adsorption sites on the reconstructed substrate. (b) Electron injection into the st subunit at the indicated position (red circle) induces a transition to dc' as shown in (c). By repeating the injection to the st subunit the original state can be restored. In contrast to the disulfide-linked complex, remote switching was never observed.

VI. Calculated orbital energies of [Fe(salten)pyS]$_2$ and [Fe(salten)pyCH$_2$]$_2$
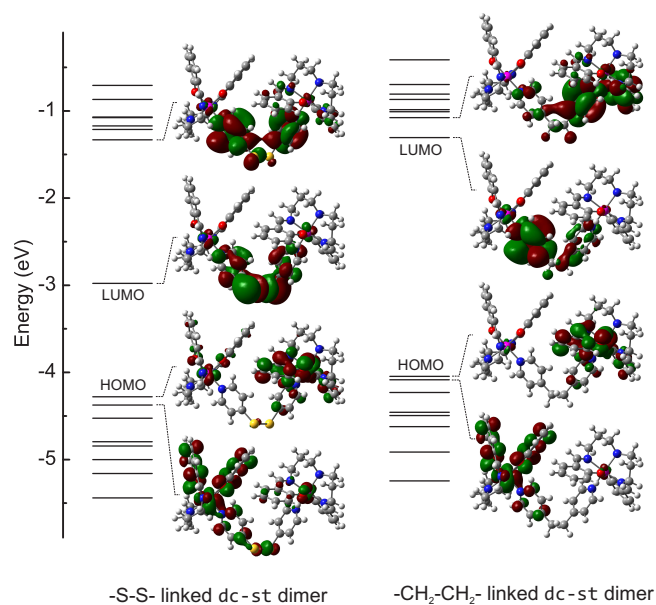
Figure 5.7: Calculated energy levels and isodensity plots of frontier orbitals. Results for [Fe(salten)pyS]$_2$ and [Fe(salten)pyCH$_2$]$_2$ are shown in the left and right columns, respectively. The lowest unoccupied molecular orbital (LUMO) of [Fe(salten)pyS]$_2$ exhibits a high density at the disulfide bridge and overlaps with the Fe(salten) subunits. In contrast, in the dipyridylethane-linked molecules this orbital is localized at the Fe(salten) subunits with hardly any overlap via the link. Moreover, the HOMO–LUMO gap is substantially wider.

VII. Oxidation state of Fe centers

The oxidation state of the Fe centers in the synthesized bulk material was III [175]. However, there are reasons to assume an Fe(II) state on the Au(111) surface. The electron rich gold surface may be expected to reduce deposited compounds [181]. More importantly, our experimental dI/dV spectra with a wide gap are consistent with a closed-shell Fe(II) molecule and do not match the calculated Fe(III) states. Finally, the DFT calculations predict widely different dihedral angles of the disulfide part. For example, $\approx 85°$ and $\approx 139°$ are obtained for the low-spin Fe(II) and Fe(III) states of the dc–sc dimer (Fig. 5.8). The same trend is observed for the other dimers. The match between the rather flat Fe(III) dimers with the observed STM images is less favorable. Finally, injection of electrons into the antibonding LUMO of the Fe(II) complex weakens the ligand bonds and thus enables a Bailar twist. In contrast, the LUMO of the Fe(III) complex is not involved in the ligand bonds and therefore inactive.
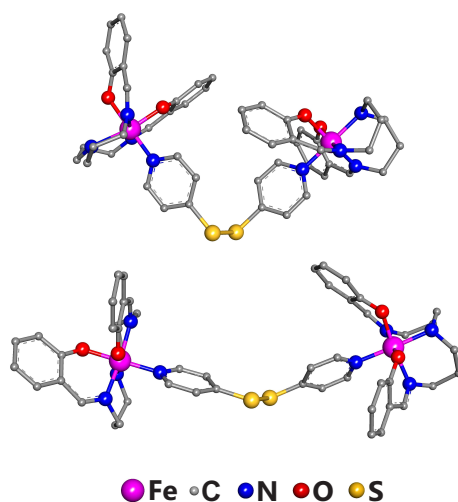
Figure 5.8: Calculated structures of dc–sc dimers with Fe(II) (top) and Fe(III) (bottom).

Acknowledgement

54

6

Surface Trapping and STM Observation of Conformational Isomers of a Bis(Terpyridine) Ligand from Metallosupramolecular Grids

This chapter is based on a publication in ChemPhysChem [182].

Abstract

Tetranuclear Co-grid complexes incorporating bis-tridentate ligands, namely 4,6-bis(2,2′-bipyrid-6-yl)-2-phenylpyrimidine, were electrosprayed onto a Au(111) substrate in ultra-high vacuum. Fragmentation occurs leaving the ligands in four different conformations. The most abundant conformer of the ligand on the Au surface is an asymmetric form, which has not been observed before. The results indicate that the fragmentation of coordination compounds during the deposition process allows for the surface trapping, identification and investigation of high energy, out-of-equilibrium conformations of the ligand molecules at low temperatures, which otherwise would not be observable.

Introduction

Finding ways for generating, stabilizing and scrutinizing fleeting and unstable molecular states, such as conformational isomers, is of much interest for the understanding of molecular structure and behaviour. We encountered an approach to these ends in the course of a scanning tunneling microscopy (STM) study of metallosupramolecular $[2 \times 2]$ grid-type architectures consisting in two-dimensional meshes of transition metal ions that are stabilized by organic ligands [183]. These complexes exhibit a number of intriguing structural and magnetic properties [184–189]. For example, antiferromagnetic coupling of Co^{2+} centers was found in the $[2 \times 2]Co(II)_4$ compound, suggesting that this complex may represent a rather ideal quantum spin system [190]. Moreover, switching of its conductance in molecular junctions has been reported [191]. STM images of this complex under ambient conditions on graphite were encouraging although an unambiguous identification of the molecules was not obtained [185, 187].

To be able to apply high-resolution electron spectroscopes such as STM at low-temperature to grid complexes, deposition and measurement under ultrahigh vacuum conditions are desirable. For this reason, we used an electrospray source to deposit the grid-type complex composed of four Co(II) ions connected via four bis-tridentate ligands, namely 4,6-bis(2,2′-bipyrid-6-yl)-2-phenylpyrimidine (**b-tpy**, Fig. 6.1a), on Au(111) single crystal surfaces. An uncoordinated ligand adopts a conformation with all NC–CN rotamers in N,N *transoid* form (Fig. 6.1a) both in organic solvents and solid state [192–195]. In contrast, metal ion binding enforces a *cisoid* orientation of all NC–CN rotamers of the ligand (Fig. 6.1b) so that it exhibits two terpyridine-like coordination subunits. Thus, in the grid-type structure, all four ligands are in fully *cisoid* orientation. We found that the grid complex fragmented even at the lowest ion energies achieved leading to the deposition of uncoordinated **b-tpy** ligands. Interestingly, a number of structural isomers of the deposited ligand were observed. Indeed, the ligand displayed four distinct conformations with one of them being asymmetric. Remarkably, the conformer that is most frequently observed on Au(111) is thermodynamically neither favored in gas phase nor on the surface. Its abundance is apparently caused by the kinetics of the deposition on the cold Au substrate. The asymmetric conformers, which become chiral upon adsorption, bind among themselves as well as with other conformers in a variety of supramolecular dimer configurations. Density functional theory (DFT) calculations are used for further characterization.

Results and Discussion

Au(111) single crystal surfaces were cleaned in ultrahigh vacuum (UHV) by repeated Ne$^+$ sputtering and annealing. A 0.05 mM solution of Co-grid in acetonitrile was electrosprayed [99] onto these substrates at ambient temperature in UHV. The electrospray set-up was operated in positive ion mode at a voltage of 3.5 kV for generating gas-phase ions. The cation beam was analyzed by a quadrupole mass spectrometer prior to the deposition onto the substrate. Typical mass spectra (Fig. 6.1c) showed an intense peak at ~ 526 Th with a width of ± 5 Th along with a smaller maximum at ~ 467 (± 6) Th. The mass-to-charge ratio of ~ 467 Th matches a protonated **b-tpy** ligand. The intense peak is attributed to $[Co_4(\textbf{b-tpy})_4 + 6\ BF_4 + 3\ H]^{+5}$. [1] To achieve a useful average ion current of ~ 8 pA at the sample at a low impact energy of 6.5 eV per charge, we selected a mass range of 525 ± 10 Th which encompasses the most intense peak. After deposition samples were cooled to 80 K and transferred to a STM without

---

[1] The molecule itself contains eight BF$_4$ anions in crystalline form [202]. The mass-to-charge rato $m/e = 523.4$ Th of $[Co_4(\textbf{b-tpy})_4 + 6\ BF_4 + 3\ H]^{+5}$ is consistent with the most intense peak. This peak could also be due to $[Co_2(\textbf{b-tpy})_3 + BF_4]^{+3}$. This would imply that one of the three **b-tpy** ligands is in *cisoid* form. The lowest energy conformation of each of the other two ligands involves one *trans* and one *cis* form of the R_{pm} rotamers encompassing the empty and Co-coordinated terpyridine-like sites, repectively. No other compounds with acceptable numbers of Co, BF$_4$ and ligands fall into the width of the most intense peak, that was selected for deposition.
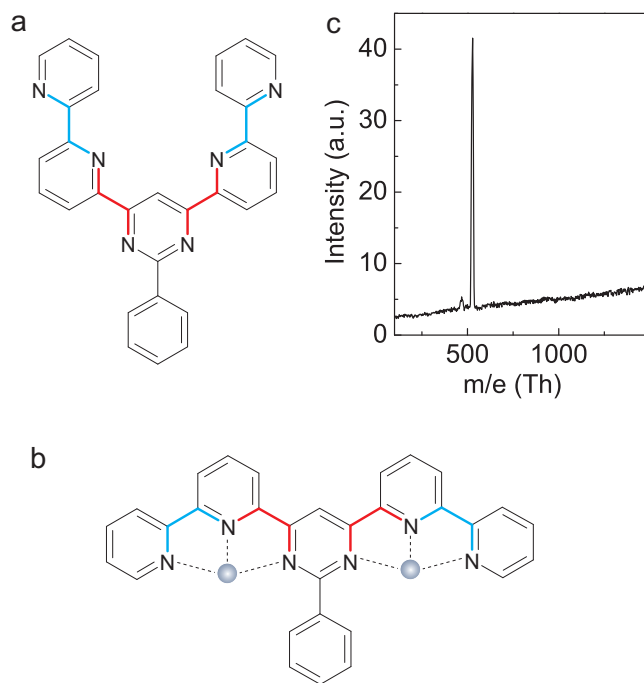
Figure 6.1: (a) Conformation of a **b-tpy** ligand with all
NC–CN rotamers in *trans* form. NC–CN rotamers contain-
ing N atoms of the pyrimidine unit are highlighted in red
(denoted R_{pm} below), cyan represents the rotamers associ-
ated to bipyridine units. (b) A ligand in *cisoid* conforma-
tion having two terpyridine-like binding sites occupied with
metal atoms through chelating coordination bonds (dotted
lines). (c) Mass spectrum of the electrosprayed ion beam.

breaking the vacuum. For imaging and spectroscopy the STM was cooled down to ~ 5 K. Electrochemically etched W wire was used as STM tips, which were further treated *in situ* by indenting into the Au substrate. Spectra of the differential conductance (dI/dV) were recorded using a lockin amplifier by adding a sinusoidal modulation of 10 mV$_{rms}$ at 1.2 kHz to the sample voltage V. The STM was operated at $V = -3$ V and at current $I = 200$ pA before opening the feedback for spectroscopy.

After the deposition we did not find any intact grids on Au(111). Rather, four distinct forms of **b-tpy** were observed (Figs. 6.2a–d), which reflect the fragmentation of the grids. All four conformers exhibit a similar average apparent height of ~ 0.16 nm, which suggests a planar adsorption geometry of all species with the heterocyclic units lying flat on the surface. The low apparent height of the observed species is also inconsistent with the height expected from intact grids. Optimized models (details in the Supporting Information, Section II) of different two-dimensional diastereomeric combinations of NC–CN rotamers involving N atoms of the pyrimidine unit (highlighted in red in Fig. 6.1, denoted R_{pm} rotamers below) are shown in Figs. 6.2e–h alongside the STM images.

The *trans* form of both R_{pm} rotamers (Fig. 6.2e) results in the conformer of Fig. 6.2a (denoted **T** below). Such a conformation of a **b-tpy** ligand is unsuited to metal coordination due to the absence of terpyridine-like binding sites (as shown in Fig. 6.1b). To retain a metal ion within the coordination geometry of the ligand, at least one of the R_{pm} rotamers should be in *cis* form [196]. Figure 6.2b shows a pattern (denoted **T**′ below) similar to **T** conformer. However, its two adjacent lobes appear closer to each other than in **T**. We propose the model in Fig. 6.2f where both bipyridine moieties of the ligand are in *cis* form. A non-planar geometry is calculated for this conformation of the ligand on gold, contrary to the other conformers with bipyridine moieties in *trans* form. Our calculations further indicate NC–CN dihedral angles of the two bipyridine units of approximately 44° and −23°. The former value is very similar to the dihedral angle reported for *cis*-bipyridine in gas phase [197]. The downward twist of the pyridine units may be the reason for the modified image contrast. The conformer shown in Fig. 6.2c (denoted **C** below) resembles the structural model of Fig. 6.2g with both R_{pm} rotamers in *cis* form, whereas the combination of *cis* and *trans* (Fig. 6.2h) produces the assymmetric pattern of Fig. 6.2d (denoted **TC** below). Although **C** and **TC** conformers have at least one of their R_{pm} rotamers in *cis* form, we presume that both these conformers appear on the surface without any coordination with cobalt for the following reasons. First, if the Co atoms were present one would expect to find a clear protrusion in the STM images as previously observed from Co adatoms on a Au(111) substrate [198]. Our simulated images of cobalt-coordinated geometries (see the Supporting Information, Fig.6.6) show pronounced protrusions at Co atoms and thus confirm this expectation. Second, Co on Au(111) usually displays a zerobias anomaly in the differential conductance (dI/dV) spectrum as a signature of Kondo-screening [105, 198]. In contrast, dI/dV spectra recorded over a variety of positions of the species (see Fig. 6.3 for two examples) do not show any characteristic feature close to zero bias.
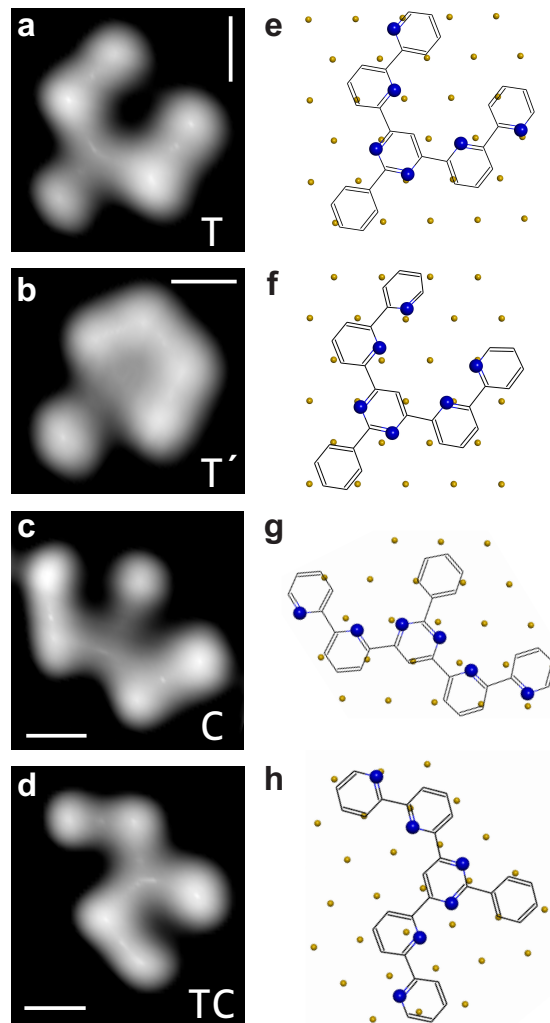
Figure 6.2: (a–d) STM images of four distinct conformers of **b-tpy** ligand on Au(111). Images are displayed in a pseudo-three-dimensional fashion with the gray scale covering a range of 0.2 nm. All images were acquired at a sample voltage $V = -0.35$ V and at constant currents $I = 10 - 30$ pA. Scale bars correspond to 0.5 nm. (e–h) Optimized structural models (top views) of the ligand on Au(111) in different isomeric forms. Yellow dots depict Au atoms at the top layer of the slab used for calculations. Blue represents N atoms.

dI/dV spectra recorded over the pyrimidine unit of the ligand (black curve in Fig. 6.3a) show an intense resonance at ≈ 2.3 V which we attribute to the lowest unoccupied molecular orbital (LUMO) of the ligand. As the tip is moved laterally, the peak intensity diminishes (red curve, Fig. 6.3a), suggesting that the LUMO is located on the pyrimidine unit of the ligand, in agreement with interpretations of previous electrochemical and UV absorption measurements [193]. We also calculated the projected density of states (PDOS) for different conformers of the ligand. Similar features (blue curve in Fig. 6.3b shows an example for **C** conformer) were obtained for all the conformers shown in Figs. 6.2e–h, as one would expect for geometrical isomers. They exhibit HOMO–LUMO gaps of approximately 2 eV, whereas the calculations predict vanishing gaps for cobalt-coordinated complexes (cyan curve in Fig. 6.3b). This further confirms that the Co centers have been lost.[2]

Large scale images show that **TC** and **T** conformers are most abundant (~ 75 and ~ 10 %, respectively) whereas only few **C** conformers were observed. This sequence may seem surprising in view of the gas phase energetics (see the Supporting Information, Fig. 6.5). In the gas phase, the total energy of **T** is lowest because both bipyridine subunits are in their lowest-energy form[197], which avoids repulsion between the lone pairs of N and enables the formation of intramolecular hydrogen bonds [199]. The energies of **TC** and **C** are higher by $\approx$ 0.25 and 0.52 eV, respectively. However, it is unlikely that the deposition process leads to the formation of an equilibrium distribution. The intact grid complexes arriving at the substrate comprise **b-tpy** ligands in *cisoid* conformation (cf. Fig. 6.1b). The loss of Co ions during the adsorption will favor the *trans* form over the *cisoid* form. The lower abundance of the **T** conformer may thus reflect that its formation requires rotations of two R_{pm} rotamers while **TC** is obtained by transforming a single rotamer only.

All the monomers except **T**′ are found to form dimers (Figs. 6.4a–f) either with themselves or with any of the other conformers. **TC** conformers bind themselves in four different configurations (Figs. 6.4a–d). Close inspection of Figs. 6.4a and 6.4b reveals that the surface induces chirality of the asymmetric **TC** conformer [200, 201]. Both dimers of Figs. 6.4a and 6.4b are composed of different enantiomers of **TC** whereas the other two patterns in Figs. 6.4c and d comprise the same two-dimensional enantiomers. Conformers **C** and **T** were rarely observed to form dimers with **TC** (Figs. 6.4e and 6.4f).

As confirmed from the calculations (details in the Supporting Information, Section IV), all these dimers ensue from the interaction between bipyridine moieties via hydrogen bonds. The *trans* conformations of NC–CN rotamers associated with bipyridine moieties (highlighted in cyan in Fig. 6.1) lead to the exposure of N atoms at their outer surfaces, which may be considered as docking sites that attract a second monomer. As an example, the optimized configuration of the dimer of Fig. 6.4a is shown in Fig. 6.4g, where N atoms

---

[2]Cobalt atoms dissociated from the ligands were not observed on terraces. We suppose that they diffuse to step edges during the deposition at ambient temperature. Indeed, bulky clusters of material were observed at step edges. In addition, some clusters that appeared fuzzy in STM images were found on terraces and at steps. They may be due to BF_4 or Co.
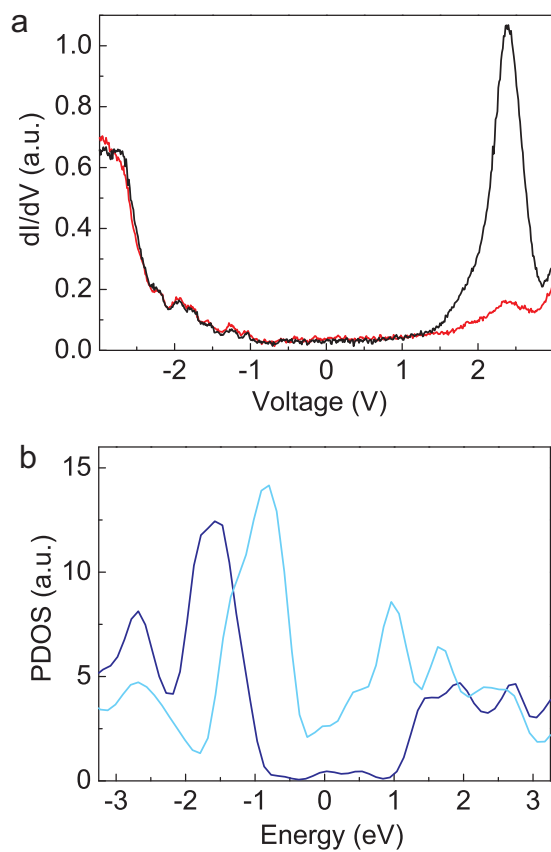
Figure 6.3: (a) dI/dV spectra of a ligand recorded above the pyrimidine (black) and bipyridine (red) subunits. (b) Calculated PDOS of **C** conformer (blue) and cobalt-coordinated **b-tpy** ligand (Fig. 6.1b). The sums of s and p (and d for cobalt-coordinated configuration) contributions from each of the atoms of the ligand are shown. Similar results were obtained for the other conformers as well as for the cobalt-coordinated structures.
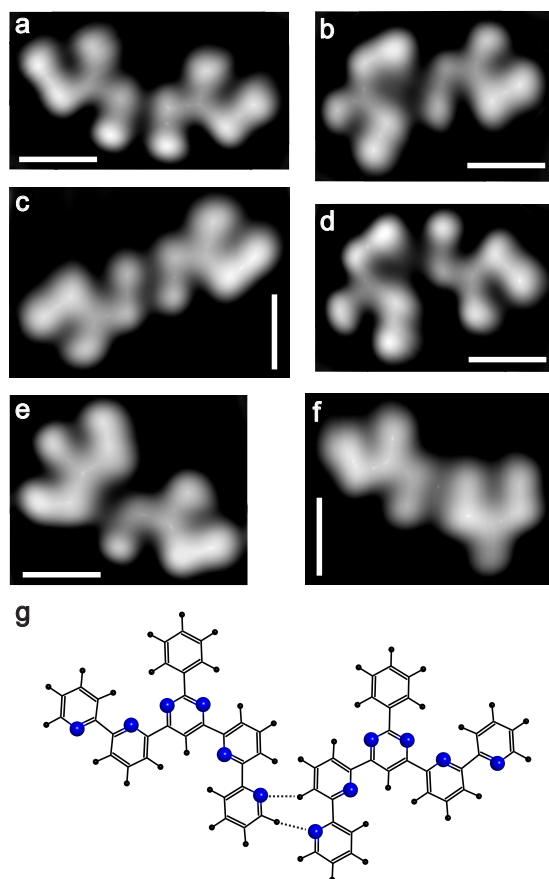
Figure 6.4: (a,b) Dimers consisting of different two-dimensional enantiomers of **TC** (c,d) Patterns composed of the same enantiomers of **TC** (e,f) Dimers comprising different conformers. Scale bars correspond to 1 nm in all the images. (g) Optimized model of the dimer of Fig. 6.4a. Blue and black dots represent N and H atoms, respectively.

of the constituent conformers form hydrogen bonds with the other molecule (shown by dotted lines). The optimized structure does not exactly match the experimentally observed configuration, possibly because the surface was not included in the model calculations. Moreover, the conformers were restricted to a plane during the optimization.

T' conformers were never observed to form dimers. With both bipyridine moieties in *cis* form all four N atoms are oriented towards the inside of the molecule (Fig. 6.2f), which prevent them from forming hydrogen bonds. In addition to dimers, which were frequently observed, we occasionally found trimers. Larger clusters were not found.

Conclusion

In conclusion, tetranuclear Co-grid complexes incorporating **b-tpy** ligands were electrosprayed onto a Au(111) substrate under UHV conditions. Complete fragmentation occurs leaving the **b-tpy** ligands in four different conformations. Most ligands are found to form H-bonded dimers. The most abundant conformer on the Au surface is an asymmetric form of the ligand (**TC**), which has not been observed before. Apparently the deposition on the cold Au substrate kinetically favors its formation.

From a broader perspective, the present results also indicate that the fragmentation of coordination compounds during the deposition process in principle allows for the surface trapping, identification and investigation of high energy, out-of-equilibrium conformations of the ligand molecules at low temperatures, which otherwise would not be observable. Furthermore, such studies may also give access to the dynamics of interconversion processes between conformational isomers on a surface at a given temperature.

Supporting Information

I. Conformations of the ligand in gas phase

b-tpy ligands were first calculated with the semi-empirical quantum chemistry program MOPAC2012 [203]. It is based on recently improved NDDO (neglect of diatomic differential overlap) approximations and newly optimized parameters, PM7. Non-covalent interactions were treated with both PM6-DH+ (PM6 [204] plus post-SCF van der Waals and hydrogen-bond corrections [205]) and PM7 [206]. As very similar results were obtained with these two methods, only the results obtained with the PM7 are shown. To model **b-tpy** adsorbed on a Au(111) substrate, all conformers were forced to a planar geometry. The calculations confirm that the most stable conformation for each of **T**, **C**, and **TC** monomers corresponds to the *trans* form of bipyridine moieties. Other stereoisomers are energetically less stable (Fig. 6.5). The sequence of stability (from most stable to less stable, according to the calculated total energies) is **T** > **TC** > **C** > **T**′.

II. Optimization of the ligand conformers on Au(111)

b-tpy ligands were further investigated on Au(111) with density functional theory (DFT) calculations using Vienna ab initio simulation package VASP [207, 208]. We used pseudo-potentials within the projector augmented wave method [209]. The exchange-correlation energy was calculated within the generalized gradient approximation with the functional proposed by Perdew-Burke-Ernzerhof [154, 210]. The kinetic-energy cut-off was set to 440 eV. For **T**, **T**′, and **C** monomers, the simulation supercell had a dimension of 15Å × 15Å × 27.5Å, with the Au(111) substrate described as a slab with 4 layers of 30 atoms each slab. For the **TC** monomer, a larger 15Å × 20Å × 27.5Å cell comprising a slab with 4 layers of 42 atoms was used. Due to the large dimensions of these supercells, only the Γ point was used for Brillouin-zone sampling. A van der Waals correction was made through a modified implementation of the DFT-D2 method [155]. The electronic SCF step was converged within 0.1 meV. All atoms except those of the two bottom Au layers were relaxed until the forces were smaller than 10 meV/Å.

To investigate the possibility of Co atoms attached to distinct conformers of **b-tpy** ligands on Au(111), we also considered structures in which one or two Co atoms were attached to the **b-tpy** ligands.

The calculated adsorption energies E_{ad}, defined as the total energy minus the total energies of the molecule and the substrate alone ($E_{ad} = E_{total} - E_{substrate} - E_{molecule}$), are given in the table below (Table 6.1).

T
E = -5069.603 eV

TC
E = -5069.354 eV

C
E = -5069.082 eV

T_tc
E = -5069.293 eV

T_cC_t
E = -5069.076 eV

C_tc
E = -5068.701 eV

T´
E = -5068.904 eV

T_tC_c
E = -5068.977 eV

C_cc
E = -5068.315 eV

T_cC_c
E = -5068.699 eV
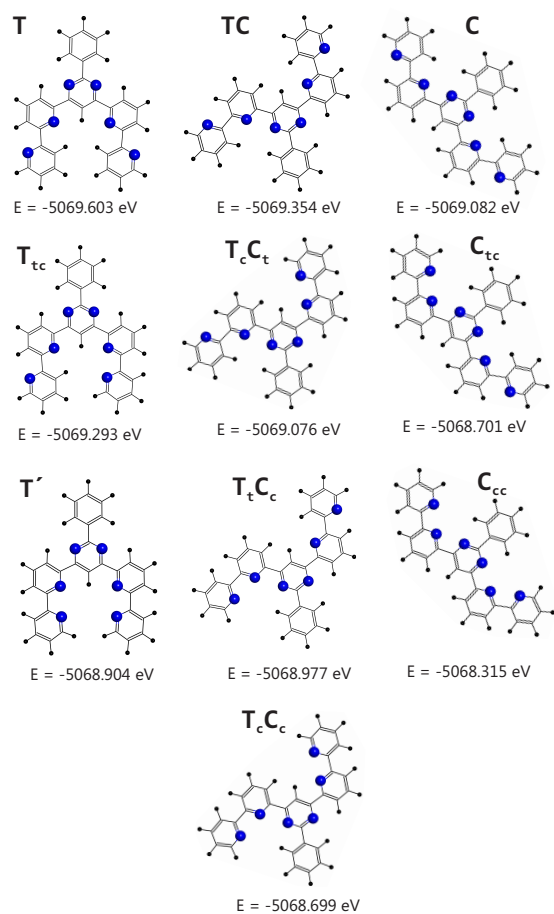
Figure 6.5: Stereoisomers of a **b-tpy** ligand in gas phase. Blue and black dots represent N and H atoms, respectively. The total energies (E) of each of the conformers are given.
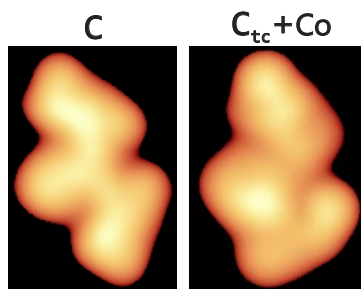
C   **C_tc+Co**

Figure 6.6: Simulated images of **C** and **C_tc**+Co. A protrusion is visible at the position of cobalt for the latter complex.

65

Complexes	E_{ad} (eV)
T	-1.430
T'	-1.035
C	-0.974
TC	-1.472

Table 6.1: Calculated adsorption energies E_{ad} of different conformations.

III. Image-simulation on Au(111)

STM images were calculated with GREEN [211], a program based on extended Hückel theory (EHT) [212]. In this program, the tunneling current is calculated explicitly by applying the Landauer formula [83]. The transmission coefficients are evaluated through a Greens function approach. Calculated images of **C** and **C**$_{tc}$+Co are shown as examples (Fig. 6.6).

IV. Optimization of dimers

b-tpy dimers comprising different conformers were calculated with PM7. The conformers were restricted to two dimensions during the optimization. The lowest energy dimers were found to be stabilized by C—H$\cdots$N hydrogen bonds with intermolecular H-N distances ranging from 2.44 Å to 2.64 Å. However, these configurations are slightly different than experimentally observed patterns. We presume that this is a consequence of the competition between intermolecular and molecule–substrate interactions. Adsorbed dimers on Au(111) were not calculated with DFT because the required computational resources were not available.

Acknowledgement

7

Surface-Supported Supramolecular Pentamers

This chapter is based on a publication in the Journal of American Chemical Society [201].

Abstract

Chiral pentamers of *all-trans*-retinoic acid molecules have been prepared on Au(111) surfaces and on a molecular monolayer. Over a range of coverages, pentamers are the building blocks of larger arrays that become increasingly enantiopure. The stability of pentamers is analysed from experiments on an isomer and a more reactive substrate as well as from density functional theory. The linear shape of the molecule and suitable densities are crucial for the formation of pentamers, driven by cyclic hydrogen bonding between carboxylic acid moieties.

Introduction

Supramolecular chemistry is of great interest in molecular recognition, catalysis, medicine, data storage and processing, and artificial photosynthetic devices [213]. Supramolecules are formed by directional and weak non-covalent interactions such as hydrogen bonding [214], metal coordination [215], hydrophobic and van der Waals forces [216], and $\pi - \pi$ and electrostatic interactions [217]. Hydrogen bonding is particularly attractive for self-assembly for its directionality, specificity, and biological relevance [218].

On surfaces, supramolecular structures are affected by direct interactions with the substrate [219]. In addition, substrate-mediated long-range molecule–molecule interactions occur and lead to discrete supramolecules instead of closely packed molecular arrays. Supramolecular dimers, trimers, and tetramers of porphyrines and azobenzene derivates have been self-assembled using these principles [220]. However, the fabrication of supramolecules with C_5 symmetry, which are mainly found in living organisms, has rarely been reported [221], most likely because a two-dimensional surface cannot be filled with a periodic arrangements of pentagons [222].

Here we present the preparation of supramolecular pentamers from *all-trans*-retinoic acid (ReA) on the Au(111) surface. Over a range of coverages these pentamers are the building blocks of larger arrays. While the ReA molecules, which become chiral upon adsorption, form a racemic mixture, the pentamers become increasingly enantiopure as larger arrays form. Using a slightly different molecule, 13-*cis*-retinoic acid (*cis*-ReA), or a more reactive substrate, Ag(111), we identify the forces driving the pentamer formation. Density functional theory calculations are used to further characterize the process.

Results and Discussion

ReA was sublimated onto Au(111) at room temperature in ultrahigh vacuum. Images were recorded with a scanning tunneling microscope (STM) operated at 5 K, low constant currents (10–60 pA), and low positive sample voltages (10–150 mV). Molecular double layers were imaged at 2.1 V. Images are displayed as an illuminated three-dimensional surface.

Electronic structure calculations were performed within DFT using a plane wave basis set and the projector augmented wave method [224]. The exchange and correlation energy was treated with the Perdew-Burke-Ernzerhof (PBE) form of the generalized gradient approximation [154] The importance of long-range van der Waals (vdW) interactions was studied using the DFT+D2 scheme of Grimme [155]. Geometries were optimized until forces were smaller than 0.01 eV/Å.

ReA is one of the most active retinoids and essential for the control of epithelial cell growth and cellular differentiation [225]. The molecule has a quasilinear geometry with the carboxyl group (–COOH) at one end. Fig. 7.1a shows a STM image of a supramolecular pentamer that formed upon deposition of ReA on Au(111). As confirmed from DFT calculations the C_5 symmetric pentamer is stabilized by cyclic O...H–O hydrogen bonds at the center (Fig. 7.1b). The bulky 1,3,3-trimethylcyclohexen groups appear as protrusions (0.2 nm apparent height) at the periphery of the supramolecular cluster while the chain-like rest of the molecules (3,7-dimethylnona-2,4,6,8-tetranoic acid, denoted oligoene below) appears lower (0.14 nm).

At low coverages, most ReA molecules arrange themselves into pentamers which interact to form larger agglomerates, inititally in fcc areas of the herringbone reconstruction. While the pentamers can still easily be identified the C_5 symmetry is usually lost. We attribute the reduced symmetry to the van der Waals interaction between pentamers and the flexibility of the oligoene chains on Au(111). In fact, no preference for a particular crystallographic direction of the Au substrate was discernible, in stark contrast to a Ag(111) substrate (see below).

Close inspection of Fig. 7.2a reveals that the surface induces a chirality of the achiral ReA molecule [226]. The two enantiomers, denoted ρ and σ, are shown in Fig. 7.2b. While small islands of a few pentamers (Fig. 7.2a) comprise similar numbers of both enantiomers larger islands (Figs. 7.2c and 3) exhibit a
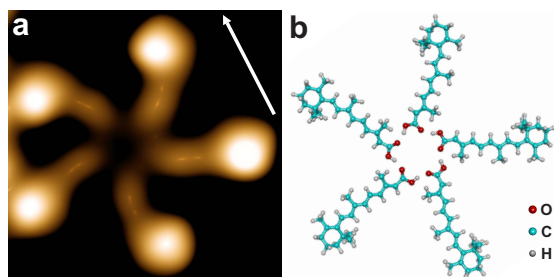
Figure 7.1: (a) Image of a ReA pentamer, observed close to a step on Au(111) at an average coverage $\Theta \approx$ 0.2 ML [223]. In this and all other STM images an arrow indicates a $\langle 1\bar{1}0 \rangle$ direction and its length corresponds to 1.5 nm. (b) Optimized geometry of five ReA molecules, confined to a plane.
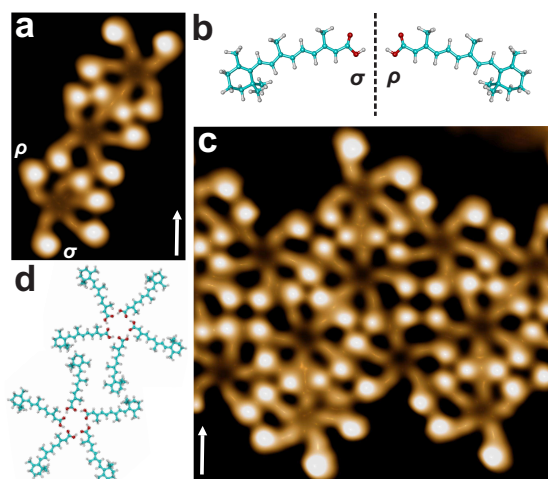
Figure 7.2: (a) STM image of three pentamers comprising different enantiomers of ReA at $\Theta \approx 0.4$ ML. ρ and σ indicate examples. (b) Surface-induced enantiomeric forms ρ and σ of ReA. (c) STM image of a larger pentamer array. (d) Schematic geometry of two pentamers attracted by van der Waals interaction.
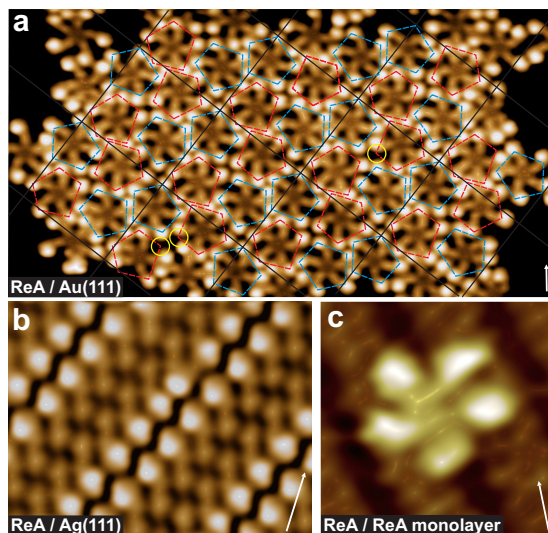
Figure 7.3: (a) STM image of ReA pentamers on Au(111) in a rectangular two-dimensional mesh at $\Theta \approx 0.75$ ML. Solid lines indicate some unit cells with dimensions 5.7×5.2 nm^2. The unit cell comprises four pentamers. Red and blue pentagons indicate pairs of pentamers with different distortions that are not congruent. The pentamers at the interior of the island contain only σ molecules. The two pentamers marked red (blue) are rotated by 180° with respect to each other. Defects in the interior of the pentamer array are marked with yellow circles. (b) ReA on Ag(111). The molecules form a densely packed, striped structure. The dimensions of the oblique unit cell are 3.6×0.82 nm^2 with an angle of $54 \pm 1°$ between the primitive vectors. (c) STM image of a pentamer grown on top of an ReA dimer island on Au(111) with monolayer thickness.

significant ($\sim 10 : 1$) excess of one enantiomer. Most molecules with the minority chirality are found at the perimeter of islands. From an analysis of many islands we found that all pentamers that are surrounded by more than four neighboring pentamers are comprised of five identical enantiomers and thus are chiral themselves [227]. These observations indicate the importance of homochiral interactions. At coverages below 0.2 monolayers (ML [223]), $\sim 5\%$ of the pentamers are enantiopure as expected for random aggregation of σ and ρ enantiomers. This fraction increases to $\sim 80\%$ in pentamer islands at ~ 0.75 ML. The mechanism of enantioselectivity may be thermally induced chiral switching [32]. In such a process the bulky 1,3,3-trimethylcyclohexen groups would flip along the oligoene chains, thus change the handedness of the molecules and enable the growth of pentamers into homochiral extended islands.

Although a planar surface cannot be completely filled with regular pentagons Fig. 7.3a shows that ReA pentamers are capable of forming large ordered arrays with a pattern resembling a pentagonal Cairo tiling [228]. Given the large size of the unit cell (black lines in Fig. 7.3a), which comprises two pairs of pentamers, *i.e.*, 20 molecules, the number of defects (yellow circles) of the structure is surprisingly low. This is attributed to a degree of flexibility of the pentamers, which adapt themselves to form a rectangular unit cell with two different pairs of distorted supermolecules. Moreover, the open structure of the periphery of the pentamers enables some interlocking with the ReA molecules from neighboring pentamers (cf. Fig. 7.2d). From a pentagonal cyclooligomer a similar scenario was reported [229]. In that case, the intermolecular interactions attributed to interdigitating alkoxy substituents. Both cases are different from that of rigid pentagonal molecules where parallel and antiparallel linear packings and a so-called rotator phase have been reported [230]. In small arrays (Figs. 7.2a and 7.2c), where most of the pentamers are part of the rim, the molecular orientations are less well ordered.

To address the role of the molecule–substrate interaction, we repeated the experiments on the more reactive Ag(111) surface, keeping all other parameters unchanged. On this surface, no pentamers were found over a wide range of coverages. Instead, densely packed islands were observed (Fig. 7.3b). We attribute this striking difference between the Au and Ag substrates to the different strengths of the molecule–substrate interactions. Our calculations showed that intermolecular hydrogen bonding favors pentamer formation. On Au(111) the interaction with the substrate is too small to change this preference. On Ag(111), the corrugation of the interaction potential is more significant and imposes an alignment of the molecules along $\langle \bar{2}11 \rangle$ directions and thus effectively prevents the formation of pentamers.

From the above results it appears likely that ReA pentamers will form on other inert surfaces as well. As a first test of this idea, a small amount of ReA was deposited on a complete ReA monolayer on Au(111). The geometric and electronic structures of this layer deviate significantly from those of the metallic Au(111) substrate. Nevertheless, pentamers were found on top of the molecular layer (Fig. 7.3c) as expected.

To characterize the driving force for pentamer formation the structure of

n	E^{PBE}	$E^{PBE+vdW}$	$\Delta_{2,n}^{PBE+vdW}$
2	0.76	0.85	0.69
3	0.88	1.01	−0.05
4	0.96	1.23	−0.01
5	1.00	1.45	0.84 / 0.53
6	0.22 / 0.68	0.83 / 1.15	–

Table 7.1: Calculated binding energies, in eV (= 96.485 kJ/mole), of enantiopure ReA clusters. For the hexamer, the first value was found for a cyclic arrangement that is obtained by inserting a sixth molecule into a pentamer. The second, higher binding energy corresponds to a different structure (see Supporting Fig. 7.7) that would require a drastic rearrangement of the pre-existing pentamer. The quantity in the right column shows the relative stability (details in the text) of respective clusters.

ReA clusters was calculated using DFT. To keep the calculation tractable, the interaction with the fairly inert Au(111) surface was neglected but the molecules were confined to two dimensions. This simplification is justified for the following reasons (cf. also Role of the Substrate in the Supporting Information). First, the ReA molecules in pentamers were not observed to exhibit a clear preference for a particular crystallographic direction of the substrate. On the more reactive but structurally similar Ag(111) surface no pentamers were found and the ReA molecules are aligned with respect to the substrate.

Second, at elevated coverages the pentamer islands extend over fcc and hcp areas as well as domain walls of the herringbone reconstruction without significant changes of the molecular arrangement.

Calculated binding energies $E(n)$ of cyclic clusters of $n = 2 - 6$ molecules are displayed in Table 7.1. With increasing cluster size, the binding energy E^{PBE} calculated with the PBE functional continuously grows up to a magic size $n = 5$. Most of the binding of the clusters is due to O...H–O bonds. The energy per O...H–O bond is higher for the dimer (0.43 eV), which can be tracked to an angle closer to 180° and a shorter distance. When adding more molecules, additional H-bonds are formed, but they are weaker because of the spatial restrictions of accommodating the consecutive molecules. That leads to a less open bond (farther from 180°) with larger distances. Finally, the addition of the sixth molecule lowers the energy per dangling bond so much that there is an overall reduction in binding energy, inhibiting the formation of the hexamer and stopping the process at the pentamer. At lower coverages the process is governed by kinetics and pentamers are formed, but a higher coverages the most stable structures per H-bond are formed, *i.e.*, dimer networks (see below). van der Waals interactions ($E^{PBE+vdW}$) further increase the binding energy and do not change the overall trend. Hexamers turn out to be significantly less stable. These results show that the attachment of single ReA molecules to existing

72

clusters is favorable until a pentamer is formed. While fission of pentamers into smaller clusters would lead to a gain of energy, the abundance of pentamers in the experiments shows that this process is inefficient. This indicates that the barrier for fission is significant.

The formation of pentamer arrays as the one shown in Fig. 7.3a was also found to be energetically favorable. We have checked several packing configurations of pentamers, finding that the binding energy per pentamer increases due to the pentamer–pentamer interactions, going up to 1.85 eV in the best of the tested cases.

The effect of the molecular coverage on the formation of pentamers has been systematically investigated in the experiments (additional STM images are shown in Supporting Fig. 7.8). Pentamers were the most abundant structural motif in the range 0.01 ML $< \Theta <$ 0.4 ML although decreasing percentages of pentamers were observed up to $\Theta \approx 1$ ML. At densities exceeding half a monolayer, ordered islands form. They may be viewed as being comprised of supramolecular tetramers (Fig. 7.4a) or dimers (Fig. 7.4b). Optimized geometries of these building blocks are overlaid on the respective STM images. Close to 1 ML, the Au(111) substrate is mostly covered with the dimer pattern of Fig. 7.4b. This is consistent with the results of Table 7.1, which show that the binding energy per ReA molecule is maximal in dimers. To theoretically characterize the interaction between dimers a monolayer in the configuration of Fig. 7.4b was considered. We found a binding energy of 1.51 eV per dimer, considerably larger than the binding energy of an isolated dimer. At coverages below 0.01 ML, we occasionally observed trimers (see Supporting Fig. 7.6). This may be understood from their low stability compared to dimers and tetramers. In Table 7.1 the relative stability is indicated by the quantity $\Delta_{2,n} = 2E(n) - E(n+1) - E(n-1)$ [231]. The larger negative value of the trimers shows their instability. Again, dimers and pentamers are the more stable formations.

Finally, we experimentally address the role of the shape of the ReA molecule. To this end the closely related molecule *cis*-ReA (Fig. 7.5a) was deposited on Au(111) and Ag(111). On both substrates, hexagonal networks of H-bonded dimers were found and pentamers were absent. Fig. 7.5b shows an example on Au(111). This result highlights the relevance of the linear shape of the ReA molecule. In the case of *cis*-ReA, steric hinderance suppresses the formation of closed cycles of O...H–O hydrogen bonds. This is particularly important during the growth process when molecules with different chiralities try to attach to a ReA$_n$, $n < 5$ cluster. Whereas ReA pentamers containing different enantiomers are stable owing to the linear shape of the constituents (Fig. 7.5c), closure of the cyclic hydrogen bond pattern is prevented in *cis*-ReA tetramers when a molecule with different chirality is added (Fig. 7.5d). The calculated binding energies of heterochiral (Fig. 7.5c) and homochiral (Fig. 7.1b) ReA pentamers, 1.42 and 1.45 eV, respectively, are similar although homochirality appears to be slightly favored. This is consistent with the observation of coexisting homo- and heterochiral ReA pentamers.
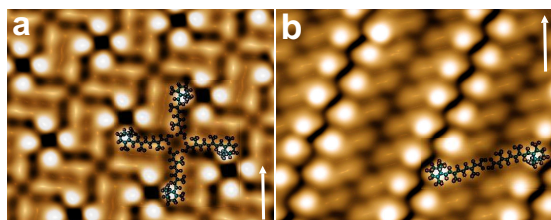
Figure 7.4: STM images of dense patterns observed on Au(111) at elevated coverages. (a) Pattern comprisng ReA tetramers. (b) Striped pattern comprising ReA dimers. The molecules within a given island exhibit the same handedness. Different islands may exhibit different chiralities. Optimized models of a tetramer and a dimer are overlaid.
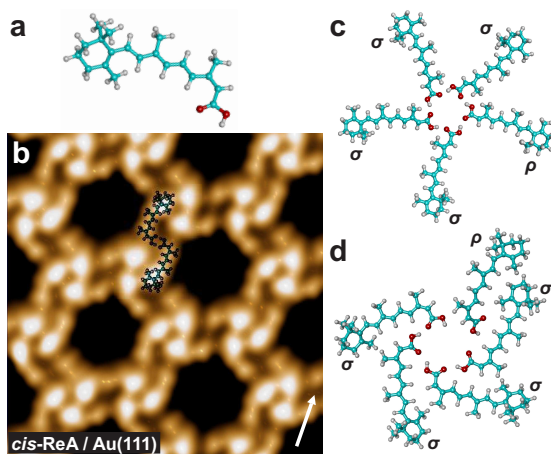
Figure 7.5: (a) Structure of *cis*-ReA. (b) STM image of a hexagonal network formed by *cis*-ReA on Au(111). A virtually identical structure was observed on Ag(111). An optimized molecular dimer is overlaid on the STM image. (c,d) Optimized heterochiral pentamers of ReA and *cis*-ReA, respectively.

Conclusion

In conclusion, pentamers of *all-trans*-retinoic acid molecules have been prepared on the pristine Au(111) surface and a molecular monolayer. Cycles of hydrogen bonds between carboxylic acid moieties stabilize the pentamers. The linear shape of ReA and suitable molecular densities are crucial for pentamer formation. We speculate that related self-assembly of pentamers may be achieved on other weakly interacting surfaces.

Supporting Information

I. Role of the substrate

The lack of a preferred orientation on the Au(111) surface in contrast to the more reactive Ag(111) one, indicates the unimportance of the substrate interaction for the formation of the pentamers. In addition, the observed islands and arrays are not commensurable with the underlying substrate, which is also an indication of the limited interaction. On the other hand, the size of the arrays and the lack of commensurability of the islands prohibits a DFT calculation including the surface. However, test calculations have been done with low precision for individual molecules and dimers. From such calculations, we conclude that the interaction of molecules with the substrate is purely due to van der Waals forces, with charge transfers below 0.2 electrons for the whole molecule, which is around the accuracy of the calculation. We were also able to estimate the energy needed to separate two molecules on the surface, which is equal to 0.90 eV, very close to the value reported in Table 7.1 (0.85 eV). The lack of directional preference, the smallness of the molecule–surface interactions with negligible charge transfer, and the agreement of the dimer binding energy computed with and without surface give us confidence on the ability of the calculations without surface to capture the intermolecular behavior of the supported molecules.

II. ReA trimer on Au(111)

Figure 7.6: Constant current images of ReA trimer on Au(111). Scale bar indicates 1 nm and a $\langle 1\bar{1}0 \rangle$ direction.

III. Optimized geometries of ReA hexamers
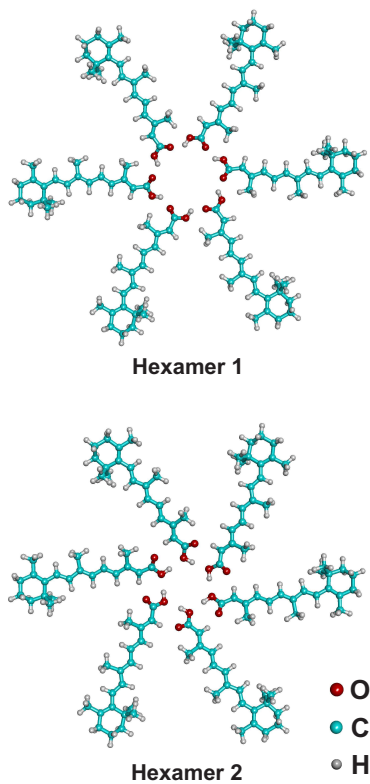
Figure 7.7: Two optimized geometries of six *all-trans--retinoic* acid (ReA) molecules in a plane. Hexamer 1 is obtained by requiring that the hexamer be obtained by inserting an additional ReA molecule into the optimized pentamer. It has a binding energy of 0.83 eV. The binding energy of the fully optimized Hexamer 2 is higher (1.15 eV). However, its formation requires a significant rearrangement of the pentamer. Both the structures have lower binding energies than a pentamer (1.45 eV).

IV. Overview images of ReA on Au(111)
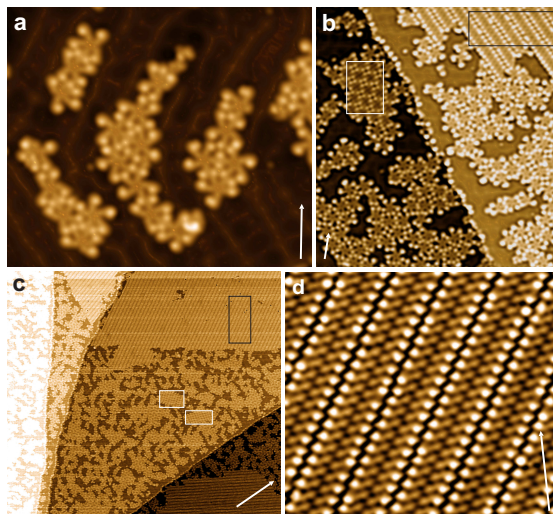
Figure 7.8: Constant current images of ReA on Au(111). Arrows indicate a $\langle 1\bar{1}0 \rangle$ direction. Their lengths indicate 5 nm in (a), (b), and (d) and 50 nm in (c). (a) Image at low coverage ($\theta \approx 0.4$ ML) showing essentially only pentamers. (b), (c) Coexistence of structures at intermediate coverage ($\theta \approx 0.75$ ML). Black and white rectangles indicate islands of dimers and tetramer, respectively. Most other structures are due to pentamers. (d) Close to $\theta = 1$ ML only dimer chains are observed.

coverage in ML	pentamers	tetramers	dimers
0.25	100%	0%	0%
0.4	100%	0%	0%
0.6	87%	1%	12%
1.0	0%	0%	100%

Table 7.2: Fractions of structures observed. Values are based on more than 10 images of $(150 \text{ nm})^2$ for each coverage.

Acknowledgement

8

Spin Manipulation by Creating Single-Molecule Radical Cations

This chapter is based on a manuscript submitted for publication [232].

Abstract

All-trans-retinoic acid (ReA), a closed-shell organic molecule comprising C, H, and O atoms, is investigated on a Au(111) substrate using scanning tunneling microscopy and spectroscopy. In dense arrays single ReA molecules are switched to a number of states, three of which carry a localized spin as evidenced by conductance spectroscopy in high magnetic fields. The spin of a single molecule may be reversibly switched on and off without affecting its neighbors. On the basis of our experiments and density functional theory calculations we suggest that ReA on Au is readily converted to a radical by the abstraction of an electron.

Introduction

Tunable spins in adsorbed molecules are of interest for molecular spintronics applications [233]. Transition metal complexes have often been used in this context [234] because their metal centers provide localized spins that may be protected by the surrounding organic framework. Chemical modifications to their ligand shells [40, 41, 43, 44] were found effective in manipulating spins of adsorbed molecules.

Here we report scanning tunneling microscopy (STM) results from the closed-shell organic molecule retinoic acid (ReA, Fig. 1a) adsorbed to the inert Au(111) surface, a materials combination that does not immediately suggest the presence of spin effects. Surprisingly, however, adsorbed ReA molecules may reversibly be converted between several states some of which carry a localized spin as evidenced by conductance spectroscopy in high magnetic fields. Single molecules in dense arrays may be switched without affecting their neighbors. We suggest that the molecules are switched to a radical state by the removal of an electron from the endocyclic double bond of ReA. Indeed, stable radicals may preserve their spins upon adsorption on surfaces [79, 235–237]. It may be interesting to

note that ReA and its derivatives exhibit great structural flexibility that living organisms use for signal transduction [238].

Results and Discussion

Experiments were performed in ultra-high vacuum with three scanning tunneling microscopes operated at ~ 5, ~ 4.3, and ~ 0.5 K. Au(111) single-crystal surfaces and etched tungsten tips were prepared by Ar ion bombardment and annealing cycles. ReA was sublimated onto Au(111) at ambient temperature in ultrahigh vacuum and imaged at approximately between ~ 0.5 and ~ 5 K. Images are displayed as illuminated three-dimensional surfaces. For detection of the differential conductance, dI/dV, we applied standard lock-in techniques.

Simulations were carried out using dispersion-corrected DFTB as implemented in Hotbit [239] and DFT (GGA-PBE) as implemented in FHI-AIMS [240], both in combination with the ASE package [241]. Dispersion interactions were supplied by the vdW $^{\text{surf}}$-method [242]. Charge resonant excited states were calculated using the leΔSCF approach [243] as implemented in a local version of CASTEP 6.0.1 [244]. More details are available in the Supplemental Material.

Close to monolayer coverage, ReA forms a dense pattern that covers large areas of the Au(111) surface (see Fig. 7.8d of Chapter 7) [201]. Figure 8.1b shows a detailed image revealing that ReA molecules arrange themselves in parallel dimers. The highest protrusions correspond to the bulky 1,3,3-trimethylcyclohexene groups (denoted head groups below) and appear ~ 0.06 nm higher than the rest of the molecules (3,7-dimethylnona-2,4,6,8-tetranoic acid, denoted polyene below). Slight variations in contrast among molecules within the array are likely due to variations of the adsorption site on the atomic lattice of Au(111). Such an incommensurateness is not surprising because the selective and directionally defined H-bonds mediated by the carboxylic groups may prevail over interfacial van der Waals interactions in attaining the eventual structure. No preferred orientation of the molecular patterns on the substrate was observed, which is an indication of a limited corrugation of the molecule–substrate interaction. This finding is furthermore supported by dispersion corrected density functional theory (DFT) simulations of the adsorbed molecule (cf. Section IV of the Supporting Information), where no strong energetic preference of a specific adsorption site was found.

ReA molecules in arrays can be switched selectively among different states by placing the tip over the neck of the bulky heads and lowering the sample voltage to -2.5 V with current-feedback disabled. The process was effected by monitoring the current through the molecular junction, which switched back and forth among well defined levels, and increasing the voltage (to values closer to 0 V) when the current corresponding to a desired state was detected. Figure 8.1c shows an intermediate upshot. Three distinct shapes of the manipulated states, denoted A, B, and C (Fig. 8.1c), surrounded by pristine molecules, are discernible. While the head group in state A appears as an elliptical protrusion, a rounded Reuleaux triangular shape is viewed in state B. State C displays an
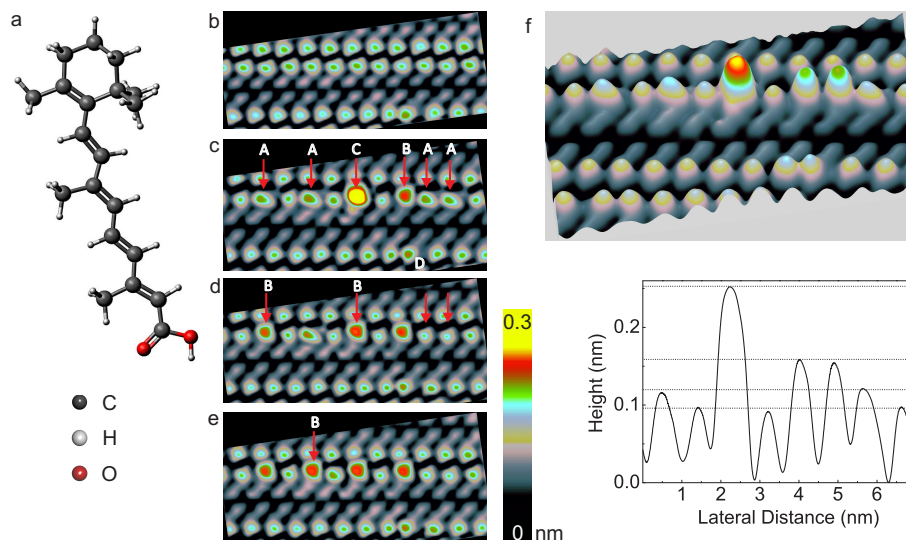
Figure 8.1: *All-trans*-retinoic acid (ReA): Structure, STM image and manipulation sequence. (a) Schematic of ReA. (b) STM image (9.7×4.3 nm^2) of striped pattern comprising ReA dimers on Au(111), acquired at ~ 5 K. The molecules are in their pristine form as deposited. (c) STM image of the same area after manipulating selected molecules at a sample voltage $V = -2.5$ V. Only the manipulated molecules are indicated with red arrows. The different states obtained are labeled A–D. (d, e) Further manipulation steps. Only those molecules that have been modified compared to the previous image are labeled. (f) Pseudo three-dimensional image and a line profile showing the differences in apparent heights of the manipulated states with respect to pristine molecules. All images were acquired with $V = -5$ mV at a constant current $I = 100$ pA. The color scale covers a range of 0.3 nm. The image contrasts were essentially unchanged within the range -2 V$< V <2$ V.

extended protrusion along with a kink in the polyene chain at the back of the neck of the bulky head. Switching was found to lead to some further states the most common one of which is labeled D in Fig. 8.1c.

The manipulated states were found to be stable over periods as long as days at the temperature of the experiments (5 K). Spontaneous conversion was never observed so long as nondestructive currents and voltages (usually $|V| \leq 2$ V) were used for imaging. The degree of selectivity in attaining a particular state is further illustrated in Figs. 8.1d and e. Whereas different states were prepared in Fig. 8.1d (keeping only two manipulated molecules of Fig. 8.1c unchanged), all manipulated molecules have been converted to state B in Fig. 8.1e.

The differences in apparent heights among different states can be seen in the pseudo three-dimensional image presented in Fig. 8.1f along with the line profile taken along the bulky heads of manipulated molecules. The head groups of states A, B, and C appear higher (~ 20, ~ 60, and ~ 140 pm, respectively) relative to pristine molecules [1]. The substantial increase in apparent heights indicates either a strong conformational change of the molecule or a redistribution of the local density of states or a combination thereof. However, the tails of the polyene chains remain essentially unchanged in apparent height. To identify possible geometric arrangements we employed a DFTB/DFT+vdW$^{\mathrm{surf}}$ [242] screening approach (see Section II of the Supporting Information for more details) and found four distinct groups of stable adsorption geometries, for which we also simulated corresponding STM images (Supporting Figure 8.5). Taking into account relative adsorption energies and comparing simulated and measured STM data, we conclude that in its unswitched ground state ReA adsorbs most likely in an *all-trans* configuration. Configurations with an uplifted phenyl group reproduce the switched states observed experimentally, which are characterized by a low tail and a protruding head-group. Depending on the orientation of the phenyl ring, the corresponding Tersoff-Hamann simulations show either elliptical or round protrusions, reminiscent of the different appearances in the experiment.

The electronic properties of all five states of the molecule mentioned above are embodied in the differential conductance (dI/dV) spectra shown in Fig. 8.2a. The featureless spectrum (bottom curve) corresponds to a pristine molecule. Other spectra taken over the center of the bulky heads of the manipulated states surprisingly show (except for state D) a zero-bias resonance, similar to the Kondo fingerprint reported from atoms and molecules on surfaces [33, 38, 42, 103–107]. As the tip is moved sideways along the polyene chain, the resonance vanishes (Fig. 8.2b).

To determine the origin of the zero bias anomaly, the evolution of dI/dV spectra was examined in the presence of a variable magnetic field B. Figure 8.3a shows a series of spectra from the head group in state A recorded at various field strengths. As expected for a Kondo resonance, the zero-bias peak splits as B is increased. Similar results were obtained for state B (Fig. 8.3b). In

---

[1]These height differences correspond to changes of the tunneling current under open-feedback conditions.
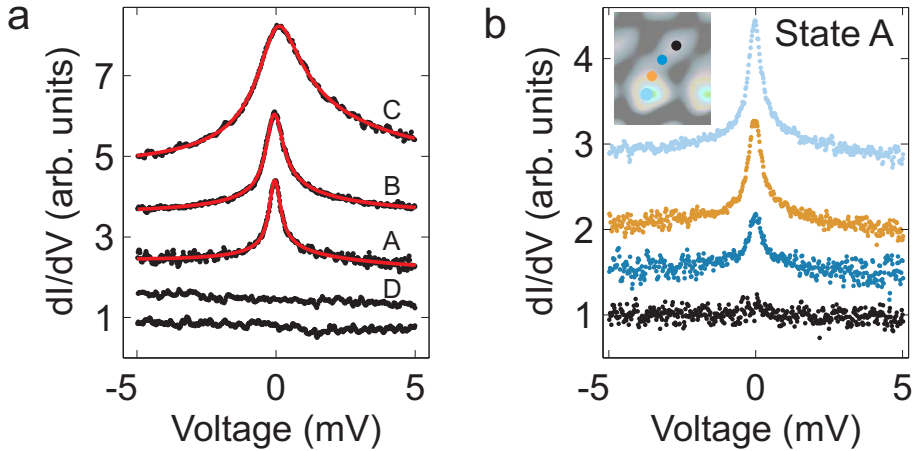
Figure 8.2: dI/dV spectroscopy of pristine and manipulated ReA. (a) dI/dV spectra recorded over the center of the bulky heads of pristine ReA (bottom spectrum) and different manipulated states (labeled A–D). Before opening the current feedback for spectroscopy, the STM was operated at $V = -10$ mV and $I = 100$ pA. Red curves represent fits of Frota functions to the spectra (see Section I of the Supporting Information for details). (b) Spatial evolution of dI/dV spectra along the polyene chain of state A. Colored dots in the inset indicate the positions at which the spectra were recorded. For clarity, the spectra are shifted vertically. Similar results were obtained for other manipulated states.

state C (Fig. 8.3c) no splitting was achieved at the maximum B available at the time of the experiment. However, the involvement of the molecular spin is evident from the significant broadening at $B = 6$ T. These data exclude the possibility that the feature at the Fermi level is due to the excitation of low energy vibrations [245, 246]. Information on the Kondo temperatures and the fitting procedures are provided in the Section I of the Supporting Information. We note that multistability was previously reported from tetracyanoethylene on Cu(111) with one state displaying several low-energy excitations [247]. An excitation around E_F has been attributed to a Kondo resonance, but no field dependence was reported.

None of the stable isomers we identified using dispersion-corrected DFT carried a majority spin in their ground state that would explain the observed Kondo resonance. In addition, no significant charge-transfer between the surface and the molecule was found, implying that pristine ReA remains essentially neutral on the Au surface. We therefore suggest that the molecule is converted to a positively charged radical (ReA^{*+}) during manipulation with the STM, consistent with the application of a negative bias voltage. In the case of solvated ReA, addition of an electron leads to dissociation via deprotonation [248], electron removal leads to a stable radical cation under acidic and alkaline conditions [249]. In line with this interpretation, switching to states that exhibit a Kondo resonance
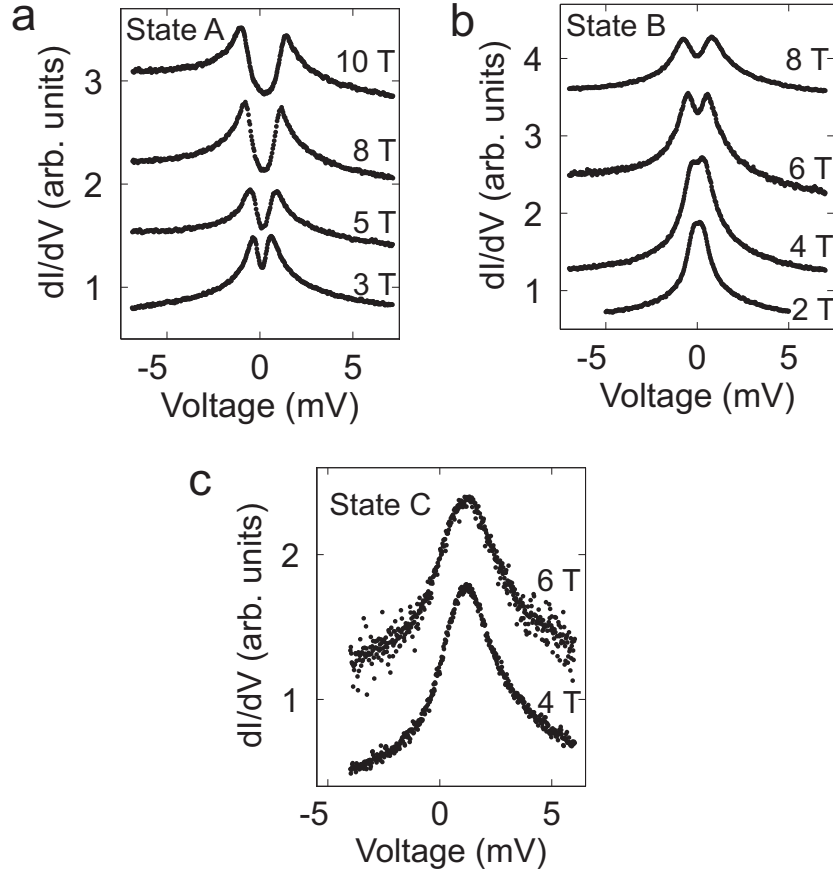
Figure 8.3: dI/dV spectra of states A, B, and C in magnetic fields. The states and the field strengths are indicated in the figure. Splitting of the Kondo resonance of state A is observed at all field strengths. State B displays some splitting at approximately 4 T. State C progressively broadens compared to the zero-field spectrum in Fig. 8.2a. However, up to 6 T no splitting occurs.

was only observed at negative sample voltages. The aforementioned change in the molecular structure is likely to stabilize the charged molecule similar to the case of charged metal atoms on insulating films [250–252].

We investigated ReA also on Ag(111), Cu(111) and Pb(111) surfaces. On none of these substrates ReA could be switched to display a Kondo effect. On the other hand, from 13-*cis*-retinoic acid, an isomer of ReA, we succeeded in preparing spin-carrying states similar to ReA on Au(111). Apparently, the weak coupling of ReA to the inert Au(111) substrate is required to enable structural flexibility and radical formation.

To further explore the charged states, we simulated two excited states of the four optimized geometries on the surface by removing (adding) an electron from the highest occupied molecular orbital (into the lowest unoccupied molecular orbital, LUMO). The energy to remove an electron from the molecule (~ 0.8 eV) is approximately half the energy needed to add an electron to the LUMO (see Supporting Table 8.2). Formation of a cationic state thus appears plausible at the bias voltages used in the experiments to induce switching (-2.5 V). A series of calculations for different molecular conformations showed that these two energies do not critically depend on the conformation. This is expected for different conformers experiencing dispersion-based interaction with the substrate and might indicate that the potential corrugation in the excited state may be further reduced, thus facilitating structural rearrangements and reducing the dependence of excited state lifetime on the molecular geometry. The above addition energy is close to its analogue in gas-phase, the electron affinity. However, electrostatic interaction between the molecular charge and its image charge strongly reduces the electron removal energy of the adsorbed molecule compared to the ionization potential in gas phase, thereby facilitating the formation of a charged radical cation on the surface (see Supporting Table 8.2).

Conclusion

In summary, retinoic acid molecules on gold may be converted to states that carry a localized spin. We propose that a radical cation is created by the removal of an electron from the endocyclic double bond. A possible ramification of this work is to use arrays of ReA and related molecules to create arbitrary patterns of spins. While the direct interaction of these spins may be small the underlying metal surface may mediate long-range interactions.

Supporting Information

I. Estimation of the Kondo temperature T_K

To estimate Kondo temperatures we modelled the spectra at $B = 0$ with Frota functions [113–116] (solid red lines in Figure 2a of the manuscript). From the half-width of the Frota lines we find $T_K \approx 4.1, 6.6$ and 20 K for states A, B and C.

An upper limit for T_K may also be estimated from the minimum field required to induce a splitting of the Kondo resonance. For state A, splitting becomes discernible at approximately 2 T which indicates $T_K \leq 5.4$ K [253]. This value is consistent with the result of the line shape analysis.

II. Computational Details on adsorbate geometry screening

The simulations were performed using dispersion-corrected DFT (DFT-vdW) as implemented in ASE [241] and FHI-AIMS [240] with dispersive interactions supplied by the vdW$^{\text{surf}}$-method [242]. The large number of internal degrees of freedom of ReA (Figure 8.4) leads to a vast library of possible adsorption geometries. It is therefore crucial to find an efficient way of sampling the whole parameter space without loss of accuracy. We take advantage of the fact that for the physisorption of organic molecules on Au(111) dispersive interactions dominate [254]. Therefore only the electronic structure of the molecule and the topmost metal layers is explicitly included in the DFT calculation, while the lower-lying metal layers are considered by semi-empirically including additional long-range pairwise interactions.

Figure 8.4: Internal coordinates of Retinoic acid (gray: carbon, red: oxygen, hydrogen atoms omitted for clarity)

To further reduce the computational demand, a first prescreening of a large number of possible adsorption geometries and sites was performed using dispersion-corrected density-functional tight-binding (DFTB-vdW) [255] using the Hotbit software package [239]. This allowed to optimize 122 different ReA conformations obtained by systematically varying the internal parameters displayed in

Table 8.1: Optimized geometry parameters calculated with FHI-AIMS for the four ReA conformers depicted in Figure 8.5. Φ and Ψ are the dihedral angles depicted in Figure 8.4, d refers to the distance above the surface (for nomenclature see Figure 8.4). CASTEP values are given in parentheses.

structure	d_{CO_2}	$d_{C_{7,8}}$	Φ	Ψ
all-trans	3.23 (3.25)	3.40 (3.32)	179 (176)	172 (172)
cis	3.10 (3.00)	3.22 (3.25)	354 (353)	317 (320)
dimethyl	3.31 (3.18)	3.83 (3.89)	163 (165)	318 (317)
methyl	3.00 (2.96)	5.65 (5.50)	345 (342)	299 (296)
	(in Å)		(in deg)	

Figure 8.4. All calculations were conducted using a periodic supercell containing the retinoic acid molecule adsorbed on a six-layered 3x7 surface slab of Au(111) (cf. Figure 8.5), where the two topmost layers were explicitly described by DFTB. The initial adsorption geometries were chosen such that the C-C bonds of the ring system are inclined by 30° with respect to the Au-Au direction and the nearest distance between atoms of the surface and the molecule does not lie below 2 Å. Approximately 25% of these 122 initial configurations were unstable, the remaining structures all can be classified in four subgroups, in the following denoted as *all-trans*, *cis*, *methyl*, and *dimethyl*. These four basic on-surface adsorption geometries were then used as initial input structures for geometry optimizations using a full DFT description.

DFT optimizations of the four adsorbate geometries were done using FHI-AIMS and the PBE functional [154] on a 3x7x6 Au(111) ($a_{Au} = 4.19$ Å) slab. The geometry optimizations included two gold layers explicitly with FHI-AIMS, whereas the pairwise dispersive interaction was supplied for the whole system. The calculation of adsorption energies and the local density of states (LDOS) included four explicit DFT layers. The basis set was chosen as the light standard numerical atom centered set for the geometry optimization and tight for calculation of the adsorption energies and the LDOS. The convergence criteria for the maximum force were set to 10^{-3} eV/Å, 10^{-4} eV for the total energy and the density convergence set to 10^{-7} Å^{-3} difference between consecutive iteration steps. The calculations were performed using periodic boundary conditions and a 2x2x1 (4x2x1) k-point grid for optimizations (adsorption energy calculations). The scalar zeroth order relativistic atomic scaling (ZORA) was applied for heavy atoms with a threshold of 10^{-6} eV. Gaussian broadening of the Fermi electron occupations with 0.1 eV was applied. In the calculation of dispersive interactions, the system was separated into two domains, namely the adsorbate and the surface. The adsorbate-surface and lateral interactions between the periodic images of the molecules were included but intramolecular contributions discarded. The C_6^{AB} coefficients for Au were rescaled by 0.9452, a constant

which arises due to the fact that the vdW^{surf} scheme is referenced to atomic volumina in a metal bulk [256, 257]. The overall convergence criterion for the geometry optimizations was chosen to be a maximum force of 0.025 eV/Å using the BFGSLineSearch algorithm as implemented in ASE.

III. Computational Details on spin-polarization and electronic structure

The LDOS used in the preparation of Tersoff-Hamann [65] STM topographs was calculated with bias voltages of -2.5, -1.5, +1.5, and +2.5 Volts on a grid spaced with 0.1 Å. In order to compare the Tersoff-Hamann STM topographs, the apparent height was plotted normalized with respect to the overall maximum and minimum isodensity values that were found.

All geometry optimizations have been performed neglecting spin degrees of freedom, whereas energy evaluations have been done accounting for spin using independent, collinear spin channels. In order to impose spin and charge constraints on the system we additionally simulated the molecular orbital projected DOS (MOLPDOS) and leΔSCF^{EX} excitations as implemented in the periodic plane wave code CASTEP [243]. The re-optimization of the four isomers on an explicitly treated four-layered Au(111) slab (3x2x1 k-point grid, >20 Å vacuum) using a local code version of CASTEP and a standard parameter set (450 eV plane wave cutoff, PBE+vdw^{surf}, collinear spin) confirmed the relative stability of the four conformations with only minor changes of the adsorbate structure (see Table 8.1 for comparison).

MOLPDOS and leΔSCF^{EX} excitations have been calculated on top of these geometries using 100 additional bands. In all cases cationic and anionic excitations have been calculated by removing an electron from the projected HOMO or adding an electron to the projected LUMO of the gas-phase molecule in the corresponding adsorbate geometry. The gas-phase reference orbitals have been generated in the same supercell geometries with the underlying substrate removed. The MOLPDOS reference orbitals are ground state Kohn-Sham states, the leΔSCF^{EX} reference states are calculated from a conventional ΔSCF(HOMO$\rightarrow$LUMO) calculation. Excitations have been enforced within one spin channel.

IV. Details on predicted adsorbate geometries

By sampling a large range of possible conformations according to the procedure described in the previous section we find four stable adsorption geometries of ReA/Au(111) (Figure 8.5a) representative of the aforementioned subgroups all-trans, cis, dimethyl, and methyl. During the computational screening described in section II the parameter space of internal coordinates was sampled on the DFTB level giving rise to differences in lateral displacements of head and tail groups (i.e., different adsorption sites). These did not lead to substantial changes
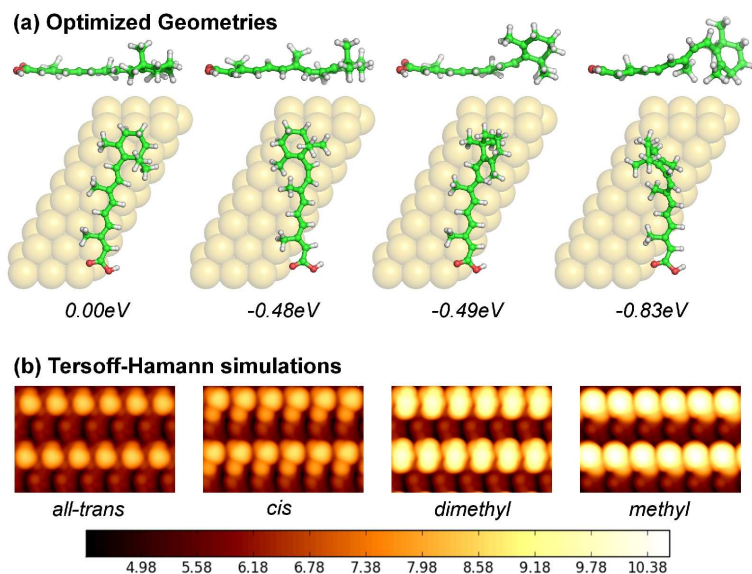
(a) Optimized Geometries

0.00eV   -0.48eV   -0.49eV   -0.83eV

(b) Tersoff-Hamann simulations

all-trans   *cis*   *dimethyl*   *methyl*

4.98   5.58   6.18   6.78   7.38   7.98   8.58   9.18   9.78   10.38

Figure 8.5: Results of the DFT simulations for retinoic acid adsorbed on a Au(111) surface. The **(a)** optimized geometries are ordered from left to right by decreasing adsorption energy, i.e., *all-trans* is the most stable configuration. The conformational characteristics (e.g., uplifted head group) are reflected in the intensity distribution of the **(b)** corresponding Tersoff-Hamann STM images.

in either adsorption energies or conformations within the four subgroups. Table 8.1 compares the most important geometry parameters of the four isomers *all-trans*, *cis*, *dimethyl*, and *methyl*, namely the dihedral angles Φ and Ψ (cf. Figure 8.4) and the vertical distance of the carbon atom of the $-CO_2$ end group and the C_7 and C_8 atoms.

The most stable system (leftmost in Figure 8.5a) is the *all-trans* conformation, which is characterized by the conjugated system being exclusively in *trans* configuration. Both the ReA chain and the head-group adsorb entirely flat and parallel to the Au(111) substrate as indicated by the nearly identical adsorption height (3.25 and 3.32 Å, respectively) of the carboxyl-group and carbon atoms C_7 and C_8. Also, the dihedral angles Φ and Ψ are very close to 180°, which is the ideal value of a trans-configured bond. The corresponding simulated STM image (leftmost in Figure 8.5b) is characterized by a relatively dark chain and brighter head-group.

In the *cis*-isomer (second from the left) one of the bonds near to the predominantly aliphatic ring system is rearranged in a cis-conformation (as can be seen by the values of Φ and Ψ approaching 360°). This leads to an increased overall adsorption distance (by 0.1 - 0.25 Å) in the backbone compared to the *all-trans* isomer, mainly attributed to the fact that the cis-bond approaches the surface due to less steric strain. This increased cis-bond/surface interaction leads to

two geometrical effects: First, the headgroup is lifted from the surface and second, the C_9-attached methyl group is now pointing outwards, protruding away from the surface. The resulting buckling of the polyene chain is reflected in the varying intensities in the corresponding simulated STM signature.

The two isomers shown on the right side of Figure 8.5 correspond to a conformation where the ring system is rotated by 90° with respect to the conjugated chain such that either the *dimethyl* ($\Psi = 317°$) or *methyl* ($\Psi = 296°$) group points towards the surface. Since this sterically requires to lift the center of mass of the headgroup from the surface, the values of the adsorption distance between the carboxyl-group (acting as an anchor and keeping the molecule attached to the surface) and the $C_{7,8}$ carbon atoms differs by 0.7 and 2.5 Å, respectively. Both geometries are stabilized by tripodal arrangements of functional groups which prevent the isomerization in the *all-trans* or *cis* isomers. For these configurations the tilting of the headgroup leads to a largely increased apparent height, while the intensities of the chains remain very similar to those of the *all-trans* configuration (Figure 8.5b).

Each of the four simulated STM images has a distinct appearance, characterized by the relative intensities and symmetry between the polyene chain and the aliphatic ring system. The signature of the most stable configuration (*all-trans*) is also the one which agrees most with the unswitched isomers observed in the experiment. Thus we tentatively assign the unswitched ReA species to a configuration where both the chain and the head group adsorb flat on the surface. None of the switched states exactly resembles the *cis*-isomer, so that we cannot directly assign this conformation to any of the measured states. The structures *methyl* and *dimethyl* are characterized by more severe geometric distortions, i.e., the rotation and uplifting of the ring system, which lead to a significant increase in the intensity of the molecule's headgroup. These signatures (bright headgroup, dark chain) are characteristic for the experimentally observed switched states, therefore we tentatively assign those to structures with an upwards tilted phenyl ring. Such a geometry change might be induced by a resonant charge transfer to or from the molecule. In the case of free ReA charged states have been found experimentally, anions [248] as well as cations [249].

V. Details on spin-polarization and charged states

Upon including spin degrees of freedom and re-optimization of the four selected adsorbate geometries we find no significant structural changes or spin polarization in all four geometries. This is expected considering the charge-neutral ground state and the dispersion-dominated interaction between surface and adsorbate.

In order to simulate the expected resonant charge and spin transfer we modeled two excited states by addition and removal of an electron into the LUMO and HOMO of the adsorbate, respectively. Table 8.2 summarizes the ground and excited state energies for the selected model geometries, small deviations in relative adsorption energies to those in Figure 8.5 are due to previous re-

Table 8.2: Adsorption energies of the four ReA conformers and vertical excitation energies as calculated with leΔSCF$^{\text{EX}}$ with CASTEP. E_{LUMO,e^-} and E_{HOMO,h^+} refer to the addition and removal of an electron in the LUMO and HOMO of the adsorbed molecule. $E_{\text{LUMO},e^-}^{gas}$ and $E_{\text{HOMO},h^+}^{gas}$ refer to the corresponding quantities for the gas-phase molecule.

in eV	E_{ads}	E_{LUMO,e^-}	E_{HOMO,h^+}	$E_{\text{LUMO},e^-}^{gas}$	$E_{\text{HOMO},h^+}^{gas}$
all-trans	2.22	1.45	0.74	1.37	6.67
cis	1.69	1.44	0.76	1.33	6.77
dimethyl	1.70	1.44	0.85	1.34	6.94
methyl	1.37	1.48	0.87	1.38	6.74

optimization of the selected geometries (cf. section IV). As discussed before the *all-trans* structure is by far the most stable geometry, further evidencing that this corresponds to the stable initial adsorption geometry of ReA adsorbed to Au(111).

However, the corresponding energy cost to add or remove electrons from the molecule is almost constant up to the accuracy that can be reached with this approach. This can be understood from the Kohn-Sham orbital energies (not shown) of the ground state isomers adsorbed to Au(111). For all conformers the orbital energies of the adsorbate frontier orbitals are almost unchanged. This is due to the dominantly dispersion-based interaction with the substrate and the almost negligible ground-state charge transfer between substrate and adsorbate. As a consequence there is no significant difference in hybridization or interaction strength with the image charge potential between the studied adsorbate geometries that would be resolvable with this method. This may indicate two things: First of all the potential corrugation in the excited state is significantly reduced, which will facilitate structural changes and geometrical stabilization of the resonant charge state. Secondly, once such a state is formed its lifetime will not strongly depend on the molecular geometry.

To assess the effect of surface adsorption on the excited states of the molecule we have calculated electron addition and removal energies for the above molecule geometries without the underlying surface (see Table 8.2). The corresponding electron addition energies are almost unchanged, suggesting minimal screening and changes due to surface adsorption. However the electron removal energies of the gas-phase molecule, or rather the ionization potential, is much larger than for the metal-adsorbed molecule. The large reduction of the electron removal energy upon adsorption is due to the stabilizing electrostatic interaction between the molecular charge and an image-charge build-up in the surface. The fact that the surface largely facilitates the creation of a positively charged state further supports the interpretation of a tunneling-induced charge-abstraction in Retinoic acid on Au(111).

Acknowledgement

9

Generating Spins in Single Cholesterol Molecules on Gold

This chapter is based on a manuscript prepared for publication [258].

Abstract

Compact islands of cholesterol on Au(111) were investigated with scanning tunneling microscopy at $\sim$ 5 K. By current injection, single molecules have been switched among several states, three of which exhibit a sharp spectroscopic feature at the Fermi level. This feature signals the presence of a localized spin and suggests that the molecule may be controllably switched between paramagnetic and diamagnetic states.

Introduction

Most materials investigated in spintronics are metallic compounds and semiconductors [15, 16]. Recently efforts have been made to establish organic spintronics [259], one reason being that weak spin-orbit and hyperfine interactions in organic molecules tend to imply long spin coherence times [260]. A few stable organic radicals have already been shown to preserve their spin on surfaces [235, 237]. Moreover, electron transfer from the surface can induce a magnetic moment in organic complexes [261]. Here we report indication that a spin can be generated and quenched in cholesterol, a closed shell molecule, on the Au(111) surface. A scanning tunneling microscope (STM) was used to create a radical cation via hole injection from the tip into the molecule.

Cholesterol (Fig. 9.1a) consists of four fused hydrocarbon rings (denoted tetra-cyclic unit below) linked to an isooctyl chain, with a hydroxyl group attached to the cyclohexane ring (highlighted in red) at the far end. A pseudo-three-dimensional schematic viewed across the plane of the hydrocarbon rings shows that two methyl groups attached to the hydrocarbon rings protrude from the plane of the tetra-cyclic unit and the octyl chain. It may be interesting to note that the molecule is an essential component of cell membranes, plays a vital role in lipid metabolism, and contributes to the functions of living organism through signal transduction [262–264].

Results and Discussion

Cholesterol was sublimated onto Au(111) at room temperature in ultra-high vacuum. Experiments were carried out with a STM operated at ~ 5 K. Electrochemically etched tungsten wires were used as tips, treated *in situ* by indenting into the Au substrate.

Figure 9.1b shows an image of a molecular island formed upon deposition on Au(111). The ellipse drawn on the image indicates a single molecule (also see Fig. 9.1c). The tetra-cyclic units of the molecules appear to lie flat on the surface with the methyl groups, attached to hydrocarbon rings, in upright orientation. This apparently causes the dumbbell shaped protrusions appearing higher (apparent height ~ 0.21 nm) than the octyl chains (discussed in detail below). Incommensurate adsorption of the molecules with respect to atomic lattice of the substrate leads to slight variations from molecule to molecule.

Much of the surface is cluttered with molecules (as in the right part of Fig. 9.1b), although some short-range order is seen with strings of molecules arranged in parallel or antiparallel. In addition, rhombic pores surrounded by cruciform patterns (examples marked in white in Fig. 9.1b, acute angle $\sim 84°$) are frequently observed within the agglomerates. These arrangements involve a head-to-head orientation of the molecules which is likely caused by intermolecular hydrogen bonds among hydroxyl groups. Previous studies of cholesterol monolayers at a variety of liquid-solid interfaces have also shown the molecules to be oriented head-to-head in pairs, owing to hydrogen bonds between the hydroxyl groups [265–268]. Parallel arrangements of dimers have also been reported and attributed to interaction through the tetra-cyclic units [267]. This is consistent to our observations of molecules being mostly grouped in parallel, although in small domains.

Closer inspection of Fig. 9.1c reveals two distinct adsorption geometries of the molecules. While the octyl chains of some molecules are imaged as elliptical protrusions with apparent heights of ~ 0.16 nm, others appear lower (~ 0.1 nm). This difference may be understood from the flexibility of the octyl chains, which is also observed in crystal structures [269]. The chains may adapt their geometries to maximize the van der Waals interaction with the substrate and to reduce the steric repulsion within a molecule as well as with neighbors [270]. The pattern surrounded by an ellipse in Fig. 9.1c is consistent with a fully extended anti form of the octyl chain (Fig. 9.1d), which is the energetically most favored structure [269]. In this form, the methyl end-groups of the octyl chain are located at heights similar to that of methylenes and the chain as a whole remains at a height below the methyl groups attached to the tetra-cyclic unit. The other pattern presumably corresponds to a conformation of the chain involving one of the C–C bonds in gauche form (marked with curved red arrow in Fig. 9.1d), which leads to an upright orientation of one of the methyl end-groups and to an elliptical protrusion in STM images.

Each of the molecules may be switched to a number of states by applying voltage pulses to the center of the tetra-cyclic unit (red crosses in Fig. 9.2a). A particular state was obtained by changing the sample voltage to ~ -2.5 V
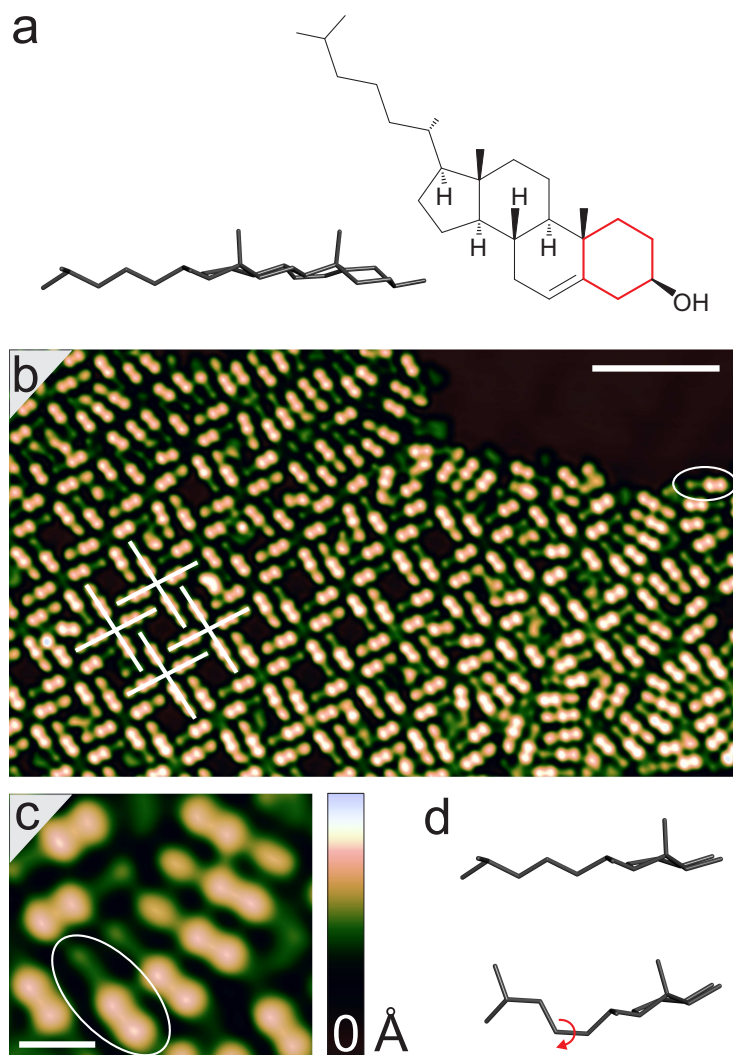
Figure 9.1: (a) Schematics of cholesterol displayed in different viewing angles. (b) STM image of molecules agglomerated into an island on Au(111). (c) Zoomed-in image showing two different adsorption geometry of the molecule. Images were acquired with sample voltages $V = -0.1$ V at constant currents $I = 100$ pA. The data are displayed in a pseudo-three-dimensional fashion with the color scale covering a range of 0.38 nm. Scale bars correspond to 5 nm in (b) and 1 nm in (c). (d) Left half of the cholesterol molecule shown with vicinal groups of the octyl chain in anti (top) and a combination of anti and gauche conformation (bottom). The gauche conformation involves the C–C bond marked with red curved arrow.

from a value of approximately ~ -1 V with the current-feedback disabled and subsequently monitoring the current I. V was changed back to its original value when an abrupt change of I, which typically occurred on a time scale of seconds, signaled a change of the molecule. This procedure had the effect to freeze the manipulated state. The images in Fig. 9.2b–d illustrate a sequence of switching events. Figure 9.2b presents the result of hole injection to the molecules indicated with crosses in Fig. 9.2a. The applied pulses switched the molecules to two states denoted A and B in Fig. 9.2b. A few other molecules in the island suffered changes to state A as well. Inelastic scattering of electrons propagating through the surface may induce these changes [46, 271]. Moreover, it is conceivable that a geometrical change of a molecule is transmitted via lateral forces within the close-packed islands.

Figure 9.2c shows two other states, which are denoted C and D below, of the molecules that resulted from another four pulses applied at the positions marked in Fig. 9.2b (red crosses). In addition, a few molecules were also switched to state A by those pulses.

The tetra-cyclic unit of state A appears as a rounded trapezium with an apparent height similar to that of pristine molecules. In state B, one end of these rings appears higher than the other with a sharp depression between them. C and D appear quite similar to each other with the cyclohexane ring (red in Fig. 9.1a) at the far end of the tetra-cyclic unit being slightly higher (~ 0.1 nm) in C than in D. The octyl chains remain essentially unchanged in all states. Molecules were found to be stable in any of these manipulated states at ~ 5 K, although spontaneous conversions of octyl chains from gauche to anti form (*vide supra*) were often observed while imaging at slightly elevated voltages $|V| > 0.5$ V. The substantial increase in apparent heights at the far end of the tetra-cyclic units appears to indicate a conformational change of the cyclohexane ring. Although the tetra-cyclic unit is planar, the cycohexane ring can adopt other conformations as observed in crystal structures [269].

Figure 9.2d recorded after Figure 9.2c demonstrates that the switching may be reversed by additional pulses. While state C (in Fig. 9.2c) was switched back to the pristine state, state D was changed to A. Conversely, one of the molecules in state A was switched to state D. Furthermore, another B state was prepared from a pristine molecule (cross mark in Fig. 9.2c).

Differential conductance (dI/dV) spectra of all observed states of the molecule are presented in Fig. 9.2e. Pristine molecules (bottom spectrum) and molecules in state A have featureless spectra in an energy range close to the Fermi level ($V = 0$). The spectra of the other states surprisingly show zero-bias resonances. They were found all over the molecules except the very end of the octyl chains. Slight variations of the resonance-width were observed from different manipulated molecules, presumably due to small differences in their local environments. The reversibility of the switching observed in Fig. 9.2 shows that dissociation of the molecule does not occur.

The small width of the resonance close to the Fermi level, in particular in state D (≈ 12 meV), is difficult to reconcile with an electronic single particle excitation. As an alternative interpretation a low-energy vibrational excitation
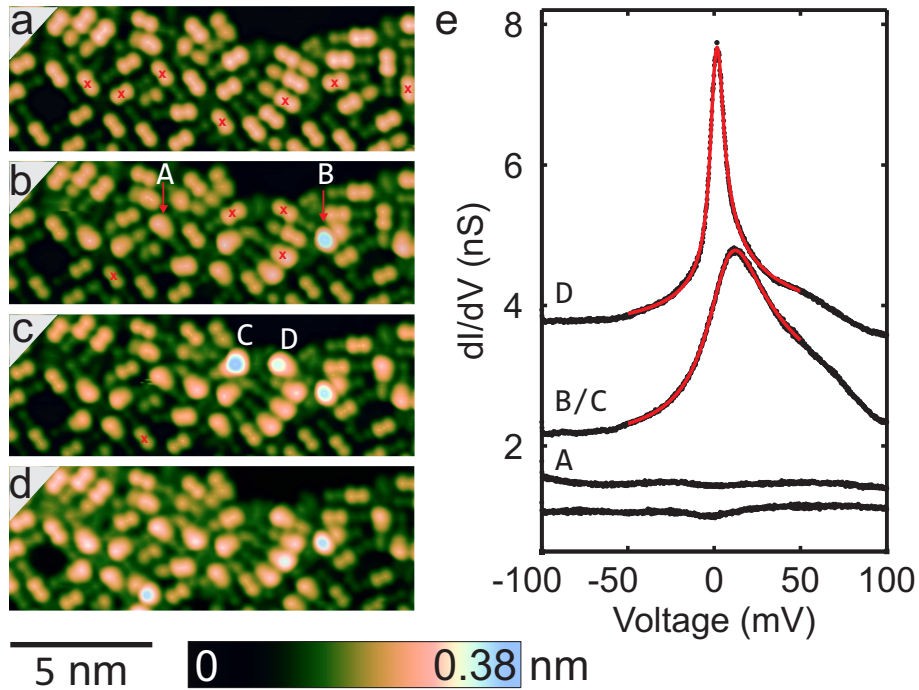
Figure 9.2: (a–d) STM images showing a sequence of switching events. The manipulations were effected at $V = -2.5$ V with disabled current-feedback. The positions of the applied pulses are marked with red crosses. Different states are marked with arrows. (e) dI/dV spectra recorded over the center of the tetra-cyclic rings of different molecular states. For clarity, the top three spectra are shifted vertically by 3, 1.5, and 0.5 nS, respectively. The data were recorded using a lock-in amplifier by adding a sinusoidal modulation of 2 mV$_{rms}$ at 985 Hz to the sample voltage. Before opening the current feedback, the STM was operated at $V = -100$ mV and $I = 100$ pA.

should be considered [245, 246]. The asymmetry of the lines, which is particularly obvious in states B and C, however, does not favor this scenario. We therefore attribute the resonance to a Kondo effect. This is a many-body effect in which a localized spin is screened by the conduction electrons of the substrate. It has been observed from various magnetic atoms and molecules on surfaces [38, 42, 103–107]. Organic radicals on surfaces were also shown to exhibit this effect [79, 235–237, 247]. The corresponding line-shape may be described by a Frota function [113, 114], which has recently been used to model the Kondo fingerprints of a range of systems [37, 115–117]. Using the generalized Frota function of Ref. [116], which allows for an asymmetry parameter, our experimental data is reproduced very well[1] (Figure 9.2e).

The Kondo effect requires the presence of a localized spin. Indeed, no such effect is observed from pristine cholesterol on Au(111) as expected for a closed-shell molecule. State A may tentatively be attributed to a geometrical isomer because its electronic structure is unchanged in dI/dV spectra[2]. We propose that states B–D are due to the formation of radical cation. The possibility of generating stable radical cations has indeed been reported for organic biomolecules such as retinoic acid [249], whereas the creation of an anion may dissociate the molecule through deprotonation [272]. A cationic state is also consistent with the experimental observation that these states are obtained upon electron transfer from the molecule to the tip at elevated bias voltage. It may be speculated that the extracted electron stems from the endocyclic double bond, similar to the case of retinoic acid [249]. At the low temperature of the experiment the cationic state may be stabilized by a concomitant change of the molecular geometry. A closely related mechanism has been reported from charged metal atoms on insulators [250–252].

Conclusion

In conclusion, single cholesterol molecules have been reversibly switched on a Au(111) substrate among several states, three of which carry a localized spin as revealed from scanning tunneling spectroscopy. The process is attributed to the creation of a radical cation which gives rise to a Kondo resonance. The multistability of the molecule with paramagnetic and diamagnetic states that may be controllably switched may make it a candidate for spintronic applications. It may also be interesting to look for spin effects in cholesterol in a biochemical environment.

---

[1]From the fits of Frota functions Kondo temperatures of ~ 22, ~ 125 K, and ~ 125 K are obtained for states D, B, and C, respectively. It should be noted that these values are not obvious to be the actual Kondo temperatures [79].

[2]Spectra over a wider voltage range ($-0.5 \ldots 0.5$ V, not shown) did not reveal significant spectroscopic differences between pristine molecules and state A.

Concluding Remarks

To summarize, several aspects of single-molecule junctions are presented in this thesis analyzing the geometry and chemical compositions of molecules along with their electronic structures. The results contribute significantly to the understanding of structural and electronic properties of single molecules.

Reversible switching between two isomers of a Fe(salten) complex has been achieved within single binuclear molecules. A disulfide bridge connecting the molecular subunits enables remote switching, whereas an ethyl link is found to be inactive. It is conceivable that our approach may be extended to implement basic logic functions within a single molecule.

Tetranuclear Co-grid complexes incorporating bis-terpyridine ligands were electrosprayed onto a Au(111) substrate. Complete fragmentation occurs leaving the ligands in four different conformations. The most abundant conformer exhibit an asymmetric form, which has not been observed before. The present results indicate that the fragmentation of coordination compounds during the deposition process allows for the surface trapping of high energy conformations of the ligand molecules at low temperatures.

Mn-porphyrin, a planar molecule, was studied on Au(111). Using a sharp feature at the Fermi energy, which results from a Kondo effect, it is shown that approximately 80 % of the voltage applied to the junction drops at the molecule-substrate spacing, when the central Mn atom is contacted with the STM tip. The result implies that simplistic assumptions—that in a supposedly symmetric single-molecule junction, the applied voltage drops equally on both molecule-electrode interfaces—may not always be valid.

Pentamers of *all-trans*-retinoic acid molecules have been prepared on the pristine Au(111) surface and a molecular monolayer. Cycles of hydrogen bonds between carboxylic acid moieties stabilize the pentamers. The linear shape and suitable molecular densities are crucial for pentamer formation. We speculate that related self-assembly of pentamers may be achieved on other weakly interacting surfaces. Moreover, these molecules on gold may be converted to a number of states that carry a localized spin. Based on ab-initio calculations and presumably related observations in liquid environments we propose that the molecule is converted to a radical cation. An interesting extension of the work will be to use arrays of related molecules to create arbitrary patterns of spins.

Finally, I revealed that single cholesterol molecules can be reversibly switched

on a Au(111) substrate among several spin-carrying states. The process is attributed to the creation of a radical cation. We hint that an electron is removed from the endocyclic double bond. It may be interesting to look for spin effects in cholesterol in a biochemical environment.

Although satisfactory conclusions have been made from each of the experiments, given the broad interest in molecular junctions and the novelty of the experimental results, a follow-up would be important to take the ideas forward for further developments. I propose to look further into a couple of projects. While the result presented in Chapter 5 demonstrating isomerization from binuclear organometallic complexes set out a foundation for molecules to be controlled through non-local perturbation, it seems natural to extend this approach to tune the spin states of molecules in a similar manner. Also, the applicability of the proposed mechanism could be investigated on insulating layers to access the importance of the substrates.

To extend upon the work undertaken on Mn-porphyrin, outlined in Chapter 4, I suggest to design experiments on disubstituted porphin, presuming that a change in Kondo temperature would occur at contact. This comparison may illustrate a trend and perhaps help us explaining molecular transport-junctions even in more detail.

List of Publications

Author's publications in peer-reviewed journals:

1) S. Karan, T. G. Gopakumar, H. Jacob, S. Meyer, F. Tuczek, and R. Berndt; Remotely Triggered Geometrical Isomerization of a Binuclear Complex, *J. Am. Chem. Soc.* **136**, 6163 (2014).

2) S. Karan, Y. Wang, R. Robles, N. Lorente, and R. Berndt; Surface-Supported Supramolecular Pentamers,
J. Am. Chem. Soc. **135**, 14004 (2013).

3) S. Karan, Chr. Hamann, H. Tang, A. R. Stefankiewicz, J.-M. Lehn, and R. Berndt; Surface Trapping and STM Observation of Conformational Isomers of a Bis(Terpyridine) Ligand from Metallosupramolecular Grids,
ChemPhysChem, **16**, 1370 (2015).

4) S. Karan, D. Jacob, M. Karolak, Chr. Hamann, Y. F. Wang, A. Weismann, A. I. Lichtenstein, and R. Berndt; Shifting the voltage drop in electron transport through a single molecule,
Phys. Rev. Lett. (accepted).

5) Chr. Hamann, R. Woltmann, I.-P. Hong, N. Hauptmann, S. Karan, and R. Berndt; Ultrahigh vacuum deposition of organic molecules by electrospray ionization,
Rev. Sci. Instrum. **82**, 033903 (2011).

6) C. Tank, S. Raman, S. Karan, S. Gosavi, N. P. Lalla, V. Sathe, R. Berndt, W. N. Gade, S. V. Bhoraskar, and V. L. Mathe; Antimicrobial activity of silica coated silicon nano-tubes (SCSNT) and silica coated silicon nano-particles (SCSNP) synthesized by gas phase condensation,
J. Mater Sci.: Mater Med. **24**, 1483 (2013).

7) S. Karan et al.; Spin manipulation by creating single-molecule radical cation,
Submitted.

8) S. Karan and R. Berndt; Generating Spins in Single Cholesterol Molecules on Gold,
Ready for submission.

Acknowledgement

Excitement of getting closer to the purpose certainly calls me to acknowledge those peoples who helped me along the way.

I was incredibly fortunate to be able to work with Prof. Dr. Richard Berndt, my thesis advisor. I can't thank him enough for his trust and guidance throughout the entire time. The contentment in working together and those endless discussions will probably be unforgettable. It was nice to have worked with you "Boss". Many thanks!

All my collaborators, especially Prof. Nicolás Lorente, Dr. Roberto Robles, Dr. David Jacob, Dr. Michael Karolak, Prof. Alexander I. Lichtenstein, Dr. Reinhard J. Maurer, Prof. Karsten Reuter, and Dr. Hao Tang are acknowledged for their support through theoretical work; Prof. Kai Wu and Prof. Yongfeng Wang are acknowledged for their assistance with additional experiments.

I thank all my other co-authors and the authors listed in the references.

I also thank several chemists, especially Prof. Felix Tuczek, Prof. Rainer Herges, and Prof. J.-M. Lehn who taught me the beauty of chemistry. I don't think I got it enough, but that doesn't take away their credit.

Dr. Markus Gruyters, Dr. Alexander Weismann and Dr. Manuel Gruber, many thanks to all three of you for the assistance and proofreading parts of this thesis.

I owe special thanks to all my colleagues, lab mates, and former coworkers for maintaining friendly atmosphere all the time; especially my office-mates for their helpful attitude.

A big thanks goes to Ms. Monika Seeger for her adroit help with routine paperwork.

The administrative and non-scientific stuff of CAU are acknowledged for making several necessary things available.

It can not be concluded without mentioning my parents who have done every possible thing to make me feel comfortable and secure all the years.

I will always cherish all those days spent in Kiel. Thanks to each and every one for adopting me as one of yours[3].

---

[3]Sujoy Karan, Institute of Experimental and Applied Physics, CAU Kiel

Curriculum Vitae

Name	Sujoy Karan
Nationality	Indian

Education

B.Sc. Physics with Honours, University of Calcutta, India.

M.Sc. Physics, University of Pune, India.

Ph.D. Christian-Albrechts-Universitt zu Kiel, Germany.

Past Research Experiences

A project on the dynamics of Atomic Force Microscopy (AFM) Cantilevers at the Department of Physics, University of Pune, India.

A project on the structure of Cs nucleus in Saha Institute of Nuclear Physics, Kolkata, India.

Teaching Experience

Worked as a principal teaching assistant at the Physics Laboratory for B.Sc. courses in University of Kiel.

Declaration

Herewith I declare in lieu of an oath that the present thesis entitled "Exploiting Spin Manipulation and Stereo-Isomerization in Molecular Switches" is an account of my own work carried out consulting my scientific advisor together with the listed material only. This work or any part thereof has not been submitted to any other university or institution in the context of an examination procedure. Earlier attempts to attain a doctorate degree were not made.

Hiermit erkläre ich an Eides Statt, dass ich diese Arbeit selbständig unter der Beratung meiner wissenschaftlichen Lehrer und nur mit den angegebenen Hilfsmitteln erstellt habe. Diese Arbeit wurde weder ganz noch in Teilen an anderer Stelle im Rahmen eines Prfungsverfahrens vorgelegt. Frühere Promotionsversuche wurden von mir nicht vorgenommen.

(Sujoy Karan)

Kiel,   .2015

Bibliography

[1] M. Ratner, *Nature Nanotech.* **8**, 378 (2013).

[2] B. Mann, and H. Kuhn, *J. Appl. Phys.* **42**, 4398 (1971).

[3] A. Aviram, and M. A. Ratner, *Chem. Phys. Lett.* **29**, 277 (1974).

[4] G. Binnig and H. Rohrer, *Helv. Phys. Acta* **55**, 726 (1982).

[5] G. Binnig, H. Rohrer, C. Gerber, and E. Weibel, *Appl. Phys. Lett.* **40**, 178 (1982).

[6] G. Binnig, H. Rohrer, C. Gerber, and E. Weibel, *Phys. Rev. Lett.* **49**, 57 (1982).

[7] J. K. Gimzewski, E. Stoll, and R. R. Schlittler, *Surf. Sci.* **181**, 267 (1987).

[8] A. Nitzan, and M. A. Ratner, *Science* **300**, 1384 (2003).

[9] N. J. Tao, *Nature Nanotech.* **1**, 173 (2006).

[10] H. Choi and C. C. M. Mody, *Soc. Stud. Sci.* **39**, 11 (2009).

[11] G. Schull, T. Frederiksen, A. Arnau, D. Sanchez-Portal, and R. Berndt, *Nature Nanotech.* **6**, 23 (2011).

[12] S. A. Wolf, D. D. Awschalom, R. A. Buhrman, J. M. Daughton, S. von Molnár, M. L. Roukes, A. Y. Chtchelkanova, and D. M. Treger, *Science* **294**, 1488 (2001).

[13] A. R. Rocha, V. M. García-suárez, S. W. Bailey, C. J. Lambert, J. Ferrer, and S. Sanvito, *Nature Mater.* **4**, 335 (2005).

[14] L. Bogani and W. Wernsdorfer, *Nature Mater.* **7**, 179 (2008).

[15] C. Chappert, A. Fert, and F. N. Van Dau, *Nature Mater.* **6**, 813 (2007).

[16] D. D. Awshalom and M. M. Flatté, *Nature Phys.* **3**, 153 (2007).

[17] S. Karan, T. G. Gopakumar, H. Jacob, S. Meyer, F. Tuczek, and R. Berndt, *J. Am. Chem. Soc.* **136**, 6163 (2014).

[18] S. V. Aradhya, and L. Venkataraman, *Nature Nanotech.* **8**, 399 (2013).

[19] J. K. Gimzewski and C. Joachim, *Science* **283**, 1683 (1999).

[20] F. Moresco, G. Meyer, K.-H. Rieder, H. Tang, A. Gourdon, C. Joachim, *Phys. Rev. Lett.* **86**, 672 (2001).

[21] X.H. Qiu, G.V. Nazin, W. Ho, *Phys. Rev. Lett.* **93**, 196806-1 (2004).

[22] M. Alemani, M. V. Peters, S. Hecht, K.-H. Rieder, F. Moresco, and L. Grill, *J. Am. Chem. Soc.* **128**, 14446 (2006).

[23] B.-Y. Choi, S. J. Kahng, S. Kim, H. Kim, H. W. Kim, Y. J. Song, J. Ihm, and Y. Kuk, *Phys. Rev. Lett.* **96**, 156106 (2006).

[24] J. Henzl, M. Mehlhorn, H. Gawronski, K.-H. Rieder, and K. Morgenstern, *Angew. Chem. Int. Ed.* **45**, 603 (2006).

[25] M. E. Garah, B. Baris, V. Luzet, F. Palmino, and F. Chérioux, *ChemPhysChem* **11**, 2568 (2010).

[26] M. J. Comstock, N. Levy, A. Kirakosian, J. Cho, F. Lauterwasser, J. H. Harvey, D. A. Strubbe, J. M. J. Fréchet, D. Trauner, S. G. Louie, and M. F. Crommie, *Phys. Rev. Lett.* **99**, 038301 (2007).

[27] A. S. Kumar, T. Ye, T. Takami, B.-C. Yu, A. K. Flatt, J. M. Tour, and P. S. Weiss, *Nano Lett.* **8**, 1644 (2008).

[28] M. Alemani, S. Selvanathan, F. Ample, M.V. Peters, K.-H. Rieder, F. Moresco, C. Joachim, S. Hecht, and L. Grill, *J. Chem. Phys. C* **112**, 10509 (2008).

[29] V. Iancu and S.-W. Hla, *Proc. Natl. Acad. Sci. U.S.A.* **103**, 13718 (2006).

[30] P. Liljeroth, J. Repp, and G. Meyer, *Science* **317**, 1203 (2007).

[31] W. Auwärter, K. Seufert, F. Bischoff, D. Ecija, S. Vijayaraghavan, S. Joshi, F. Klappenberger, N. Samudrala, and J. V. Barth, *Nature Nanotech.* **7**, 41 (2012).

[32] S. Weigelt, C. Busse, L. Petersen, E. Rauls, B. Hammer, K. V. Gothelf, F. Besenbacher, and T. R.Linderoth, *Nature Mater.* **5**, 112 (2006).

[33] A. Zhao, Q. Li, L. Chen, H. Xiang, W. Wang, S. Pan, B. Wang, X. Xiao, J. Yang, J. G. Hou, Q. Zhu, *Science* **309**, 1542 (2005).

[34] V. Iancu, A. Deshpande, and S.-W. Hla, *Nano Lett.* **6**, 820 (2006).

[35] P. Wahl, L. Diekhöner, G. Wittich, L. Vitali, M. A. Schneider, and K. Kern, *Phys. Rev. Lett.* **95**, 166601 (2005).

[36] V. Iancu, A. Deshpande, and S.-W. Hla, *Phys. Rev. Lett.* **97**, 266603 (2006).

[37] Y.-S. Fu, S.-H. Ji, X. Chen, X.-C. Ma, R. Wu, C.-C. Wang, W.-H. Duan, X.-H. Qiu, B. Sun, P. Zhang, J.-F. Jia, and Q.-K. Xue, *Phys. Rev. Lett.* **99**, 256601 (2007).

[38] E. Minamitani, N. Tsukahara, D. Matsunaka, Y. Kim, N. Takagi, and M. Kawai, *Phys. Rev. Lett.* **109**, 086602 (2012).

[39] A. Stróżecka, M. Soriano, J. I. Pascual, and J. J. Palacios, *Phys. Rev. Lett.* **109**, 147202 (2012).

[40] C. Wäckerlin, D. Chylarecka, A. Kleibert, K. Müller, C. Iacovita, F. Nolting, T. A. Jung, and N. Ballav, *Nat. Commun.* **1**, 61 (2010).

[41] L. Liu, K. Yang, Y. Jiang, B. Song, W. Xiao, L. Li, H. Zhou, Y. Wang, S. Du, M. Ouyang, W. A. Hofer, A. H. Castro Neto, and H.-J. Gao, *Sci. Rep.* **3**, 1210 (2013).

[42] T. Komeda, H. Isshiki, J. Liu, Y.-F. Zhang, N. Lorente, K. Katoh, B. K. Breedlove, and M. Yamashita, *Nat. Commun.* **2**, 217 (2011).

[43] R. Robles, N. Lorente, H. Isshiki, J. Liu, K. Katoh, B. K. Breedlove, M. Yamashita, and T. Komeda, *Nano Lett.* **12**, 3609 (2012).

[44] C. Krull, R. Robles, A. Mugarza, and P. Gambardella, *Nature Mater.* **12**, 337 (2013).

[45] T. Miyamachi, M. Gruber, V. Davesne, M. Bowen, S. Boukari, L. Joly, F. Scheurer, G. Rogez, T. K. Yamada, P. Ohresser, E. Beaurepaire, and W. Wulfhekel, *Nat. Commun.* **3**, 938 (2012).

[46] T. G. Gopakumar, F. Matino, H. Naggert, A. Bannwarth, F. Tuczek, and R. Berndt, *Angew. Chem. Int. Ed.* **51**, 6262 (2012).

[47] J. M. van Ruitenbeek, A. Alvarez, I. Piñeyro, C. Grahmann, P. Joyez, M. H. Devoret, D. Esteve, and C. Urbina, *Rev. Sci. Instrum.* **67**, 108 (1996).

[48] M. A. Reed, C. Zhou, C. J. Muller, T. P. Burgin, and J. M. Tour, *Science* **278**, 252 (1997).

[49] C. Kergueris, J.-P. Bourgoin, S. Palacin, D. Esteve, C. Urbina, M. Magoga and C. Joachim, *Phys. Rev. B* **59**, 12505 (1999).

[50] F. Chen, J. He, C. Nuckolls, T. Roberts, J. E. Klare, and S. Lindsay, *Nano Lett.* **5**, 503 (2005).

[51] E. Lörtscher, J. W. Ciszek, J. Tour, and H. Riel, *Small* **2**, 973 (2006).

[52] S. Y. Quek, M. Kamenetska, M. L. Steigerwald, H. J. Choi, S. G. Louie, M. S. Hybertsen, J. B. Neaton, and L. Venkataraman, *Nature Nanotech.* **4**, 230 (2009).

[53] I. Díez-Pérez, J. Hihath, Y. Lee, L. Yu, L. Adamska, M. A. Kozhushner, I. I. Oleynik, and N. Tao, *Nature Chem.* **1**, 635 (2009).

[54] R. H. M. Smit, Y. Noat, C. Untiedt, N. D. Lang, M. C. van Hemert, and J. M. van Ruitenbeek, *Nature* **419**, 906 (2002).

[55] B. Xu and N. J. Tao, *Science* **301**, 1221 (2003).

[56] L. Venkataraman, J. E. Klare, C. Nuckolls, M. S. Hybertsen, and M. L. Steigerwald, *Nature* **442**, 904 (2006).

[57] M. Taniguchi, M. Tsutsui, R. Mogi, T. Sugawara, Y. Tsuji, K. Yoshizawa, and T. Kawai, *J. Am. Chem. Soc.* **133**, 11426 (2011).

[58] J. M Hamill, K. Wang, and B. Xu, *Reports in Electrochemistry* **4**, 1 (2014).

[59] F. D. Novaes, M. Cobian, A. García, P. Ordejón, H. Ueba, and N. Lorente, arXiv:1101.3714 (2011).

[60] S. Ulstrup, T. Frederiksen, and M. Brandbyge, Phys. Rev. B **86**, 245417 (2012).

[61] D. L. Kepert, *Prog. Inorg. Chem.* **23**, 1 (1977).

[62] C. J. Chen (edited by M. Lapp), *Introduction to scanning tunneling microscopy*, Oxford University Press: New York (1993).

[63] R. Wiesendanger, *Scanning probe microscopy and spectroscopy - Methods and applications*, Cambridge University Press: Cambridge (1994).

[64] J. Tersoff and D. R. Hamann, *Phys. Rev. Lett.* **50**, 1998 (1983).

[65] J. Tersoff and D. R. Hamann, *Phys. Rev. B* **31**, 805 (1985).

[66] J. Bardeen, *Phys. Rev. Lett.* **6**, 57 (1961).

[67] B. Voigtländer, V. Scheuch, and H. P. Bonzel, S. Heinze, and S. Blügel, *Phys. Rev. B* **55**, R13444 (1997).

[68] V. P. LaBella, H. Yang, D. W. Bullock, P. M. Thibado, P. Kratzer, and M. Scheffler, *Phys. Rev. Lett.* **83**, 2989 (1999).

[69] S. Heinze, S. Blügel, R. Pascal, M. Bode, and R. Wiesendanger, *Phys. Rev. B* **58**, 16432 (1998).

[70] C. J. Chen, *Phys. Rev. Lett.* **65**, 448 (1990).

[71] A. Selloni, P. Carnevali, E. Tosatti, and C. D. Chen, *Phys. Rev. B* **31**, 2602 (1985).

[72] J. Li, W.-D. Schneider, and R. Berndt, *Phys. Rev. B* **56**, 7656 (1997).

[73] J. A. Stroscio, R. M. Feenstra, and A. P. Fein, *Phys. Rev. Lett.* **57**, 2579 (1986).

[74] N. D. Lang, *Phys. Rev. B* **34**, 5947 (1986).

[75] A. L. Vázquez de Parga, O. S. Hernán, R. Miranda, A. L. Yeyati, N. Mingo, A. Martin-Rodero, and F. Flores, *Phys. Rev. Lett.* **80**, 357 (1998).

[76] W. Chen, V. Madhavan, T. Jamneala, and M. F. Crommie, *Phys. Rev. Lett.* **80**, 1469 (1998).

[77] F. Reinert, G. Nicolay, S. Schmidt, D. Ehm, and S. Hüfner, *Phys. Rev. B* **63**, 115415 (2001).

[78] J. Klein, A. Léger, M. Belin, D. Défourneau, and M. J. L. Sangster, *Phys. Rev. B* **7**, 2336 (1973).

[79] Y.-h. Zhang, S. Kahle, T. Herden, C. Stroh, M. Mayor, U. Schlickum, M. Ternes, P. Wahl, and K. Kern, *Nat. Commun.* **4**, 2110 (2013).

[80] A. Burtzlaff, A. Weismann, M. Brandbyge, and R. Berndt, *Phys. Rev. Lett.* **114**, 016602 (2015).

[81] N. D. Lang, *Phys. Rev. B* **37**, 10395 (1988).

[82] N. Agräit, A. L. Yeyati, and J. M. van Ruitenbeek, *Phys. Rep.* **377**, 81 (2003).

[83] R. Landauer, *IBM J. Res. Dev.* **1**, 223 (1957).

[84] R. Landauer, *Philos. Mag.* **21**, 683 (1970).

[85] M. Büttiker, Y. Imry, R. Landauer, and S. Pinhas, *Phys. Rev. B* **31**, 6207 (1985).

[86] P. W. Anderson, D. J. Thouiess, E. Abraharns, and D. S. Fisher, *Phys. Rev. B* **22**, 3519 (1980).

[87] M. Büttiker, *Phys. Rev. Lett.* **57**, 1761 (1986).

[88] S. Datta, M. Cahay, and M. McLennan, *Phys. Rev. B* **36**, 5655 (1987).

[89] J. Fenn, M. Mann, C. Meng, S. Wong, and C. Whitehouse, *Science* **246**, 64 (1989).

[90] R. D. Smith, J. A. Loo, C. G. Edmonds, C. J. Barinaga, and H. R. Udseth, *Anal. Chem.* **62**, 882 (1990).

[91] G. Taylor, *Proceedings of the Royal Society of London. Series A, Mathematical and Physical Sciences* **280**, 383 (1964).

[92] L. Rayleigh, *Philosophical Magazine Series 5* **14**, 184 (1882).

[93] D. C. Taflin, T. L. Ward, and E. J. Davis, *Langmuir* **5**, 376 (1989).

[94] D. Duft, T. Achtzehn, R. Müller, B. A. Huber, and T. Leisner, *Nature* **421**, 128 (2003).

[95] Z. Ouyang, Z. Takáts, T. A. Blake, B. Gologan, A. J. Guymon, J. M. Wiseman, J. C. Oliver, V. J. Davisson, and R. G. Cooks, *Science* **301**, 1351 (2003).

[96] S. Rauschenbach, F. L. Stadler, E. Lunedei, N. Malinowski, S. Koltsov, Gi. Costantini, and K. Kern, *Small* **2**, 540 (2006).

[97] J. C. Swarbrick, J. B. Taylor, and J. N. O'Shea, *Appl. Surf. Sci.* **252**, 5622 (2006).

[98] O. Hadjar, P. Wang, J. H. Futrell, Y. Dessiaterik, Z. Zhu, J. P. Cowin, M. J. Iedema, and J. Laskin, *Anal. Chem.* **79**, 6566 (2007).

[99] Chr. Hamann, R. Woltmann, I.-P. Hong, N. Hauptmann, S. Karan, and R. Berndt, *Rev. Sci. Instrum.* **82**, 033903 (2011).

[100] J. W. Farley, *Rev. Sci. Instrum.* **56**, 1834 (1985).

[101] P. R. Mahaffy and K. Lai, *J. Vac. Sci. Technol. A* **8**, 3244 (1990).

[102] Chr. Hamann, *Ph.D. Thesis, CAU Kiel* (2011).

[103] J. Li, W.-D. Schneider, R. Berndt, and B. Delley, *Phys. Rev. Lett.* **80**, 2893 (1998).

[104] V. Madhavan, W. Chen, T. Jamneala, M. F. Crommie, and N. S. Wingreen, *Science* **280**, 567 (1998).

[105] U. G. E. Perera, H. J. Kulik, V. Iancu, L. G. G. V. Dias da Silva, S. E. Ulloa, N. Marzari, and S.-W. Hla, *Phys. Rev. Lett.* **105**, 106601 (2010).

[106] A. Mugarza, R. Robles, C. Krull, R. Korytár, N. Lorente, and P. Gambardella, *Phys. Rev. B* **85**, 155437 (2012).

[107] A. DiLullo, S.-H. Chang, N. Baadji, K. Clark, J.-P. Klöckner, M.-H. Prosenc, S. Sanvito, R. Wiesendanger, G. Hoffmann, and S.-W. Hla, *Nano Lett.* **12**, 3174 (2012).

[108] A. C. Hewson, *The Kondo Problem to Heavy Fermions*, Cambridge University Press: Cambridge (1993).

[109] M. Ternes, A. J. Heinrich, and W.-D. Schneider, *J. Phys.: Condens. Matter* **21**, 053001 (2009).

[110] K. Nagaoka, T. Jamneala, M. Grobis, and M. F. Crommie, *Phys. Rev. Lett.* **88**, 077205 (2002).

[111] M. Ternes, A. J. Heinrich, and W.-D. Schneider, *J. Phys.: Condens. Matter* **21**, 053001 (2009).

[112] U. Fano, *Phys. Rev.* **124**, 1866 (1961).

[113] H. O. Frota and L. N. Oliveira, *Phys. Rev. B* **33**, 7871 (1986).

[114] H. O. Frota, *Phys. Rev. B* **45**, 1096 (1992).

[115] H. Prüser, M. Wenderoth, P. E. Dargel, A. Weismann, R. Peters, T. Pruschke, and R. G. Ulbrich, *Nature Phys.* **7**, 203 (2011).

[116] H. Prüser, M. Wenderoth, A. Weismann, and R. G. Ulbrich, *Phys. Rev. Lett.* **108**, 166604 (2012).

[117] D.-J. Choi, M. V. Rastei, P. Simon, and L. Limot, *Phys. Rev. Lett.* **108**, 266803 (2012).

[118] R. Žitko, *Phys. Rev. B* **84**, 195116 (2011).

[119] R. Žitko and T. Pruschke, *Phys. Rev. B* **79**, 085106 (2009).

[120] V. L. Campo, Jr. and L. N. Oliveira, *Phys. Rev. B* **68**, 035337 (2003).

[121] M. North, *Principles and Applications of Stereochemistry*, CRC Press: United Kingdom (1998).

[122] IUPAC, Compendium of Chemical Terminology, 2nd ed. (the "Gold Book"), doi:10.1351/goldbook.T06406.

[123] G. P. Moss, IUPAC-IUB Joint Commission on Biochemical Nomenclature (JCBN), http://www.chem.qmul.ac.uk/iupac/misc/pnuc1.html

[124] W. Klyne and V. Prelog, *Experientia* **16**, 521 (1960).

[125] M. S. Newman, *J. Chem. Educ.* **32**, 344 (1955).

[126] Ch. Wöll, S. Chiang, R. J. Wilson, and P. H. Lippel, *Phys. Rev. B* **39**, 7988 (1989).

[127] F. Reinert and G. Nicolay, *Appl. Phys. A* **78**, 817 (2004).

[128] S. Narasimhan and D. Vanderbilt, *Phys. Rev. Lett.* **69**, 1564 (1992).

[129] K. Besocke, *Surf. Sci.* **181**, 145 (1987).

[130] J. Frohn, J. F.Wolf, K. Besocke, and M. Teske, *Rev. Sci. Instrum.* **60**, 1200 (1989).

[131] S. Karan, D. Jacob, M. Karolak, C. Hamann, Y. Wang, A. Weismann, A. I. Lichtenstein, and Richard Berndt, *Phys. Rev. Lett.* (accepted).

[132] V. Meded, A. Bagrets, K. Fink, R. Chandrasekar, M. Ruben, F. Evers, A. Bernand-Mantel, J. S. Seldenthuis, A. Beukman, and H. S. J. van der Zant, Phys. Rev. B **83**, 245415 (2011).

[133] J. J. Parks, A. R. Champagne, T. A. Costi, W. W. Shum, A. N. Pasupathy, E. Neuscamman, S. Flores-Torres, P. S. Cornaglia, A. A. Aligia, C. A. Balseiro, et al., Science **328**, 1370 (2010).

[134] T. G. Gopakumar, H. Tang, J. Morillo, and R. Berndt, J. Am. Chem. Soc. **134**, 11844 (2012).

[135] N. Néel, J. Kröger, L. Limot, K. Palotas, W. A. Hofer, and R. Berndt, Phys. Rev. Lett. **98**, 016801 (2007).

[136] N. Néel, J. Kröger, and R. Berndt, Phys. Rev. B **82**, 233401 (2010).

[137] J. Bork, Y. Zhang, L. Diekhner, L. Borda, P. Simon, J. Kroha, P. Wahl, and K. Kern, Nature Phys. **7**, 901 (2011).

[138] D. M. Eigler, C. P. Lutz, and W. E. Rudge, Nature **352**, 600 (1991).

[139] G. Schull, T. Frederiksen, M. Brandbyge, and R. Berndt, Phys. Rev. Lett. **103**, 206803 (2009).

[140] G. V. Nazin, S. W. Wu, and W. Ho, Proc. Natl. Acad. Sci. U.S.A. **102**, 8832 (2005).

[141] B. Li, C. Zeng, J. Zhao, J. Yang, J. G. Hou, and Q. Zhu, J. Chem. Phys. **124**, 064709 (2006).

[142] B. Warner, F. E. Hallak, H. Prüser, J. Sharp, M. Persson, A. J. Fisher, and C. F. Hirjibehedin, *Nature Nanotech.* **10**, 259 (2015).

[143] S. Datta, W. Tian, S. Hong, R. Reifenberger, J. I. Henderson, and C. P. Kubiak, Phys. Rev. Lett. **79**, 2530 (1997).

[144] F. Matino, G. Schull, F. Köhler, S. Gabutti, M. Mayor, and R. Berndt, Proc. Natl. Acad. Sci. U.S.A. **108**, 961 (2011).

[145] G. C. Liang, A. W. Ghosh, M. Paulsson, and S. Datta, *Phys. Rev. B* **69**, 115302 (2004).

[146] K. H. Bevan, D. Kienle, H. Guo, and S. Datta, *Phys. Rev. B* **78**, 035303 (2008).

[147] J. Taylor, M. Brandbyge, and K. Stokbro, Phys. Rev. Lett. **89**, 138301 (2002).

[148] Q. Li, S. Yamazaki, T. Eguchi, H. Kim, S.-J. Kahng, J. F. Jia, Q. K. Xue, and Y. Hasegawa, Phys. Rev. B **80**, 115431 (2009).

[149] D. Jacob, K. Haule, and G. Kotliar, Phys. Rev. Lett. **103**, 016803 (2009).

[150] M. Karolak, D. Jacob, and A. I. Lichtenstein, Phys. Rev. Lett. **107**, 146604 (2011).

[151] D. Jacob, M. Soriano, and J. J. Palacios, Phys. Rev. B **88**, 134417 (2013).

[152] G. Kresse and J. Hafner, J. Phys.: Condens. Matter **6**, 8245 (1994).

[153] G. Kresse and D. Joubert, Phys. Rev. B **59**, 1758 (1999).

[154] J. P. Perdew, K. Burke, and M. Ernzerhof, Phys. Rev. Lett. **77**, 3865 (1996).

[155] S. Grimme, J. Comput. Chem. **27**, 1787 (2006).

[156] D. Jacob and J. J. Palacios, J. Chem. Phys. **134**, 044118 (2011).

[157] J. Kügel, M. Karolak, J. Senkpiel, P.-J. Hsu, G. Sangiovanni, and M. Bode, Nano Lett. **14**, 3895 (2014).

[158] K. Haule, S. Kirchner, J. Kroha, and P. Wölfle, Phys. Rev. B **64**, 155111 (2001).

[159] R. N. Silver, J. E. Gubernatis, D. S. Sivia, and M. Jarrell, Phys. Rev. Lett. **65**, 496 (1990).

[160] B. Horvatić and V. Zlatić, phys. stat. sol. (b) **99**, 251 (1980).

[161] S. W. Wu, G. V. Nazin, X. Chen, X. H. Qiu, and W. Ho, Phys. Rev. Lett. **93**, 236802 (2004).

[162] M. T. Czyżyk and G. A. Sawatzky, Phys. Rev. B **49**, 14211 (1994).

[163] S. Weigelt, C. Busse, L. Petersen, E. Rauls, B. Hammer, K. V. Gothelf, F. Besenbacher, and T. R. Linderoth, *Nature Mater.* **5**, 112 (2006).

[164] T. G. Gopakumar, F. Müller, and M. Hietschold, *J. Phys. Chem. B* **110**, 6051 (2006).

[165] G. Pace, V. Ferri, C. Grave, M. Elbing, C. von Hänisch, M. Zharnikov, M. Mayor, M. A. Rampi, and P. Samori, *Proc. Natl. Acad. Sci. U.S.A.* **104**, 9937 (2007).

[166] S. J. van der Molen, J. Liao, T. Kudernac, J. S. Agustsson, L. Bernard, M. Calame, B. J. van Wees, B. L. Feringa, and C. Schönenberger, *Nano Lett.* **9**, 76 (2009).

[167] A. Saedi, A. van Houselt, R. van Gastel, B. Poelsema, and H. J. W. Zandvliet, *Nano Lett.* **9**, 1733 (2009).

[168] M. J. Comstock, D. A. Strubbe, L. Berbil-Bautista, N. Levy, J. Cho, D. Poulsen, J. M. J. Fréchet, S. G. Louie, and M. F. Crommie, *Phys. Rev. Lett.* **104**, 178301 (2010).

[169] K. Morgenstern, *Prog. Surf. Sci.* **86**, 115 (2011).

[170] M. Lastapis, M. Martin, D. Riedel, L. Hellner, G. Comtet, and G. Dujardin, *Science* **308**, 1000 (2005).

[171] N. Wintjes, D. Bonifazi, F. Cheng, A. Kiebele, M. Stöhr, Th. Jung, H. Spillmann, and F. Diederich, *Angew. Chem.* **119**, 4167 (2007).

[172] Y. F. Wang, J. Kröger, R. Berndt, and W. A. Hofer, *J. Am. Chem. Soc.* **131**, 3639 (2009).

[173] Electron-induced remote switching via electronic surface states has been reported: P. Maksymovych, D. B. Dougherty, X.-Y. Zhu, and J. T. Yates, Jr., *Phys. Rev. Lett.* **99**, 016101 (2007). Also see Ref. [46]. Electric-field-induced changes over nanometer distances have been reported in, *e.g.*, Ref. [22]. However, single molecules were not addressed.

[174] A. J. Heinrich, C. P. Lutz, J. A. Gupta, and D. M. Eigler, *Science* **298**, 1381 (2002).

[175] H. Jacob, K. Kathirvel, F. Petersen, T. Strunskus, A. Bannwarth, S. Meyer, and F. Tuczek, *Langmuir* **29**, 8534 (2013).

[176] N. Matsumoto, S. Ohta, C. Yoshimura, A. Ohyoshi, S. Kohata, H. Okawa, and Y. Maeda, *J. Chem. Soc. Dalton Trans.* 2575 (1985).

[177] C. R. Mayer, G. Cucchiaro, J. Jullien, F. Dumur, J. Marrot, E. Dumas, and F. Sécheresse, *Eur. J. Inorg. Chem.* 3614 (2008).

[178] I. Horcas, R. Fernandez, J. M. Gomez-Rodriguez, J. Colchero, J. Gomez-Herrero, and A. M. Baro, *Rev. Sci. Instrum.* **78**, 013705 (2007).

[179] M. J. Frisch *et al.*, *Gaussian09, Revision A.02*, Gaussian, Inc.

[180] A. D. J. Becke, *Chem. Phys.* **98**, 5648 (1993).

[181] W. Hieringer, K. Flechtner, A. Kretschmann, K. Seufert, W. Auwärter, J. V. Barth, A. Görling, H.-P. Steinrück, and J. M. Gottfried, *J. Am. Chem. Soc.* **133**, 6206 (2011).

[182] S. Karan, C. Hamann, H. Tang, A. R. Stefankiewicz, J.-M. Lehn, and R. Berndt, *ChemPhysChem* **16**, 1370 (2015).
As there was an active collaboration, a part of this data was presented in [102]).

[183] M. Ruben, J. Rojo, F. J. Romero-Salguero, L. H. Uppadine, J.-M. Lehn, *Angew. Chem. Int. Ed.* **43**, 3644 (2004).

[184] M. Ruben, J.-M. Lehn, and P. Müller, *Chem. Soc. Rev.* **35**, 1056 (2006).

[185] K. Petukhov, M. S. Alam, H. Rupp, S. Stromsdorfer, P. Muller, A. Scheurer, R. W. Saalfrank, J. Kortus, A. Postnikov, M. Ruben, L. K. Thompson, and J.-M. Lehn, *Coord. Chem. Rev.* **253**, 2387 (2009).

[186] M. S. Alam, S. Strömsdörfer, V. Dremov, P. Müller, J. Kortus, M. Ruben, and J.-M. Lehn, *Angew. Chem. Int. Ed.* **44**, 7896 (2005).

[187] G. Pace, A. Stefankiewicz, J. Harrowfield, J.-M. Lehn, and P. Samori, *ChemPhysChem* **10**, 699 (2009).

[188] T. Matsumoto, G. N. Newton, T. Shiga, S. Hayami, Y. Matsui, H. Okamoto, R. Kumai, Y. Murakami, and H. Oshio, *Nat. Commun.* **5**, 3865 (2013).

[189] B. Schneider, S. Demeshko, S. Neudeck, S. Dechert, and F. Meyer, *Inorg. Chem.* **52**, 13230 (2013).

[190] O. Waldmann, J. Hassmann, P. Müller, G. S. Hanan, D. Volkmer, U. S. Schubert, and J.-M. Lehn, *Phys. Rev. Lett.* **78**, 3390 (1997).

[191] E. A. Osorio, M. Ruben, J. S. Seldenthuis, J.-M. Lehn, and H. S. J. van der Zant, *Small* **6**, 174 (2010).

[192] G. S. Hanan, J.-M. Lehn, N. Kyritsakas, and J. Fischer, *J. Chem. Soc. Chem. Commun.* **7**, 765 (1995).

[193] G. S. Hanan, U. S. Schubert, D. Volkmer, E. Riviere, J.-M. Lehn, N. Kyritsakas, and J. Fischer, *Can. J. Chem.* **75**, 169 (1997).

[194] D. M. Bassani, J.-M. Lehn, G. Baum, and D. Fenske, *Angew. Chem. Int. Ed. Engl.* **36**, 1845 (1997).

[195] M. Ohkita, J.-M. Lehn, G. Baum, and D. Fenske, *Chem. Eur. J.* **5**, 3471 (1999).

[196] J. Ramírez, A.-M. Stadler, J. M. Harrowfield, L. Brelot, J. Huuskonen, K. Rissanen, L. Allouche, and J.-M. Lehn, *Z. Anorg. Allg. Chem.* **633**, 2435 (2007).

[197] S. T. Howard, *J. Am. Chem. Soc.* **118**, 10269 (1996).

[198] V. Madhavan, W. Chen, T. Jamneala, M. F. Crommie, and N. S. Wingreen, *Phys. Rev. B.* **64**, 165412 (2001).

[199] U. Ziener, J.-M. Lehn, A. Mourran, and M. Möller, *Chem. Eur. J.* **8**, 951 (2002).

[200] K.-H. Ernst, *Phys. Status Solidi B* **249**, 2057 (2012).

[201] S. Karan, Y. F. Wang, R. Robles, N. Lorente, and R. Berndt, *J. Am. Chem. Soc.* **135**, 14004 (2013).

[202] J. Rojo, F. J. Romero-Salguero, J.-M. Lehn, G. Baum, D. Fenske, *Eur. J. Inorg. Chem.* 1421 (1999).

[203] J. J. P. Stewart, *MOPAC***2012**, Stewart Computational Chemistry, Colorado Springs, CO, USA, HTTP://OpenMOPAC.net.

[204] J. J. P. Stewart, *J. Mol. Model.* **13**, 1173 (2007).

[205] M. J. Korth, *Chem. Theory Comput.* **6**, 3808 (2010).

[206] J. J. P. Stewart, *J. Mol. Model.* **19**, 1 (2013).

[207] G. Kresse and J. Hafner, *Phys. Rev. B* **47**, 558 (1993).

[208] G. Kresse and J. Furthmüller, *Phys. Rev. B* **54**, 11169 (1996).

[209] E. Blöchl, *Phys. Rev. B* **50**, 17953 (1994).

[210] J. P. Perdew, K. Burke, and M. Ernzerhof, *Phys. Rev. Lett.* **78**, 1396 (1997).

[211] J. Cerdá, M. A. Van Hove, P. Sautet, and M. Salmeron, *Phys. Rev. B* **56**, 15885 (1997).

[212] J. Cerdá and F. Soria, *Phys. Rev. B* **61**, 7965 (2000).

[213] (a) L. Bartels, *Nature Chem.* **2**, 87 (2010). (b) J. V. Barth, *Annu. Rev. Phys. Chem.* **58**, 375 (2007).

[214] (a) G. Pawin, K. L. Wong, K.-Y. Kwon, and L. Bartels, *Science* **313**, 961 (2006). (b) Y. Ye, W. Sun, Y. Wang, X. Shao, X. Xu, F. Cheng, J. Li, and K. Wu, *J. Phys. Chem. C* **111**, 10138 (2007). (c) R. Otero, M. Lukas, R. E. A. Kelly, W. Xu, E. Lægsgaard, I. Stensgaard, L. N. Kantorovich, and F. Besenbacher, *Science* **319**, 312 (2008). (d) S. Griessl, M. Lackinger, M. Edelwirth, M. Hietschold, and W. M. Heckl, *Single Mol.* **3**, 25 (2002). (e) M. Stöhr, M. Wahl, C. H. Galka, T. Riehm, T. A. Jung, and L. H. Gade, *Angew. Chem., Int. Ed.* **44**, 7394 (2005). (f) S. De Feyter and F. C. De Schryver, *Chem. Soc. Rev.* **32**, 139 (2003).

[215] (a) A. Langner, S. L. Tait, N. Lin, C. Rajadurai, M. Ruben, A. Langner, and K. Kern, *Proc. Natl. Acad. Sci. U.S.A.* **104**, 17927 (2007). (b) T. Lin, X. S. Shang, J. Adisoejoso, P. N. Liu, and N. Lin, *J. Am. Chem. Soc.* **135**, 3576 (2013). (c) Z. Shi and N. Lin, *J. Am. Chem. Soc.* **131**, 5376 (2009).

[216] X. Qiu, C. Wang, Q. Zeng, B. Xu, S. Yin, H. Wang, S. Xu, and C. Bai, *J. Am. Chem. Soc.* **122**, 5550 (2000).

[217] (a) M. Böhringer, W.-D. Schneider, and R. Berndt, *Angew. Chem., Int. Ed.* **39**, 792 (2000). (b) K. Wong, K.-Y. Kwon, B. V. Rao, A. Liu, and L. Bartels, *J. Am. Chem. Soc.* **126**, 7762 (2004). (c) M. deWild, S. Berner, H. Suzuki, H. Yanagi, D. Schlettwein, S. Ivan, A. Baratoff, H.-J. Guentherodt, and T. A. Jung, *ChemPhysChem* **3**, 881 (2002).

[218] (a) A. Kühnle, T. R. Linderoth, B. Hammer, and F. Besenbacher, *Nature* **415**, 891 (2002). (b) X.-B. Mao, C.-X. Wang, X.-K. Wu, X.-J. Ma, L. Liu, L. Zhang, L. Niu, Y.-Y. Guo, D.-H. Li, Y.-L. Yang, and C. Wang, *Proc. Natl. Acad. Sci. U.S.A.* **108**, 19605 (2011).

[219] S. Lukas, G. Witte, and C. Wöll, *Phys. Rev. Lett.* **88**, 028301 (2002).

[220] (a) Y. Wang, X. Ge, G. Schull, R. Berndt, C. Bornholdt, F. Koehler, and R. Herges, *J. Am. Chem. Soc.* **130**, 4218 (2008). (b) T. Yokoyama, S. Yokoyama, T. Kamikado, Y. Okuno, and S. Mashiko, *Nature* **413**, 619 (2001). (c) T. Yokoyama, T. Kamikado, S. Yokoyama, and S. Mashiko, *J. Chem. Phys.* **121**, 11993 (2004). (d) Y. Wang, X. Ge, C. Manzano, J. Kröger, R. Berndt, W. A. Hofer, H. Tang, and J. Cerda, *J. Am. Chem. Soc.* **131**, 10400 (2009).

[221] (a) M.-C. Blüm, E. Ćavar, M. Pivetta, F. Patthey, and W.-D. Schneider, *Angew. Chem., Int. Ed.* **44**, 5334 (2005). (b) D. Écija, J. I. Urgel, A. C. Papageorgiou, S. Joshi, W. Auwärter, A. P. Seitsonen, S. Klyatskaya, M. Ruben, S. Fischer, S. Vijayaraghavan, J. Reichert, and J. V. Barth, *Proc. Natl. Acad. Sci. U.S.A.* **110**, 6678 (2013).

[222] (a) M. Pivetta, M.-C. Blüm, F. Patthey, and W.-D. Schneider, *Angew. Chem.* **120**, 1092 (2008). (b) T. Bauert, L. Merz, D. Bandera, M. Parschau, J. S. Siegel, and K.-H. Ernst, *J. Am. Chem. Soc.* **131**, 3460 (2009).

[223] We define 1 ML as the coverage of the most dense structure observed, Fig. 7.4b.

[224] (a) G. Kresse and J. Furthmüller, *Comput. Mater. Sci.* **6**, 15 (1996). (b) G. Kresse and D. Joubert, *Phys. Rev. B* **59**, 1758 (1999).

[225] (a) S. Strickland and V. Mahdavi, *Cell* **15**, 393 (1978). (b) H. E. Shubeita, J. F. Sambrook, and A. M. Mccormick, *Proc. Natl. Acad. Sci. U.S.A.* **84**, 5645 (1987).

[226] (a) S. M. Barlow and R. Raval, *Surf. Sci. Rep.* **50**, 201 (2003). (b) K.-H. Ernst, *Top. Curr. Chem.* **265**, 209 (2006).

[227] (a) M. Böhringer, K. Morgenstern, W.-D. Schneider, R. Berndt, F. Mauri, A. D. Vita, and R. Car, *Phys. Rev. Lett.* **83**, 324 (1999). (b) T. G. Gopakumar, F. Matino, B. Schwager, A. Bannwarth, F. Tuczek, J. Kröger, and R. Berndt, *J. Phys. Chem. C* **114**, 18247 (2010).

[228] B. Grünbaum and G. C. Shephard, *Tilings and Patterns*, Freeman: New York (1987).

[229] S.-S. Jester, E. Sigmund, and S. Höger, *J. Am. Chem. Soc.* **133**, 11062 (2011).

[230] (a) K. Tahara, T. Balandina, S. Furukawa, S. De Feyter, and Y. Tobe, *CrystEngComm* **13**, 5551 (2011). (b) C. L. Ren, F. Zhou, B. Qin, R. J. Ye, S. Shen, H. B. Su, and H. Q. Zeng, *Angew. Chem., Int. Ed.* **50**, 10612 (2011). (c) O. Guillermet, E. Niemi, S. Nagarajan, X. Bouju, D. Martrou, A. Gourdon, and S. Gauthier, *Angew. Chem.* **121**, 2004 (2009). (d) L. Zoppi, T. Bauert, J. S. Siegel, K. K. Baldridge, and K.-H. Ernst, *Phys. Chem. Chem. Phys.* **14**, 13365 (2012).

[231] R. Robles, S. N. Khanna, and J. Castleman, *Phys. Rev. B* **77**, 235441 (2008).

[232] S. Karan, N. Li, Y. Zhang, Y. He, I.-P. Hong, H. Song, J.-T. Lü, Y. Wang, L. Peng, K. Wu, G. S. Michelitsch, R. J. Maurer, K. Diller, K. Reuter, A. Weismann, and R. Berndt, *In preparation.*

[233] A. R. Rocha, V. M. García-Suárez, S. W. Balley, C. J. Lambert, J. Ferrer, and S. Sanvito, *Nature Mater.* **4**, 335 (2005).

[234] L. Bogani and W. Wernsdorfer, *Nature Mater.* **7**, 179 (2008).

[235] J. Liu, H. Isshiki, K. Katoh, T. Morita, B. K. Breedlove, M. Yamashita, and T. Komeda, *J. Am. Chem. Soc.* **135**, 651 (2013).

[236] R. Requist, S. Modesti, P. P. Baruselli, A. Smogunov, M. Fabrizio, and E. Tosatti, *Proc. Natl. Acad. Sci. U.S.A.* **111**, 69 (2013).

[237] S. Müllegger, M. Rashidi, M. Fattinger, and R. Koch, *J. Phys. Chem. C.* **117**, 5718 (2013).

[238] S. Strickland and V. Mahdavi, *Cell* **15**, 393 (1978).

[239] P. Koskinen and V. Mäkinen, *Comp. Mater. Sci.* **47**, 237 (2009).

[240] V. Blum, R. Gehrke, F. Hanke, P. Havu, V. Havu, X. Ren, K. Reuter, and M. Scheffler, *Comput. Phys. Commun.* **180**, 2175 (2009).

[241] S. R. Bahn and K. W. Jacobsen, *Comput. Sci. Eng.* **4**, 56 (2002).

[242] V. G. Ruiz, W. Liu, E. Zojer, M. Scheffler, and A. Tkatchenko, *Phys. Rev. Lett.* **108**, 146103 (2012).

[243] R. J. Maurer and K. Reuter, *J. Chem. Phys.* **139**, 014708 (2013).

[244] S. J. Clark, M. D. Segall, C. J. Pickard, P. J. Hasnip, M. I. J. Probert, K. Refson, and M. C. Payne, *Z. Kristallogr.* **220**, 567 (2005).

[245] M. Pivetta, M. Ternes, F. Patthey, and W.-D. Schneider, *Phys. Rev. Lett.* 99, 126104 (2007).

[246] W. A. Hofer, G. Teobaldi, and N. Lorente, *Nanotechnology* **19**, 305701 (2008).

[247] T. Choi, S. Bedwani, A. Rochefort, C.-Y. Chen, A. J. Epstein, and J. A. Gupta, *Nano. Lett.* **10**, 4175 (2010).

[248] Y. S. Tan, Y. Yue, and R. D. Webster, *J. Phys. Chem. B* **117**, 9371 (2013).

[249] K. Li , M. Wang, T. Wang, D. Sun, R. Zhu, X. Sun, X. Wu, and S.-L. Wang, *Photochemistry and Photobiology.* **89**, 1064 (2013).

[250] J. Repp, G. Meyer, F. E. Olsson, and M. Persson, *Science* **305**, 493 (2004).

[251] W. Steurer, J. Repp, L. Gross, I. Scivetti, M. Persson, and G. Meyer, *Phys. Rev. Lett.* **114**, 036108 (2015).

[252] M. Sterrer, T. Risse, U. M. Pozzoni, L. Giordano, M. Heyde, H.-P. Rust, G. Pacchioni, and H.-J. Freund, *Phys. Rev. Lett.* **98**, 096107 (2007).

[253] T. A. Costi, *Phys. Rev. Lett.* **85**, 1504 (2000).

[254] W. Liu, A. Tkatchenko, and M. Scheffler, *Acc. Chem. Res.* **47**, 3369 (2014).

[255] M. Stöhr, R. J. Maurer, and K. Reuter, *in preparation*, 2014, Department Chemie, Technische Universität München.

[256] A. Tkatchenko and M. Scheffler, *Phys. Rev. Lett.* **102**, 073005 (2009).

[257] R. J. Maurer and K. Reuter, *Angew. Chem. Int. Ed.* **51**, 12009 (2012).

[258] S. Karan and R. Berndt, *Ready for submission.*

[259] T. Sugawara and M. M. Matsushita, *J. Mater. Chem.* **19**, 1738 (2009).

[260] S. Pramanik, C.-G. Stefanita, S. Patibandla, S. Bandyopadhyay, K. Garre, N. Harth, and M. Cahay, *Nature* **2**, 216 (2007).

[261] M. Garnica, D. Stradi, S. Barja, F. Calleja, C. Diaz, M. Alcami, N. Martin, A. L. Vázquez de Parga, F. Martin, and R. Miranda, *Nature Phys.* **9**, 368 (2013).

[262] P. L. Yeagle, *Biochimica et Biophysica Acta* **882**, 267 (1985).

[263] D. Needham and R. S. Nunn, *Biophys. J.* **58**, 997 (1990).

[264] M. Doxastakis, A. K. Sum, and J. J. de Pablo, *J. Phys. Chem. B* **109**, 24173 (2005).

[265] B. M. Craven, *Nature* **260**, 727 (1976).

[266] H. S. Shieh, L. G. Hoard, and C. E. Nordman, *Nature* **267**, 287 (1977).

[267] M. Hibino and H. Tsuchiya, *Langmuir* **30**, 6852 (2014).

[268] S. Sek, S. Xu, M. Chen, G. Szymanski, and J. Lipkowski, *J. Am. Chem. Soc.* **130**, 5736 (2008).

[269] W. L. Duax, J. F. Griffin, D. C. Rohrer, and C. M. Weeks, *Lipids* **15**, 783 (1980).

[270] N. Hauptmann, K. Scheil, T. G. Gopakumar, F. L. Otte, Ch. Schütt, R. Herges, and R. Berndt, *J. Am. Chem. Soc.* **135**, 8814 (2013).

[271] P. Maksymovych, D. B. Dougherty, X.-Y. Zhu, and J. T. Yates, Jr., *Phys. Rev. Lett.* **99**, 016101 (2007).

[272] L. Xu, N. A. Porter, *Free Radical Research*, In Press. DOI: 10.3109/10715762.2014.985219